

# Rolled-up microtubes as components for Lab-on-a-Chip devices

von der Fakultät für Elektrotechnik und Informationstechnik

der Technischen Universität Chemnitz

genehmigte

Dissertation

zur Erlangung des akademischen Grades

Doktor der Ingenieurwissenschaften

(Dr.-Ing.)

vorgelegt

von: Dipl. Phys. Stefan M. Harazim

geboren am: 24. Juli 1981 in Dresden

eingereicht am: 22. Mai 2012

Gutachter: Prof. Dr. Prof. h.c. Oliver G. Schmidt

Prof. Dr. Dr. Prof. h.c. mult. Thomas Geßner

Tag der Verleihung: 13. November 2012



## ***Bibliographische Beschreibung***

**Stefan M. Harazim**

Rolled-up microtubes as components for Lab-on-a-Chip devices

Dissertation (in englischer Sprache)

118 Seiten, 52 Abbildungen, 2 Tabellen, 130 Literaturverweise

## ***Referat***

Die auf verspannten Dünnschichten basierende „rolled-up nanotechnologie“ ist eine leistungsfähige Methode um dreidimensionale hohle Strukturen (Mikroröhrchen) aus nahezu jeder Art von Material auf einer großen Vielfalt von Substraten herzustellen.

Ausgehend von der Möglichkeit der Skalierung des Röhrchendurchmessers und der Modifikation der Funktionalität des Röhrchens durch Einsatz verschiedener Materialien und Oberflächenfunktionalisierungen kann eine große Anzahl an verschiedenen Anwendungen ermöglicht werden. Eine Anwendung behandelt unter anderem on-chip Studien einzelner Zellen wobei die Mikroröhrchen, an die Größe der Zelle angepasste, Reaktionscontainer darstellen. Eine weitere Modifikation der Funktionalität der Mikroröhrchen kann durch das Aufbringen einer katalytischen Schicht realisiert werden, wodurch das Mikroröhrchen zu einem selbstangetriebenen katalytischen Mikro-Motor wird.

Hauptziel dieser Arbeit ist es Mikrometer große optisch aktive Glasröhrchen herzustellen, diese mikrofluidisch zu kontaktieren und als Sensoren in Lab-on-a-Chip Systeme zu integrieren. Die integrierten Glasröhrchen arbeiten als optofluidische Ringresonatoren, welche die Veränderungen des Brechungsindex von Fluiden im inneren des Röhrchens durch Änderungen im Evaneszenzfeld detektieren können. Die Funktionsfähigkeit eines Demonstrators wird mit verschiedenen Flüssigkeiten gezeigt, dabei kommt ein Fotolumineszenz Spektrometer zum Anregen des Evaneszenzfeldes und Auslesen des Signals zum Einsatz. Die entwickelte Integrationsmethode ist eine Basis für ein kostengünstiges, zuverlässiges und reproduzierbares Herstellungsverfahren von optofluidischen Mikrochips basierend auf optisch aktiven Mikroröhrchen.

---

**Keywords:** rolled-up nanotechnology, strain-engineering, microtube, on-chip integration, lab-on-a-chip, microfluidic, optofluidic, optical ring resonator, photoluminescence spectroscopy, refractometric sensing



## ***Abstract***

Rolled-up nanotechnology based on strain-engineering is a powerful tool to manufacture three-dimensional hollow structures made of virtually any kind of material on a large variety of substrates. The aim of this thesis is to address the key features of different on- and off-chip applications of rolled-up microtubes through modification of their basic framework.

The modification of the framework pertains to the tubular structure, in particular the diameter of the microtube, and the material which it is made of, hence achieving different functionalities of the final rolled-up structure. The tuning of the microtube diameter which is adjusted to the individual size of an object allows on-chip studies of single cells in artificial narrow cavities, for example. Another modification of the framework is the addition of a catalytic layer which turns the microtube into a self-propelled catalytic micro-engine. Furthermore, the tuneability of the diameter can have applications ranging from nanotools for drilling into cells, to cargo transporters in microfluidic channels. Especially rolled-up microtubes based on low-cost and easy to deposit materials, such as silicon oxides, can enable the exploration of novel systems for several scientific topics.

The main objective of this thesis is to combine microfluidic features of rolled-up structures with optical sensor capabilities of silicon oxide microtubes acting as optical ring resonators, and to integrate these into a Lab-on-a-Chip system. Therefore, a new concept of microfluidic integration is developed in order to establish an inexpensive, reliable and reproducible fabrication process which also sustains the optical capabilities of the microtubes. These integrated microtubes act as optofluidic refractometric sensors which detect changes in the refractive index of analytes using photoluminescence spectroscopy. The thesis concludes with a demonstration of a functional portable sensor device with several integrated optofluidic sensors.



## ***Table of contents***

1	General introduction.....	1
1.1	Motivation .....	1
1.2	Aim and structure of this thesis .....	2
2	Background .....	5
2.1	Rolled-up nanotech - deterministic fabrication of self-assembled microchannels .....	5
2.2	Liquids at the microscale.....	8
2.3	Optofluidic Lab-on-a-Chip devices – label-free detection .....	8
3	Methods and materials.....	17
3.1	Deposition methods .....	17
3.1.1	Lithography .....	17
3.1.2	Electron beam evaporation .....	18
3.1.3	Atomic layer deposition .....	19
3.2	Characterization methods .....	20
3.2.1	Scanning electron microscopy.....	20
3.2.2	Photoluminescence spectroscopy .....	21
3.2.3	Optofluidic setup and analytes .....	21
3.3	Fabrication methods .....	23
3.3.1	Fabrication of SiO <sub>x</sub> microtubes .....	23
3.3.2	On-Chip integration of SiO <sub>2</sub> microtubes .....	24
4	Scaling of SiO <sub>x</sub> microtubes and potential applications.....	29
4.1	Introduction .....	29
4.2	Microtube fabrication .....	30
4.3	Characterization of rolled-up microtubes .....	33
4.4	Field of application of SiO <sub>x</sub> microtubes – a perspective .....	37
4.4.1	Microtubes as artificial cavities for cells.....	37
4.4.2	Catalytic microtubes as versatile tools .....	39
4.4.3	On-chip components: pumps, valves and sensors .....	42
4.5	Conclusion.....	45
5	SiO <sub>2</sub> microtubes as optofluidic sensors integrated on-chip .....	47
5.1	Introduction .....	47
5.2	Microchip fabrication .....	48
5.3	Controlling liquids within the microchip.....	64
5.4	Sensor Characterization.....	67
5.4.1	Quality factor (Q) evolution .....	67
5.4.2	Response of the PL spectrum - from air to water .....	68
5.4.3	Response of the PL spectrum - while drying out.....	71
5.4.4	Stop-flow signal stability.....	72

---

5.4.5 In-flow signal stability .....	72
5.4.6.....Sensing fluids with different refractive index .....	74
5.5 Conclusions.....	77
6 Conclusion and Outlook.....	79
Bibliography.....	81
List of Figures and Tables .....	93
Theses.....	97
Curriculum Vitae .....	103

# ***Titel***

Aufgerollte Mikroröhrchen als Komponenten in Lab-on-a-Chip Systemen

## ***Inhaltsverzeichnis***

1	Allgemeine Einleitung .....	1
1.1	Motivation .....	1
1.2	Ziel und Struktur der Arbeit.....	2
2	Hintergrund .....	5
2.1	Rolled-up nanotech – deterministische Herstellung von selbstformierenden Mikrokanälen.....	5
2.2	Verhalten von Flüssigkeiten im Mikrometerbereich .....	8
2.3	optofluidische Lab-on-a-Chip Systeme – markerfreie Detektion.....	8
3	Methoden und Materialien .....	17
3.1	Abscheidemethoden .....	17
3.1.1	Lithographie .....	17
3.1.2	Elektronstrahlverdampfung .....	18
3.1.3	Atomlagenabscheidung .....	19
3.2	Charakterisierungsmethoden .....	20
3.2.1	Rasterelektronenmikroskopie .....	20
3.2.2	Photolumineszenzspektroskopie.....	21
3.2.3	optofluidisches Setup und verwendete Flüssigkeiten .....	21
3.3	Herstellungsmethoden .....	23
3.3.1	Herstellung von SiO <sub>x</sub> Mikroröhrchen.....	23
3.3.2	On-Chip Integration von SiO <sub>2</sub> Mikroröhrchen.....	24
4	Skalierung von SiO <sub>x</sub> Mikroröhrchen und deren mögliche Anwendungen .....	29
4.1	Einleitung .....	29
4.2	Herstellungsprozess der Mikroröhrchen.....	30
4.3	Charakterisierung der aufgerollten Mikroröhrchen .....	33
4.4	Potentielle Anwendungen der SiO <sub>x</sub> Mikroröhrchen – eine Perspective .....	37
4.4.1	Mikroröhrchen als künstliche Container für Zellen.....	37
4.4.2	Katalytische Mikroröhrchen als verschiedene Werkzeuge.....	39
4.4.3	On-chip Komponenten: Pumpen, Ventile und Sensoren.....	42
4.5	Schlussfolgerung .....	45
5	SiO <sub>2</sub> Mikroröhrchen als optofluidische Sensoren integriert in eine Chipstruktur .....	47
5.1	Einleitung .....	47
5.2	Mikrochip Herstellung.....	48
5.3	Steuerung der Flüssigkeiten im Mikrochip .....	64
5.4	Sensor Charakterisierung.....	67

---

5.4.1	Entwicklung des Qualitätsfaktors (Q).....	67
5.4.2	Reaktion des PL Spektrums – Übergang von Luft zu Wasser .....	68
5.4.3	Reaktion des PL Spektrums – während des Austrocknens .....	71
5.4.4	Signalstabilität bei einer stehenden Flüssigkeit .....	72
5.4.5	Signalstabilität bei einer fließenden Flüssigkeit .....	72
5.4.6	Detektion von Flüssigkeiten mit verschiedenen Brechungsindizes .....	74
5.5	Schlussfolgerung.....	77
6	Schlussfolgerung und Ausblick .....	79
	Literaturverzeichnis.....	81
	Abbildungs- und Tabellenverzeichnis .....	93
	Thesen .....	97
	Lebenslauf .....	103

## *Acronyms and Abbreviations*

2D	Two-Dimensional
3D	Three-Dimensional
ALD	Atomic Layer Deposition
AFM	Atomic Force Microscope
BSE	Back Scattered Electrons
CCD	Charge Coupled Device
CPD	Critical Point Dryer
CVD	Chemical Vapor Deposition
CW	Continues Wave (Laser)
DCA	DCA Instruments
DI	De-Ionized Water
DL	Detection Limit
DLC	Diamond Like Carbon
DMSO	Dimethylsulfoxid
DNA	Deoxyribonucleic Acid
ECM	Extra Cellular Matrix
EDL	Electrical Double Layer
EO	Electroosmotic
FFT	Fast Fourier Transformation
FIB	Focused Ion Beam
LoC	Lab-on-a-Chip
$\mu$ -TAS	Mirco Total Analysis System
MA 56	Mask Aligner, Version 5.6
MBE	Molecular Beam Epitaxy
MEMS	Microelectromechanical System
MIF	Metal Ion Free
OFRR	Optofluidic Ring Resonator
PBS	Phosphate Buffered Saline
PDMS	Polydimethylsiloxane
PEB	Post Exposure Baking
PL	Photoluminescence
PTFE	Polytetrafluoroethylene
PVD	Physical Vapor Deposition

QCM	Quartz Crystal Microbalance
Q	Quality factor (optical)
RI	Refractive Index
RIU	Refractive Index Unit
RR	Ring Resonator
SAM	Self-Assembled Monolayer
SDS	Sodium Dodecyl Sulfate
SE	Secondary Electrons
SEM	Scanning Electron Microscope
SPR	Surface Plasmon Resonance
TMA	Trimethylaluminium, ALD precursor
UV	Ultraviolet
WGM	Whispering Gallery Mode

## *Symbols and Chemical Formulas*

<b>Symbol</b>	<b>Description</b>
A	wrinkling amplitude
$a_1, a_2$	lattice constants for material 1 and 2
$\text{Al}_2\text{O}_3$	aluminum oxide
$\alpha$	glancing angle for e-beam evaporation
Au	gold
$\beta_1, \beta_2$	inherent strain of material 1 and 2
$\Delta\beta$	strain gradient
C	carbon
$\text{CO}_2$	carbon dioxide
Cr	chrome
d	depth of a channel
$d_1, d_2$	thicknesses of nanomembrane 1 and 2
$\varepsilon$	in plane biaxial strain
$\eta$	viscosity of a fluid
$F_e$	tooling factor, e-beam
g	gravitational acceleration
h	etching distance
$h_{\text{cap}}$	length of a capillary
$\text{H}_2\text{O}$	water
$\text{H}_2\text{O}_2$	hydrogen peroxide
$I_{\text{tube}}$	flow velocity of a fluid
j	Young module ratio
$\lambda$	wrinkling wavelength
$\lambda_D$	Debye length
$\lambda_m$	resonant wavelength
L	length of a channel
$L_{\text{eff}}$	effective length of the optical light path
m	resonant mode number
$\nu$	Poisson ratio
$n_1, n_2, \dots$	refractive index for material 1, material 2, ...
$n_{\text{eff}}$	effective refractive index
$\Delta n$	change of refractive index

$n_{\text{PBS}}, n_{\text{DI}}$	refractive index for PBS and DI water
$\text{N}_2$	gaseous nitrogen
$\text{O}_2$	gaseous oxygen
$\text{OH}$	hydroxide
$\Delta p$	pressure gradient (in a tube)
$p_{\text{cap}}$	capillary pressure
$\text{Pt}$	platinum
$R$	radius of a tubular structure
$R_{\text{sens}}$	sensor resolution
$R_{\text{spec}}$	spectral resolution
$\rho$	density
$r$	length of a microtube
$\text{Re}$	Reynolds number
$R_{\text{tube}}$	flow resistance
$v_{\text{inlet}}, v_{\text{outlet}}$	velocity of a fluid at the in- or outlet
$\Delta v$	relative fluid velocity
$v_{\text{sp}}$	Spin speed
$\sigma$	surface tension
$\sigma_d$	standard deviation
$\text{Si}$	silicon
$\text{SiO}$	silicon monoxide
$\text{SiO}_2$	silicon dioxide
$\text{SiO}_x$	silicon oxide compound
$\text{Si-CH}_3$	methyl group
$\text{Si-OH}$	Silanol
$T_D$	film thickness measured by a Dektak profiler
$\theta$	contact angle
$T_M$	film thickness measured by a QCM based thickness monitor
$v$	velocity of a fluid
$Y_1, Y_2$	Young module for material 1 and 2
$\zeta(x,y)$	deflection profile of a wrinkled membrane
$\zeta$	zeta potential

# ***1 General introduction***

## ***1.1 Motivation***

The area of biochemical analysis in medical applications is probably one of the fastest growing markets. In the next decades the average age of western people is expected to increase significantly. This demographic development may raise new difficulties in hospitals and laboratories due entirely to the large number of patients. Hence, to relieve these facilities and to speed up the diagnosis process, it will become increasingly important to transfer the process of diagnosis to the location of the patient. This hospital and laboratory free analysis is called point-of-care diagnosis and contains clear benefits: it can significantly reduce the diagnosis time since the analysis will be performed at the location of the patient which avoids the transport of samples to the laboratories. Furthermore, point-of-care diagnostic devices are portable and operational at locations where no hospitals or laboratories are available for analysis.

A point-of-care device has to fulfill certain requirements such as portability, low production and sales costs, reliability and construction for mass fabrication. The scientific community has named this device a micro total analysis system ( $\mu$ -TAS). Such systems combine all analytical processes performed in a laboratory including sample pre-preparation, analyte separation and purification, analyte detection and data analysis, on a small and portable unit. Devices which are able to realize parts of the functions of a  $\mu$ -TAS are called Lab-on-a-Chip (LoC) devices. LoC devices usually involve sensors and actuators at the micrometer scale whereas the readout and processing of the collected information is mainly performed by external devices. Components such as micro pumps, micro valves and micro mixers act as actuators to manipulate and move the analyte on the chip. Sensors in LoC devices are most commonly based on optical, electrical, magnetically or chemical sensing mechanisms.

Nowadays, the manipulation of fluids, addressed by the field of microfluidics, already reached a state of development where complex fluid handling is possible. However, the detection of analytes and their contents using scaled down and integrated sensors is still a challenging issue for the scientific community. The sensing mechanisms for optical detection of analytes cover a broad field of labeled and label-free working sensors. Especially the label-free sensors are of great interest for the point-of-care concept since this detection mechanism avoids additional steps for sample preparation and additional reagents, which consequently leads to a faster and direct analysis of the sample. There are a variety of methods available to fabricate optical label-free sensors. Among these, a particular method based on rolled-up nanotech has been recently developed in the IIN institute. With this method it is possible to fabricate tubular structures with

sizes that enable the integration into Lab-on-a-Chip devices and with intrinsic properties that can be utilized for label-free optical detection. The next section gives an insight into the aim of this work utilizing the rolled-up nanotech in combination with the LoC approach and a short overview on the structure of this thesis.

## ***1.2 Aim and structure of this thesis***

The rolled-up nanotech enables the fabrication of tubular structures with sensing capabilities on virtually any kind of substrate. Two objectives of this thesis are to investigate a reliable fabrication process of tubular structures yielding large quantities of tubes, and the ability to tune the dimension of the microtubes in length and diameter. Aside from the given overview on a large variety of applications for such microtubes, the main focus of this work relies on the microfluidic on-chip integration of optical active microtubes as refractometric sensors. This challenging engineering task involves the development of a novel chip structure design with well-established fabrication steps and parameters in order to maintain the optical capabilities of the microtubes during the integration process. While keeping the goal of a reliable and a low-cost fabrication process in mind, all materials utilized in this work are selected carefully and the chip design is carried out to be suitable for the fabrication of larger quantities of devices at the wafer level.

In chapter two (*Background*) a brief introduction to the rolled-up nanotech is presented, followed by an overview of the characteristics of fluids at the microscale. Because the utilized microtubes in this work combine inherent fluidic functionality and optical capabilities, the background chapter closes with an introduction to optofluidic sensors at the microscale with emphasis on optical ring resonators.

Chapter three (*Methods and protocols*) describes in the first subsection the material deposition methods utilized to fabricate and modify the tubular structure. The second subsection discusses two main characterization methods employed in this thesis, which are in particular scanning electron microscopy (SEM) and photoluminescence (PL) spectroscopy. The third subsection contains protocols enabling the reader to repeat all established processes from this thesis.

Chapter four (*Scaling of SiO<sub>x</sub> microtubes and potential applications*) discusses the method of fabricating large numbers of well aligned microtubes with different diameters made of SiO<sub>x</sub> material. An implemented macroscopic continuum mechanical model shows good agreement with the collected data of the modified microtubes. This chapter finishes with a selection of possible off- and on-chip applications of SiO<sub>x</sub> microtubes.

Chapter five (*SiO<sub>2</sub> microtubes as optofluidic sensors integrated on-chip*) starts with an introduction and a detailed description of the integration process of SiO<sub>2</sub> microtubes into an on-

chip microfluidic structure. The following subsections discuss the methods of controlling fluids on the chip and its limitations followed by the characterization of the integrated microtubes according to their sensing capabilities. The last subsection presents the results and gives a conclusion on the integration process with an outlook toward further applications.

Chapter six (*Conclusion and Outlook*) summarizes the thesis and discusses possible applications of integrated microtubes as well as other applications of the newly developed integration method for microtubes containing different functionalities.

Chapter seven (*Theses*) summarizes and recapitulates the main aspects of this work in several theses.



## 2 Background

### 2.1 Rolled-up nanotech - deterministic fabrication of self-assembled microchannels

Rolled-up nanotech is a technological concept introduced about a decade ago by Schmidt and Eberl in the Journal *Nature* [1] and is based on scrolled heterostructures.<sup>[2]</sup> The concept enables the fabrication of tubular structures formed by thin films consisting of virtually any kind of material on many different substrates. The underlying principle involves the release of a thin solid film with an internal strain gradient from a substrate by a selective etching procedure. An example is given in Figure 2.1.

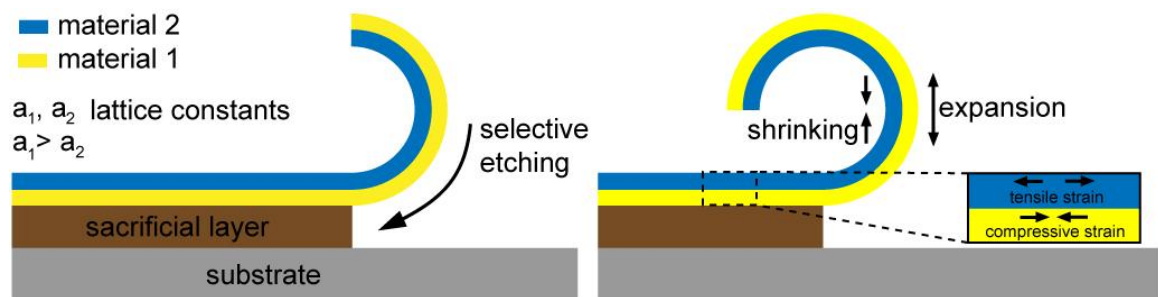


**Figure 2.1:** General method to create a nanotube. The layer sequence consists of an etchant-sensitive material, followed by a bilayer of two different materials (materials 1 and 2) with corresponding lattice constants  $a_1$  and  $a_2$  ( $a_1 > a_2$ ). Once the bilayer is released by selective etching, the bilayer bends upwards and forms a nanotube. (Adapted from Ref. [1])

A bilayer consisting of two crystalline materials with different lattice constants  $a_1$  and  $a_2$  ( $a_1 > a_2$ ) is released from the substrate by selectively etching of the etchant sensitive material, the so-called sacrificial layer. All layers are grown in single-crystal quality by molecular beam epitaxy (MBE) to achieve an internal strain gradient in the bilayer. The heteroepitaxial growth lead to a pseudomorphical rearrangement of the lattices of the two top materials influenced by the lattice of the sacrificial layer with the consequence that the first grown material layer (yellow) contains compressive strain and the second layer (blue) has inherent tensile strain. Selective etching of the sacrificial layer releases the bilayer and leads to lattice rearrangements. The compressed lower layer extends whereas the lattice of the top layer shrinks. By controlling the etching depth and the specific lattice parameters of the deposited materials the bilayer can roll-up into a tubular structure. The number of revolutions as well as the position of the tube on the substrate is determined by the starting point of the etching process and the etching distance.

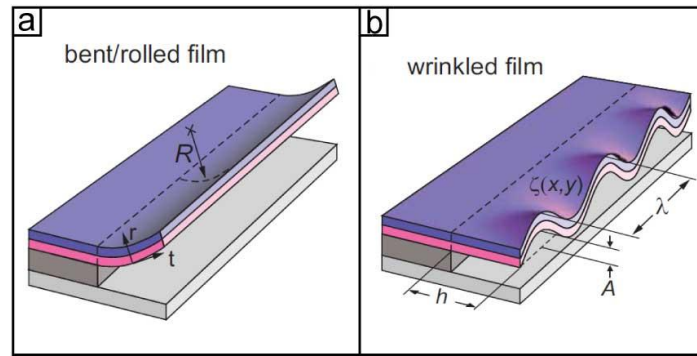


**Figure 2.2:** Schematics of bending behavior. (a) Bent film with inner radius  $R$ , and (b) wrinkled structure with deflection profile  $\zeta(x,y)$ , amplitude  $A$ , and wavelength  $\lambda$  (Taken from Ref. [3]).

A more general and analytical description of the bending behavior of strained bilayers is given by Cendula et al. [3]. The bilayer, also called nanomembrane, containing two different build-in biaxial strains  $\beta_1$  (bottom layer) and  $\beta_2$  (top layer), can either wrinkle or bend after release, depending on the strain gradient  $\Delta\beta = \beta_2 - \beta_1$  in the nanomembrane. If the gradient is small ( $\Delta\beta < 0.5\%$ ) the nanomembrane prefers to wrinkle, but it will roll-up if the gradient is larger than 0.5%. Figure 2.2 illustrates the two different bending behaviors: (a) bending or respectively rolling-up with a certain radius  $R$  and (b) wrinkling with a wrinkle wavelength  $\lambda$  and amplitude  $A$ . The etching distance is given by  $h$ .

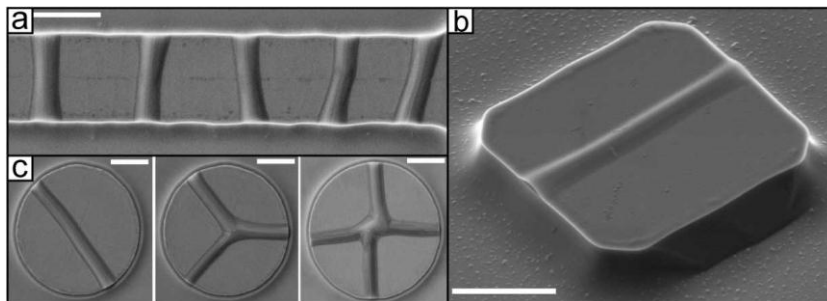


**Figure 2.3:** SEM images of wrinkled nanomembranes. The dependence of the wrinkling behavior of nanomembranes on the shape of the strained layer. (a) Stripes form mainly parallel wrinkles. (b) Circular shaped membranes form different channel structures such as straight, three-way or even four way channels (left to right). (c) Tilted view on a square shaped wrinkle structure preferably forming a straight channel. Scale bars are  $2\ \mu\text{m}$  (Taken from [4])

The pattern of the wrinkles depends also on the shape of the nanomembrane. Some examples are illustrated in Figure 2.3. Stripe like (a), square like (b) and circular like shapes (c) result in a variety of different wrinkling types with heights of about 100 nm and widths of less than 400 nm which could act as nanochannels for fluidic applications. In this particular case the wrinkled nanomembrane consists of a 20 nm thick InGaAs/GaAs bilayer grown by MBE on an 80 nm thick

AlAs sacrificial layer. The patterning and release of the nanomembrane is performed by photolithography and wet chemical etching.<sup>[4]</sup>

The fluidic capabilities and the fluidic integration in on-chip devices of such wrinkled channels is proven<sup>[4-6]</sup> and wrinkles can be created at almost any scale.<sup>[7,8]</sup> However, one limitation of these wrinkled nanomembranes is that wrinkled membranes so far cannot be detached from the substrate deterministically. Furthermore, the required complex and expensive MBE layer growth to fabricate the nanomembranes makes the wrinkles unattractive for Lab-on-a-Chip applications. In general, the wrinkling and rolling of nanomembranes grown by MBE has foreseen the potential of deterministically fabricated hollow cavities acting as fluidic channels. It was just the beginning of a rewarding journey of exploring the possibilities of rolled-up nanotech.

An improved roll-up technique, invented just a few years ago, solved the problem of expensive fabrication: the strain engineering of nanomembranes on polymers from Mei et al. [9]. This technique replaces the epitaxial growth of the sacrificial layer and the pre-stressed nanomembrane by deposition methods which are easier to handle and less expensive. The deposition of the nanomembrane is performed by electron beam (e-beam) evaporation at different deposition rates, where a higher rate will lead to a higher build-in strain. Alternatively, the deposition at constant rates but at different temperatures can also lead to a strain gradient within the nanomembrane. However, the most important modification of the roll-up technique is the use of a modified sacrificial layer. This sacrificial layer is a photo active polymer called photoresist which can be easily created on a substrate by spin coating.

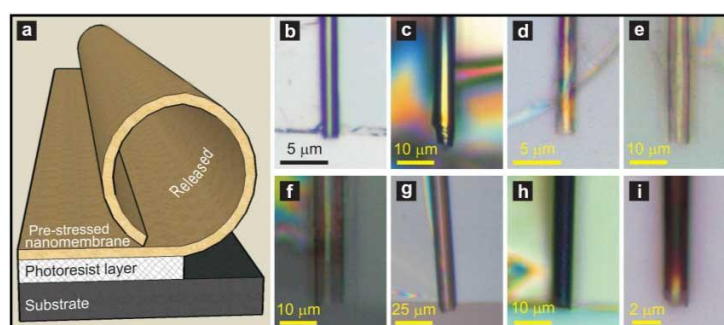


**Figure 2.4:** Rolled-up nanotech on polymers. (a) Schematic diagram illustrating the roll-up process of a nanomembrane into a tube on photoresist; optical images of rolled-up nanomembranes made out of (b) Pt, (c) Pd/Fe/Pd, (d) TiO<sub>2</sub>, (e) ZnO, (f) Al<sub>2</sub>O<sub>3</sub>, (g) Si<sub>3</sub>N<sub>4</sub>, (h) Si<sub>3</sub>N<sub>4</sub>/Ag, and (i) diamond like carbon (DLC) (Taken from Ref. [9]).

The schematic in Figure 2.4.a illustrates the rolling-up principle. After structuring the photoresist by photolithography, a substrate can contain an enormous number of rolled-up microtubes.<sup>[10]</sup> In order to pin the rolled-up microtubes to the substrate the material is deposited at a certain angle on the polymer pattern. This creates an anchor at the close end of the pattern (compared to the

material source of the e-beam) and fixes the nanomembrane to the substrate. Due to ballistic shadow effects at the far end of the polymer pattern, this part of the pattern is not covered by the nanomembrane and a selectively working etchant can reach the sacrificial layer through this window. The optical images in Figure 2.4.b-i show microtubes rolled-up on photoresist consisting of different materials after etching the sacrificial layer.

SiO<sub>x</sub> is of particular interest in this thesis for rolling-up microtubes because it has been shown that this material can roll-up utilizing the rolled-up nanotech on polymers.<sup>[11]</sup> Furthermore, SiO<sub>x</sub> shows biocompatibility, is transparent in the visible spectrum, compatible with semiconductor transistor technology and is also optically active.<sup>[10,12,13]</sup> In conclusion, this material is very attractive to be utilized as a LoC component because a microtube made of SiO<sub>x</sub> combines inherently fluidic functionality, biocompatibility and optical properties. The behavior of fluids in channels at the microscale with dimensions in the lower micrometer regime, comparable to the diameter of rolled-up SiO<sub>x</sub> microtubes, is discussed in the next section.

## 2.2 *Liquids at the microscale*

Liquids at the microscale behave differently compared to the macroscopic world. Some of the well-known characteristics of liquids at the microscale are laminar flow and capillary forces which have influences on the way how the manipulation of liquids at this dimension is affected. Laminar flow means no turbulences in the flowing liquid and hence, the mixing of two different liquids is mainly driven by diffusion. The type of flow in a system (laminar or turbulent) can be determined by the Reynolds number. The Reynolds number  $Re$  depends on the characteristics of the utilized liquid and the dimension of the channel. This dimensionless value and can be calculated by,<sup>[14]</sup>

$$Re = \frac{\rho dv}{\eta} \quad (2.1)$$

where  $\rho$  is the density of the liquid,  $d$  is the length of the channel,  $v$  corresponds to the velocity of the moving liquid and  $\eta$  is its viscosity. Values above 2300 indicate turbulent flow; below 2300 the flow is laminar.<sup>[14]</sup> If the liquid is driven by external pressure through a tube, the stream lines (velocity vectors) of the liquid form a parabolic shape, where the highest velocity is present in the center of the cross-section area of the channel.

Capillary forces, which are another important characteristic in channels at the microfluidic scale, can contribute to the filling of microchannels. In general, the cohesion forces, the gravity and the adhesion forces at the triple point (where wall, liquid and gas are in contact) accumulate in a force, whose force-vector can point towards the solid wall or the liquid. In the case when a capillary with an appropriate small dimension is immersed into a liquid and depending on the

material characteristics of the wall and the liquid, the resulting force can elevate the level of the liquid inside the capillary above the liquid level around the capillary or below. The angle between the tangent on the surface of the liquid and the solid surface is called the contact angle  $\theta$ . If this angle is smaller than  $90^\circ$ , a liquid enters the capillary to a certain height  $h$  above zero level. This height can be calculated by,<sup>[14]</sup>

$$h_{cap} = \frac{2\sigma \cos \theta}{\rho g R} \quad (2.2)$$

where  $\sigma$  is the surface tension of the liquid at the liquid-air interface,  $\rho$  the density of the liquid,  $g$  the gravitational acceleration and  $R$  the radius of the capillary. For example: a glass capillary with a radius of  $5 \mu\text{m}$  is immersed into water the height reaches  $2.8 \text{ m}$  and the so-called capillary pressure  $p_{cap}$  is  $280 \text{ mbar}$  calculated by,

$$p_{cap} = h_{cap} \cdot \rho g = \frac{2\sigma \cos \theta}{R} \quad (2.3)$$

In common LoC devices the value of the capillary pressure is important if the microchannels should be emptied. In this specific case a negative pressure of at least  $280 \text{ mbar}$  has to be applied to the liquid by some actuator to overcome the capillary forces and to empty the microchannel.

But not only capillary forces and the laminar flow have an influence on the manipulation of liquids at the microscale. The velocity of the flux  $I_{tube}$  of a liquid strongly depends on the shape and the dimension of the microchannel. The flux for a tubular channel structure can be calculated by an adapted Hagen-Poiseuille-law equation,<sup>[14]</sup>

$$I_{tube} = \frac{\pi R^4 \Delta p}{8\eta L} \quad (2.4)$$

where  $L$  is the length of the channel,  $\Delta p$  the pressure gradient within the tube,  $R$  the diameter and  $\eta$  the viscosity of the liquid. The flow resistance defined by  $R_{tube} = \Delta p / I_{tube}$  can be calculated by,

$$R_{tube} = \frac{8\eta L}{\pi R^4} \quad (2.5)$$

The strong dependence on the diameter of the flow resistance makes it very difficult to move liquids in channels with diameters smaller than  $1 \mu\text{m}$  while applying mechanical pressure by external forces. A technical solution to achieve high pressure in such small cavities could be provided by electroosmotic (EO) forces where liquids can be forced to move by an external electrical field.<sup>[15]</sup> As an example for an electroosmotic pump, the achieved pressure to move a liquid in a  $1.1 \mu\text{m}$  cavity is about  $24 \text{ bar}$  at an applied voltage of  $2 \text{ kV}$ .<sup>[15]</sup>

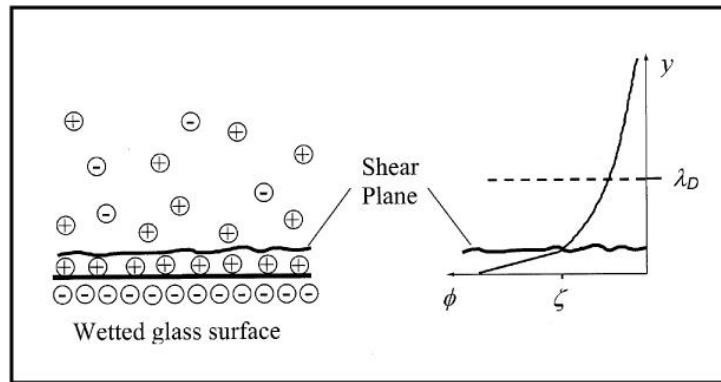


**Figure 2.5:** Schematic of the structure of the electric double layer. Glass acquires a negative surface charge upon contact with an aqueous solution. The surface charge attracts dissolved counter-ions and repels co-ions, resulting in a charge separation. The zeta potential ( $\zeta$ ) is the potential at the shear plane and the Debye length ( $\lambda_D$ ) is the characteristic thickness of the double layer. A layer of immobile positive ions immediately adjacent to the wall is called the Stern layer. [Text and image taken from Ref. [15]]

The required conditions for EO flow are depicted in Figure 2.5. Ions with opposite charges compared to the surface, will concentrate near the wall. This layer in the electrolyte is called electrical double layer (EDL). The layer where only the counter ions are located is called shear plane with a certain potential  $\zeta$ . In this layer, the ions can be forced to be moved by external electrical fields because the electrical neutrality is not given.<sup>[16]</sup> The so-called Debye length defines the overall thickness of the electrical double layer (EDL) which can range from lower than 1 nm up to about 100 nm in thickness depending on the concentration of ions in the liquid.<sup>[16]</sup> However, EO pumps are only suitable if the volume of liquid in the channel is small enough to be dragged off by shear forces of the moving liquid in the EDL.

The advantage of EO pumping in LoC devices is that the electroosmotic pressure occurs only where the electrical field is applied and not everywhere in the microchip structure. This is important since many LoC devices in the scientific community have comparatively low pressure limits of some Bar before damage, because of the use of poly-dimethylsiloxane (PDMS) for fabrication,<sup>[17,18]</sup> as the review from Sollier et al. [19] summarizes. However, PDMS allows a fast, low-cost and reproducible fabrication of microfluidic chips and as long the pressure limits are not exceeded the microchips work reliable.

To conclude, it is important for the fabrication of a Lab-on-a-Chip device to evaluate device specific parameters such as applied flow speed, flow resistance, required pressures and channel dimensions, before the design and fabrication of such a device starts. If the estimated values are taken in account in the chip design, possible system failures such as delamination, disassembly, too high flow resistance and turbulences in the flow during the operation of the device can be reduced.

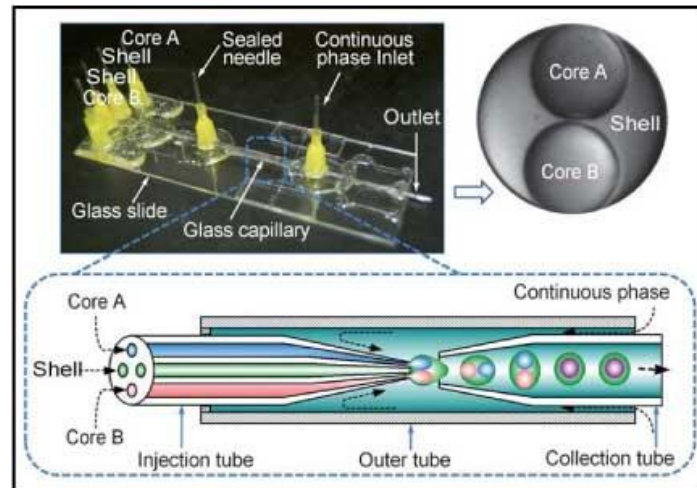


**Figure 2.6:** Example a complex on-chip microfluidic structure. The glass microfluidic device designed to make double emulsions where each droplet contains two inner cores A and B. The schematic within the dashed boundary shows the flow process of the emulsions through the pair of nozzles, and the dashed arrows on the schematic show the flow directions of the different phases. (Taken from [20])

The microfluidic chip depicted in Figure 2.8 fabricated by Chen et al. [20] is a “droplet in droplet” generator and demonstrates state-of-the-art possibilities of engineering and controlling liquids at the microscale. Here, it is crucial to have laminar flow at defined and well controllable velocities in order to generate such a complex droplet emulsion. Furthermore, the dimensions of the channels in the injection tube have to have a suitable diameter which is an agreement between a small as possible diameter to generate micrometer sized droplets and a large enough diameter to allow a high throughput with low as possible flow resistance.

### 2.3 Optofluidic Lab-on-a-Chip devices – label-free detection

Optofluidics at the microscale is a relative young field of research that emerged during the past six to seven years<sup>[21]</sup> combining microfluidics for sample delivery and optics for sensing<sup>[22]</sup> in LoC devices. In general, one can distinguish between labeled and label-free optical detection whereas label-free sensing has the advantage that there is no need for a pre-treatment of the sample prior the detection step. Labeled detection relies mainly on fluorescence microscopy on dye labeled objects or molecules; label-free detection is served by a broad field of optical detection mechanisms such as refractive index (RI) detection, optical absorption and detection by Raman spectroscopy. In this thesis the focus is on RI-based detection, in particular on the kind of RI detection which technically could detect both, the refractive index of a bulk solution and the molecule concentration near the sensor surface. The detection principle of label-free RI based sensor is depicted in Figure 2.7.

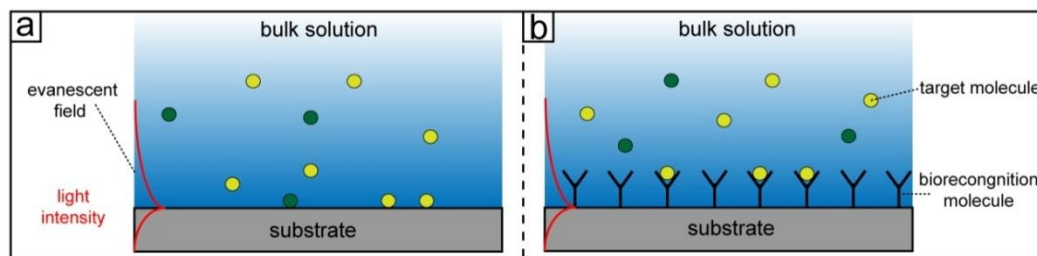


**Figure 2.7:** General schematic of the detection principle of label-free refractive index based sensors. (a) Unspecific physical adsorption and (b) specific bonding of target molecules. Light is guided through the substrate forming an evanescent field which penetrates the bulk solution. (Adapted from Ref. [23]).

In general, for label-free RI sensors light is traveling through the sensor material and forms an evanescent field at the fluid-sensor interface with a certain penetration depth into the bulk solution of a few tens to several of hundreds of nanometers.<sup>[24]</sup> Either there is a bare surface on the substrate or the surface is functionalized with for instance immobilized biorecognition molecules such as antibodies, aptamers or phages.<sup>[23]</sup> Both together, the bulk solution and the sensor surface, have a certain RI. If light is traveling through the sensor substrate according to the boundary conditions given by the system, the formed evanescent field can sense these conditions. The evaluation of the readout signal will give a specific blank value. Once the target molecules are introduced into the bulk solution they can concentrate near the surface of the sensor due to unspecific physical adsorption (Figure 2.7.a) or specific binding with the recognition molecules (Figure 2.7.b). This concentration change will change the RI near the sensor surface which eventually changes the conditions for the evanescent field. Consequently, the sensor can be calibrated by a correlation between the detected change in the light propagation and the introduced target molecules. In case of a sensor for detection of the RI change of an analyte, the mechanism

is comparable but with the difference that the change of the RI is homogeneous in the entire solution.

The sensing mechanism described above is common for a variety of label-free optical sensors. Among them are surface plasmon resonance (SPR) based sensors; interferometer-based sensors; optical waveguide based sensors; photonic crystal based sensors; optical fiber based sensors and optical ring resonator based sensors.<sup>[23]</sup>

The structure of an optical ring resonator (RR) can be made of different shapes and if combined with fluidics they are called optofluidic ring resonator (OFRR). Such shapes can be for instance, microspheres, planar RRs, micro disc RRs and tubular shaped RRs as depicted in Figure 2.8.a.<sup>[12,23,25,26]</sup> The focus in this thesis is on tubular RRs because they inherently combine fluidic functionality and optical capabilities in a simple tubular structure. The light in tubular OFRRs propagate in the form of whispering gallery modes (WGMs) resulting of total internal reflection and constructive interference of light along the curved boundary between the high and low refractive index media.<sup>[23]</sup> WGM in the recorded light spectrum can be identified by their higher intensity originating from the superposition of frequencies matching the resonance conditions. The schematic cross-section in Figure 2.8.b illustrates the working principle of an OFRR.

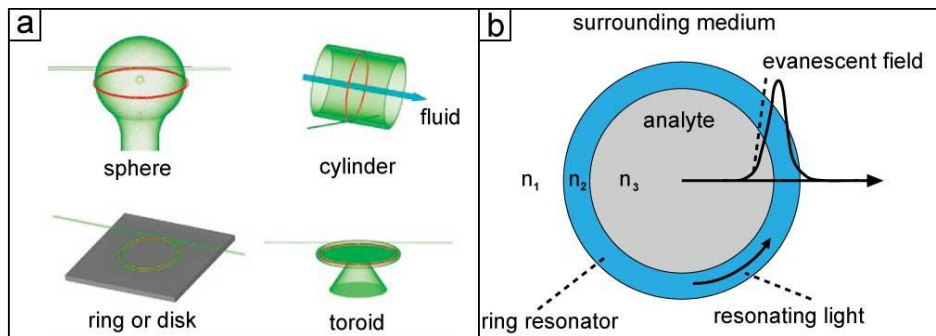


**Figure 2.8:** Schematics of ring resonators and working principle. (a) WGM resonator geometries. The WGM is highlighted in red, blue indicates microfluidic flow. (Taken from [26]) (b) Cross section of a tubular ring resonator (blue) which is filled with an analyte and surrounded by a different medium. The surrounding medium as well as the ring resonator and the analyte have their specific refractive indices  $n_1$ ,  $n_2$  and  $n_3$ . The light is confined in the ring resonator and has an evanescent field penetrating the interior and exterior medium. (Adapted from Ref. [27])

The WGMs have an evanescent field that penetrates the interior and exterior medium and respond to the changes of the refractive index inside and outside according to their resonant conditions. The position of a resonant wavelength  $\lambda_m$  in the spectrum can be calculated by:<sup>[27,28]</sup>

$$\lambda_m = \frac{2\pi R n_{eff}}{m} \quad (2.6)$$

where  $m$  is an integer number of the resonant mode,  $R$  the radius of the ring resonator and  $n_{\text{eff}} = f(n_1, n_2, n_3)$  the effective refractive index of the surrounding medium ( $n_1$ ), ring resonator ( $n_2$ ) and analyte ( $n_3$ ). The mode number  $m$  can be estimated by subtracting  $\lambda_m$  from  $\lambda_{m+1}$  using eq. (2.6) and changing the equation for  $m$  resulting in:

$$m = \frac{\lambda_m}{\lambda_{m+1} - \lambda_m} - 1 \quad (2.7)$$

The calculated value must be round up to the nearest integer number. The sensitivity  $S$  of a ring resonator to the change of the refractive index is defined by the response of the WGMs to differences in the refractive index, resulting in a shift of  $\lambda_m$  to larger or smaller wavelengths. A larger shift of the mode position is associated with a higher sensitivity. The sensitivity is defined by,

$$S = \frac{\Delta\lambda}{\Delta n} \quad (2.8)$$

Where  $\Delta\lambda = \lambda'_m - \lambda_m$  is the shift of the mode  $m$  in the PL spectrum and  $\Delta n = n'_3 - n_3$  the change of the refractive index inside the microtube. The value is given in nm/RIU (nm per refractive index unit) units. The response of the circulating light to changes in the refractive index is higher the stronger the interaction between the evanescent field and the fluid is. As long as the light can be confined in a suitable way a thinner wall and having a low refractive index medium outside the microtube leads to a stronger interaction of the evanescent field with the analyte,<sup>[29]</sup> consequently the sensitivity increases. Another possibility to increase the sensitivity of a ring resonator is to increase the quality factor (Q) of the WGMs. The Q value is defined by the linewidth of the resonant modes and is an indicator of the quality of the fabricated optical device. With increasing the Q value the light can perform more revolutions around the tubular structure without remarkable intensity losses resulting in a longer effective light path on which the light can interact with the fluid. The effective light path,  $L_{\text{eff}}$  can be calculated by,<sup>[23]</sup>

$$L_{\text{eff}} = \frac{Q\lambda_m}{2\pi n_2} \quad (2.9)$$

An example calculation demonstrate the effective light path to be  $L_{\text{eff}} = 7.7$  cm if  $Q = 10^6$ ,  $n_2 = 1.45$  RIU and  $\lambda_m = 700$  nm.

The sensitivity of a sensor is one important characteristic parameter; the detection limit (DL) is another one. The definition of the detection limit is given by:

$$DL = \frac{3\sigma_d}{S} \quad (2.10)$$

where  $\sigma_d$  is the standard deviation of the peak position of this WGM in the recorded spectrum. In general, the value of  $\sigma_d$  is a sum of all individual noise variances,<sup>[30]</sup> including amplitude noise,

temperature fluctuation and the detector's spectral resolution. High Q RR sensors are typically limited by the thermal noise whereas low Q RR sensors are limited by sensor resolution and amplitude noise.<sup>[30]</sup> Eventually, the value of the DL is an indicator of the total resolution of the RR sensor/spectrum detector system.

The main aim of this work is to integrate rolled-up microtubes as optical sensors into an on-chip microfluidic structure. Hence, it is important to be aware of influences on the optical properties of the rolled-up optofluidic ring resonators (RU-OFRRs) arising from the integration procedure. Especially influences that decrease the Q values of integrated microtubes have to be avoided.



## **3 *Methods and materials***

### **3.1 *Deposition methods***

#### **3.1.1 *Lithography***

Lithography is a method that enables the transfer of a structure from a patterned photomask to a photoactive material on a substrate by light exposure. With further processing of the photoactive layer and the substrate the structure can be transferred to the substrate. Commonly UV-light exposure is used to transfer the structure of the mask to the photoactive layer, but also x-ray and electron beam lithography is available.<sup>[31,32]</sup> The photoactive layer usually consists of polymers which are sensitive to UV-light exposure and is called photoresists. The UV-light exposure of the photoresist modifies its chemical solubility. In general, it can be distinguished between two different types of available photoresists: positive and negative photoresists. Photoresists are positive when the exposed area can be removed by a chemical developer solution and resists are negative when the exposed area is not soluble.

Due to the small wavelength of the UV-light the minimum feature size is small enough to address all requirements on the resist structures necessary in this work. Each photoresist has its own specific parameters for treatment. Usually, four main steps of treatment are always present: (i) deposition of the photoresist film on the substrate by spin-coating, where the spin-speed adjusts the film thickness; (ii) baking of the photoresist to remove the solvent and harden the film; (iii) transfer of the structure usually by a photomask consisting of silica as supporting bulk material and a chrome layer on top as the structure and finally (iv) removal of the soluble part of the photoresist by a developer solution.

Depending on the aimed application, different resists with specific properties are employed. In this work four different resists are utilized: (1) AR-P 3510 is a positive resist. This polymer is applied as a sacrificial layer for the rolled-up nanotech. (2) AZ-5214E is a positive photoresist with image reversal character, which means that with an additional backing and exposure step a thermochemical modification is applied resulting in an inversed solubility. With this inversed character this resist behaves like a high resolution negative resist containing a strong undercut.<sup>[32]</sup> This photoresist is usually utilized for lift-off techniques which is important for patterned material deposition on a substrate. (3) AZ-2070 nlof is a special negative lift-off resist suitable for thick layers and multi-layer coating. (4) SU-8 10, which is a negative resist. This resist has extraordinary properties regarding thermal stability, mechanical stability and biocompatibility and is widely utilized in fabrication methods for microelectromechanical systems (MEMS).<sup>[33,34,35,36,37]</sup>

### 3.1.2 Electron beam evaporation

This deposition method is a physical vapor deposition (PVD) to create thin films by anisotropic condensation of material on the surface of the sample. The target material is vaporized by heating of a solid source by electron bombardment at high vacuum pressures.<sup>[38]</sup> Advantages are nearly anisotropic deposition and the comfortable handling of the device.

A scheme of the employed e-beam device is depicted in Figure 3.1. The target material (Figure 3.1.a) is placed into a crucible which can be mounted into a water-cooled hearth. A thermionic filament is used as source of electrons which are accelerated at 5 kV high voltages by the anode and focused on the target by magnetic fields. The target material is heated up by the transfer of the kinetic energy of the high energetic electrons striking the target material. After reaching the material's melting point it evaporates with its specific vapor pressures and evaporation rates.

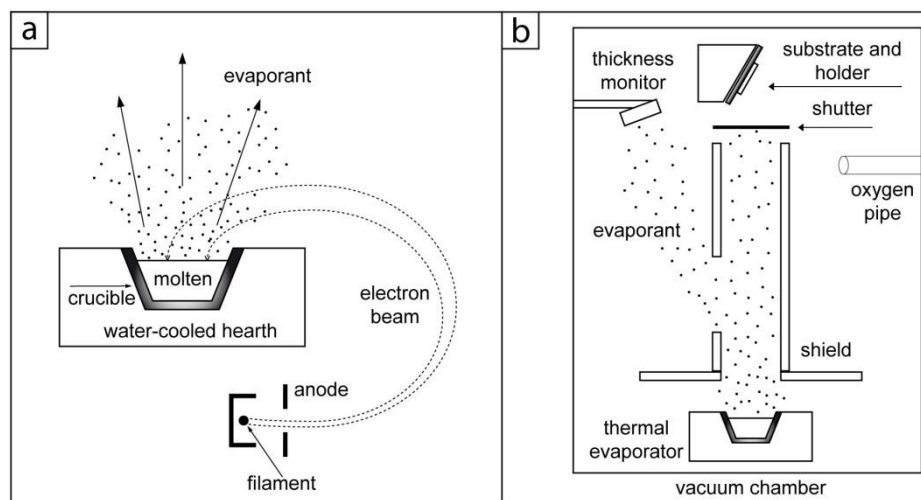


**Figure 3.1:** Overview over the BOC Edwards FL400 electron beam evaporation device. (a) Principle of evaporation of a targeted material by melting through electron bombardment. (b) Arrangement of the device components.

An overview of the design of the deposition machine is given in Figure 3.1.b. The vacuum chamber contains the evaporation unit at the bottom, a shield with a window facing the thickness monitor, an oxygen gas pipeline, a shutter and the substrate holder. The shield protects the machine and slightly collimates the evaporated material. The thickness monitor is a quartz crystal microbalance (QCM) measurement device and can detect the current deposition rate for all used materials. The thickness monitor has not the same orientation and distance to the material source as the substrate and therefore, a so called tooling factor for each material has to be calculated in order to adjust the displayed thickness on the QCM monitor to display an accurate value of the deposited thickness. The equation for the tooling factor  $F_e$  is  $F_e = F_0 \cdot T_D / T_M$  where the film thickness  $T_M$  is measured by the thickness monitor in the e-beam device and the real thickness  $T_D$

of the material on the substrate is measured by a film thickness profiler (Dektak 8 Profilometer, Veeco).  $F_0$  is the initial tooling factor usually set to the value  $F_0 = 1$ . The oxygen gas pipeline in Figure 3.1.b is used to apply an  $O_2$  background pressure to the vacuum chamber. This additional oxygen is applied during the deposition of  $SiO_2$  to ensure the deposition of almost pure  $SiO_2$ . The shutter protects the substrate during the tuning of the deposition rate and can be opened when the target rate is reached. The substrate holder can be mounted at different angles in order to adjust the glancing angle  $\alpha$  of the substrate to values from  $30^\circ$  to  $90^\circ$ . For instance, the rolling-up process in this thesis requires a glancing angle of  $30^\circ$ .

### 3.1.3 Atomic layer deposition

Atomic layer deposition (ALD) is a chemical vapor deposition (CVD) technique for isotropic material coating of polycrystalline or amorphous structures with monolayer accuracy. The principle is described in detail in Puurunen's review of surface chemistry of atomic layer deposition.<sup>[39]</sup> The deposition process can be described as a sequence of at least four characteristic cycles to coat the substrate material layer by layer. During the ALD coating process the precursors are successively introduced into the deposition chamber as a pulsed gas flux, just separated by a purging step to empty and clean the reaction chamber from the previous introduced precursor.

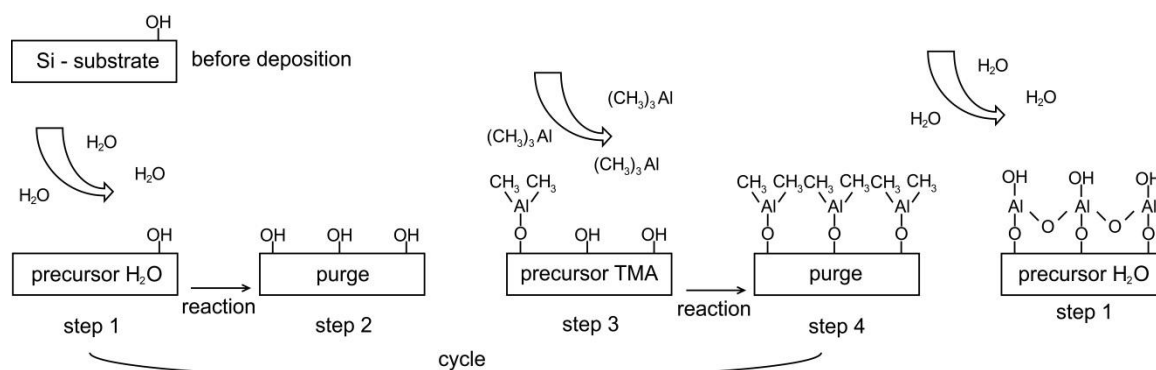


**Figure 3.2:** ALD deposition cycle. Schematic illustration of a four step water based ALD reaction cycle with the precursor TMA for  $Al_2O_3$  layers (Adapted from Ref. [40]).

A water based ALD process to deposit an  $Al_2O_3$  layer is depicted in Figure 3.2. This simple cycle sequence can be used to coat a surface with  $Al_2O_3$ . Originating from the air humidity the silicon substrate has already some chemical active hydroxide groups on the surface. During the first cycle a reactant ( $H_2O$ ) is introduced into the reaction chamber. The reactant interacts with the sample surface and covers it with OH groups. After that, the chamber is purged with an inert gas (e.g.  $N_2$ ) to clean the chamber and remove all residue reactants. The second reactant (Trimethylaluminium, TMA) is then introduced into the chamber and reacts with previously created OH-groups and

forming the first layer of the  $\text{Al}_2\text{O}_3$  material. Finally, the chamber is purged again with  $\text{N}_2$  to remove the reactants. With this deposition method the final thickness of the deposited layer depends only on the number of complete cycles.

## ***3.2 Characterization methods***

### ***3.2.1 Scanning electron microscopy***

The scanning electron microscope (SEM) enables the investigation of details on a sample that are not visible with other methods like optical microscopy. The working principle for such microscopes is well known since a long time and therefore the method can be studied in detail elsewhere.<sup>[41,42]</sup> The SEM focuses an electron beam on the sample surface and raster sequentially over a rectangular area. At every point on the raster area the electron beam penetrates the investigated material to a certain depth. Depending on the material the interaction of electrons and substrate leads to the emission of electrons which are primarily back scattered electrons (BSE) and the secondary electrons (SE). An intensity count (number of electrons) at each raster point can be measured and converted into an intensity map. BSE are useful to investigate the present elements on the sample, because BSE are created by inelastic scattering at the atoms and their deflection energy is proportional to the mass number of the element. Secondary electrons have lower energy than BSE and are emitted from the substrate near the sample surface as a side effect when the electron beam strikes the surface. The SE are very useful to study the morphology of a sample.

All samples in this work are build-up from insulator materials, causing a negative surface charge during rastering with an electron beam. Hence, the samples have to be coated additionally with a conductive layer which could be for example gold, platinum or carbon.

In this work a Zeiss NVision40 workstation is employed for the SEM studies. Prior the SEM examination, all samples are coated with 5 nm of Pt by magnetron sputtering (DCA Instruments) to enhance the surface conductivity. For a more detailed investigation on the three dimensional objects, the sample stage is rotated between  $0^\circ$  and  $90^\circ$  along the tilt-axis and freely in the x-y-plane. For investigation on the intrinsic properties of the samples, focused ion beam (FIB) cutting is utilized.

### 3.2.2 *Photoluminescence spectroscopy*

By using photoluminescence (PL) spectroscopy the energy level of electrons within the investigated material will be excited to a higher energy level by light absorption. After relaxation to the lowest energy value at this level the spontaneously recombination from this relaxed level to lower energy levels is then probable with emission of photons at material specific energies. The emitted light can be detected and contains information about the electrical structure of the investigated material.<sup>[43]</sup>

During this thesis the PL spectroscopy is utilized in a slightly modified way. The PL system is used to excite optical active defects in a tubular wall. These defects are random distributed and random in their optical characteristics, which consequences in an emission of photons whose frequencies cover the wavelength range of the white light spectrum. Depending on the geometrical properties of the microtube this emitted light propagates by total internal reflection along the circular tubular wall and certain frequencies can superpose by constructive interference. The out scattered light can be detected by the PL system and due to a higher intensity of the light at the superposing frequencies these specific wavelengths can be distinguished from the background and identified as resonant modes. These resonant modes correspond to the whispering gallery modes discussed in the *Background* chapter. In order to achieve a high intensity of the WGMs compared to the background signal the microtube is initially pumped with the excitation laser light at 442 nm for at least 3 seconds before the measurement starts. The PL system (Renishaw<sup>TM</sup>) has a build in camera with a charge coupled device (CCD) sensor for light detection and achieves a spectral resolution of 0.02 nm.

### 3.2.3 *Optofluidic setup and analytes*

This subsection is divided in two parts: the first part concerns the fluids utilized to investigate the fluidic capabilities of the microtubes and the second part focuses on the optofluidic setup for microtubes working as refractometric sensors.

#### **Part 1: dye and particle solutions**

The dye solution contains 0.1 mg mL<sup>-1</sup> Rhodamine 6G (Sigma Aldrich) dissolved in DI water. Furthermore, the solution contains 5% (v/v) isopropyl alcohol for a better solvability of the Rhodamine molecules in water. Passive filling by capillary forces is achieved by a simple self-made droplet dispenser<sup>[5]</sup> moved to an opening of the microtube and dispensing the dye solution. The active controlled fluid experiments with particles flowing through microfluidic structures are performed with a syringe pump system (neMESYS, Cetoni GmbH). During fluorescent measurements, all equipment parameter such as camera capturing time, excitation light intensity on the sample and external light are retained constant. Spherical fluorescent polymer particles

with diameters of 1.9  $\mu\text{m}$  and 0.5  $\mu\text{m}$  (Duke Scientific Corp.) are utilized as particles in the suspensions.

### Part 2: setup for microtubes as refractometric sensors

The setup consisted of the prepared chip device, a pulsation free syringe pump system (neMESYS, Cetoni GmbH, Germany) and a PL system from Renishaw<sup>TM</sup>. The micro syringe system is employed to pump the liquids in the device through the microfluidic structure. The syringes (Hamilton, 250  $\mu\text{l}$ ) are connected to the chip via polytetrafluoroethylene (PTFE) tubing with an outer diameter of 0.9 mm simply plugged into the corresponding inlet pin holes of the PDMS. The pumping velocity can be tuned from 0 to 2  $\mu\text{l}/\text{min}$  by software (neMESYS v2.50). The utilized PL system is setup with a continuous wave (CW) laser of 442 nm wavelength (He-Cd) and a standard optical microscope with long distance objectives. The chip device is plugged into a matching stage on the microscope. The whole PL system is suspended with air pressure based shock absorbers. Once the PTFE tube is sequentially filled with 2  $\mu\text{l}$  of different analytes in reverse sensing order, the tubing is plugged into the pin holes of the chip. Each segment of analyte has an air gap of 2  $\mu\text{l}$  in-between.

For this work fluids with slightly different refractive index values are chosen. The fluids are listed in Table 3.1. Deionized water is the bulk material modified by adding different components at different concentrations such as glucose or phosphate buffered saline (PBS). The refractive index of the liquids is determined by an Abbe Refractometer (Müller, Germany).

**Table 3.1** : Utilized analytes sorted by their refractive indices.

No.	Liquid	Refractive index [RIU]
1	DI water	1.3330
2	PBS	1.3345
3	PBS + 100 mM glucose	1.3369
4	PBS + 200 mM glucose	1.3394
5	PBS + 500 mM glucose	1.3472

### **3.3 Fabrication methods**

This subsection contains detailed protocols with specific parameters for the fabrication, integration and use of microtubes to enable the reader to repeat all procedures mentioned in chapters four and five.

#### **3.3.1 Fabrication of SiO<sub>x</sub> microtubes**

##### **Photolithography**

Glass substrates with lateral lengths of 22 mm and thicknesses of 160  $\mu\text{m}$  are utilized for the microtube fabrication. Prior to the spin coating process, a substrate cleaning procedure is performed in a sonication bath for 1 minute containing acetone. The acetone is removed by pouring the substrate with isopropyl alcohol. A final baking step at 120  $^{\circ}\text{C}$  for 2 minutes ends the cleaning step. A positive photoresist (AR-P 3510, Allresist GmbH) is utilized as a sacrificial layer. This resist is spin-coated on the substrate at a spin speed of  $v_{\text{sp}} = 3500$  rpm for 35 seconds to achieve a film thickness of 2.4  $\mu\text{m}$ , followed by a baking step at 90  $^{\circ}\text{C}$  for one minute on a hotplate. The photoresist pattern is transferred to the glass substrate by photolithography utilizing a mask aligner (MA56, SÜSS MicroTec AG) in contact mode. The UV-light exposure of the resist is performed for 7 seconds. The development of the exposed areas is carried out by soaking the substrate in a 1:2 (v/v) solution of the developer (AR-300 35, Allresist GmbH) and DI water for 75 seconds. The development is then stopped in DI water and finally the sample is dried by blowing the water off the sample using a nitrogen gun.

##### **Deposition of nanomembranes**

The nanomembranes (SiO, SiO<sub>2</sub> and Au) are deposited by electron beam evaporation (BOC Edwards FL400, Germany) on the previously prepared substrates. The material deposition rates are 5.0  $\text{\AA}/\text{s}$  for SiO and 0.5  $\text{\AA}/\text{s}$  for SiO<sub>2</sub> and Au. An oxygen background pressure of about  $5.8 \cdot 10^{-5}$  mbar is applied in the deposition chamber during the SiO<sub>2</sub> coating. The substrates are loaded into the chamber with a glancing angle of 30 $^{\circ}$ .

##### **Rolling-up and critical point drying**

The rolling-up of nanomembranes is performed in pure acetone where they have to be soaked for several seconds in acetone to remove the sacrificial polymer layer completely. To avoid the collapse of the microtubes caused by surface tension forces during solvent evaporation, the samples are dried in a super critical point dryer (CPD). The acetone in the CPD chamber is replaced by liquid CO<sub>2</sub> at 10  $^{\circ}\text{C}$  until the chamber pressure reached 50 bar. Once the pressure is stable and no acetone is left in the chamber, the CPD chamber is heated up to 42  $^{\circ}\text{C}$  to turn the

phase of the CO<sub>2</sub> beyond the supercritical point. Once the temperature is constant and the chamber pressure is stable at about 90 Bar, the CO<sub>2</sub> is gassed out while maintaining the temperature at 42 °C.

### 3.3.2 *On-Chip integration of SiO<sub>2</sub> microtubes*

#### **Step 1: substrate preparation**

Transparent D263T 4 inch glass wafers (Siegert Consulting e.K., Germany) with a thickness of 500 µm are cut into square pieces with a lateral length of 22 mm to fabricate a base substrate. The alignment structures which are necessary for many device fabrication steps are created onto the substrate by a lift-off technique. Prior to the photoresist processing step the substrate is baked at 120 °C for 5 minutes on a hotplate to remove the surface humidity. After cooling down, the photoresist AZ-5214E (Microchemicals GmbH, Germany) is spin-coated at 6000 rpm for 35 seconds onto the substrate with a following baking step over 4 minutes at 90 °C on a hotplate. The photomask with the alignment structures is then brought into line with the edges of the substrate by using the mask aligner MA 56 (SÜSS MicroTec AG, Germany) working in contact mode. The transfer of the structures to the photoresist is performed by exposing the resist with UV-light for 2 seconds followed by a reversal baking step on a hotplate at 120 °C for 2 minutes. A second flood exposure with UV-light for 30 seconds establishes the transferred structure in the photoresist. The development of the structure is done in pure AZ 726 MIF developer (Microchemicals GmbH, Germany) for 20 seconds, the development reaction is stopped afterwards in a DI water bath. The substrate is dried under a gaseous nitrogen flux.

The substrate and a chrome material target are loaded into an electron beam evaporator (BOC Edwards FL400, Germany). The face of the substrate with the photoresist pattern is orientated directly towards the material source. After the vacuum in the deposition chamber reached  $1 \cdot 10^{-6}$  mBar the deposition of 10 nm Cr is done at 1 Å/s. Once the substrate is unloaded the lift-off process is completed in an ultra-sonic bath for one minute with acetone as resist etchant. The acetone is washed off the sample with isopropyl alcohol and then dried with a nitrogen gun.

The so-called socket structures are then fabricated on the substrate at a defined position in the center of the sample by a two-step photolithography process utilizing the negative photoresist SU-8 10 (MicroChem, MA, USA). Prior to the first lithography step a dehydration baking step at 120 °C for 5 minutes on a hotplate is performed. Then, the first layer of the resist is spin-coated at 5000 rpm to produce a 5 µm thick layer onto the substrate. The baking process for SU-8 closely followed the company's recommendations. Therefore, a ramp baking step is established starting with heating up from 50 °C to 90 °C at 3°C per minute on a hotplate. This temperature is held for 15 minutes followed by slowly cooling down to 50 °C at about 3 °C per minute. The first part of

the socket structure is transferred by a 30 second UV-light exposure at 365 nm from a photomask to the photoresist using the mask aligner MA 56. A second baking step, similar to the one before, finished the cross-linking within the photoresist. The development of the structure is done in pure mr-DEV 600 developer for 180 seconds and is stopped in isopropyl alcohol. Afterwards the substrate is dried under a gaseous nitrogen flux. The second SU-8 10 layer is spin-coated at 2000 rpm to fabricate a 15  $\mu\text{m}$  thick layer onto the first processed SU-8 structure. The transfer of the second part of the socket structure, the development and the baking times are performed with similar parameters as for the first SU-8 layer, but with another photomask structure. An additional thermal cross-linking step following a temperature ramp is performed on each SU-8 layer separately. The ramp started at 50  $^{\circ}\text{C}$  on a hotplate, then the temperature is set to 180  $^{\circ}\text{C}$  with a heating up speed of 3  $^{\circ}\text{C}$  per minute. Once it reached 180  $^{\circ}\text{C}$ , this temperature is maintained for 10 minutes. The cooling down to 50  $^{\circ}\text{C}$  is achieved at a rate of 3  $^{\circ}\text{C}$  per minute as well.

### **Step 2: fabrication of the free-standing $\text{SiO}_2$ microtubes**

A clean square Si-wafer with lateral dimensions of 10 mm is utilized as a substrate for the microtube fabrication. This substrate is cut out of a 4 inch Si-wafer. After a dry baking step at 120  $^{\circ}\text{C}$  for 10 minutes on a hotplate the photoresist ARP-3510 (Allresist GmbH, Germany) is spin-coated on the substrate at 3500 rpm to establish a 2.4  $\mu\text{m}$  thick resist layer. After that, a baking step at 90  $^{\circ}\text{C}$  for 5 minutes is performed on a hotplate to remove the solvents of the resist. The patterning with the roll-up structure is achieved with a matching chrome photomask and the mask aligner MA 56. After patterning the photoresist the structures are developed in a 1 to 1 (v/v) mixture of DI water and AR-300 35 developer solution for about 45 seconds. The development is stopped in pure DI water. After drying the sample under a gaseous nitrogen stream, the sample is loaded into an e-beam evaporator (BOC Edwards FL400, Germany) at a glancing angle  $\alpha$  of 30 $^{\circ}$  with the material target  $\text{SiO}_2$ . Once the vacuum of the chamber reached  $1 \cdot 10^{-6}$  mBar the deposition of the bi-membrane is started with 10 nm  $\text{SiO}_2$  at 15  $\text{\AA}/\text{s}$  and 60 nm  $\text{SiO}_2$  at 0.5  $\text{\AA}/\text{s}$ . After cooling down and unloading the e-beam evaporator the rolling-up of the deposited membranes is performed in a beaker with pure acetone which selectively etched the photoresist and released the bilayer. The microtube fabrication procedure finishes with a critical point drying step. Therefore the substrate quickly is moved from the beaker to the CPD chamber filled with fresh acetone. The acetone is replaced by liquid  $\text{CO}_2$  at 10  $^{\circ}\text{C}$  and 50 Bar. After heating up to 42  $^{\circ}\text{C}$  and above the critical point at 90 Bar the supercritical  $\text{CO}_2$  is gassed out slowly. The dried Si-substrate then contains free-standing rolled-up microtubes which are characterized and transferred during the next step.

### **Step 3: microtube characterization and transfer**

The free-standing microtubes are characterized with a photoluminescence spectroscopy system (Renishaw<sup>TM</sup>) according to their resonant spectrum properties and optical quality in a wavelength range from 400 to 800 nm. A sample map is prepared to visualize the properties of all microtubes in one view. The transfer of the microtubes is carried out with a pulled glass capillary mounted on a three-dimensional (3D) micromanipulator utilizing a standard optical microscope. After pulling the glass capillary under heat, the tip achieved a diameter of about 5  $\mu\text{m}$ . The tip is moved close to a microtube selected for transfer and with gently applied mechanical forces the microtube could be detached and moved to a socket on the target substrate prepared in step 1. Each pair of sockets has trenches in which a microtube can be placed and wiped off.

### **Step 4: microtube fixing and preparation**

The transferred microtube is bonded to the sockets and stabilized mechanically by atomic layer deposition of 10 nm  $\text{Al}_2\text{O}_3$ . The deposition chamber of the ALD machine (Savannah<sup>TM</sup> 100, CambridgeNanoTech Inc.) is set to 80  $^\circ\text{C}$  prior to loading the substrate with the transferred microtubes. After loading the substrate into the deposition chamber the temperature is set to 150  $^\circ\text{C}$  with a heating up rate of about 1  $^\circ\text{C}$  per minute. Once the temperature is stabilized an isotropic deposition of  $\text{Al}_2\text{O}_3$  is performed. The number of cycles is 110 and the utilized precursors are trimethylaluminum (TMA, Sigma Aldrich) and DI water. Pulse duration and waiting times between the pulses are set according to the recommendations for this material, which are pulses over 0.015 second for each precursor and waiting times of 20 seconds between each pulse. When the coating is finished, the deposition chamber is cooled down to 80  $^\circ\text{C}$  with less than 1  $^\circ\text{C}$  per minute.

The next part of step 4 involved the deposition of UV-light protector caps on top of the microtubes. This processing step requires a thick lift-off resist (AZ-2070 nlof) layer due to the size of the microtubes. The following coating procedure is repeated three times to achieve an appropriate layer thickness of 24  $\mu\text{m}$ . First the resist is spin-coated at two velocities: (i) at 3000 rpm for 35 seconds and (ii) at 5000 rpm for 2 seconds. A soft bake step at 60  $^\circ\text{C}$  for 60 seconds is required to harden the resist slightly. The second and the third layer are coated with the same temperature settings and baking times. Another soft bake after the third coating step at 110  $^\circ\text{C}$  for 30 seconds completes the resist coating procedure. An intermediate step is performed to remove the borders of the resist and to gain a flat surface. To remove the border of the resist the sample is rotated at 1000 rpm in the spin-coater for about 10 minutes. A syringe filled with 10 ml of developer AZ 836 MIF is utilized to pour the developer gradually on the outer part of the sample until the resist on the border is dissolved completely. The drying of the sample is achieved by

spinning it for 30 seconds at a speed of 5000 rpm. A final soft bake step at 110 °C for 30 seconds on a hotplate is required to evaporate residues of the developer and to harden the resist. The photomask structure containing the protector caps is aligned to the markers on the glass substrate by using the Mask Aligner MA6 (SÜSS MicroTec AG, Germany). The exposure time is 50 seconds with UV-light (365 nm). The post exposure bake (PEB) for cross-linking the exposed resist is performed on a hotplate at 110 °C for 1 minute. The development is performed in pure AZ 826 MIF developer for 300 seconds at room temperature. The development is stopped in a DI water bath followed by a drying step of the substrate with gaseous nitrogen.

Prior to depositing the material for the protector caps an additional shadow mask (aluminum foil) is mounted on the substrate. This shadow mask covers and protects the entire sample except a small area where the material for the caps is supposed to be deposited. The deposition of the protector caps is performed using an e-beam evaporator. The substrate and the target materials Cr, Au and SiO<sub>2</sub> are loaded into the machine. The surface of the substrate is facing directly the material source. After the vacuum in the deposition chamber reached  $1 \cdot 10^{-6}$  mbar the target materials are deposited in the following order and thickness: Cr, Au, Cr and SiO<sub>2</sub> (5/50/5/10 nm) at 0.5 Å/s each. The substrate is unloaded after cooling down. Once the additional aluminum foil shadow mask is removed, the lift-off process is completed in dimethylsulfoxid (DMSO) at 60 °C over 5 minutes. Finally, the sample is cleaned in a DI water bath and dried using a N<sub>2</sub> gun.

### **Step 5: fabrication of the microchannel system**

The microfluidic channel system is fabricated using the negative photoresist SU-8 10. Prior coating the photoresist SU-8 10 the substrate is pre-baked on a hotplate at 120 °C for 5 minutes. Once the substrate is cooled down to room temperature, the resist is spin coated at 1500 rpm for 35 seconds onto the substrate to fabricate a channel height of about 20 µm. A ramp baking step, starting with heating up from 50 °C to 90 °C at 3°C/min on a hotplate, removes the solvent and hardens the coated resist. The temperature of 90 °C is maintained for 15 minutes followed by a slow cooling down to 50 °C at about 3 °C/min. Once the photomask is aligned to the substrate utilizing the MA 56 aligner, the microchannel structure is transferred to the photoresist by UV-light exposure at 365 nm for 40 seconds. A second baking step, similar to the one before, finishes the polymerization of the photoresist. The development of the structure is done in pure mr-DEV 600 developer for 180 seconds. The development reaction is stopped in isopropyl alcohol. Finally, the substrate is dried under a gaseous nitrogen stream. After a thermal cross linking step at 180 °C (as described in step 1), the photoresist is very stable and shows no remarkable swelling behavior when in contact with liquids.

**Step 6: final chip assembly**

The substrate containing the microfluidic SU-8 structure on top is loaded into an electron beam evaporator together with the material target SiO<sub>2</sub>. The substrates' loading angle  $\alpha$  is 90°, so that the SU-8 structure faces the material source directly. After reaching the working pressure of about  $1 \cdot 10^{-6}$  mBar in the deposition chamber, the deposition of 5 nm SiO<sub>2</sub> at 0.5 Å/s is completed. After unloading the substrate, it is prepared for O<sub>2</sub> plasma bonding. The system-closing lid preparation is achieved by utilizing a fresh polydimethylsiloxan (PDMS, Sylgard 184 Silicone Elastomer KIT, Dow Corning, MI, USA) mixture (1:10) poured into an square shaped aluminum frame of 15 mm side length and 5 mm height placed on a blank Si wafer. The PDMS mixture is cured for 20 minutes at 100 °C. Once the frame with the PDMS is cooled down, the PDMS is peeled off the Si wafer, the in- and outlet channels in the PDMS are defined by drilling pin holes with a cutting needle (Harris, Uni-Core, 0.75 mm inner diameter) matching the position of the inlets of the microchannel system on the substrate. The final assembly to activate the surfaces of the substrate and the PDMS is performed with an oxygen plasma treatment for 30 seconds at 30 watt and an O<sub>2</sub> flux of 15 sccm. Once the surfaces are activated, the holes in the PDMS lid are well aligned to the inlets on the substrate and then the lid is gently pressed on the substrate to establish the permanent bonding.

## ***4 Scaling of SiO<sub>x</sub> microtubes and potential applications***

This chapter is based on the publication Harazim et al. [10] in the Journal of Materials Chemistry. Expressions and segments taken from this reference are not cited separately.

In this section of the thesis the fabrication of large arrays of multifunctional biocompatible SiO/SiO<sub>2</sub> (general SiO<sub>x</sub>,  $x = 1 \dots 2$ ) microtubes by utilizing the rolled-up nanotech will be discussed. The outer tubular diameter as a function of the thicknesses of SiO and SiO<sub>2</sub> are systematically studied and the roll-up parameters are optimized to deterministically achieve a yield of nearly 100%. A macroscopic continuum mechanical model is in good agreement with the experimental data. The relative ease in functionalization of the “glass” microtubes with different biomaterials renders rolled-up nanotech an excellent option for various on- and off-chip applications, including microfluidic integration, micro-engines and pre-patterned 3D scaffolds for cell culturing.

### ***4.1 Introduction***

The deterministic fabrication of a large number of uniform tubular structures is of interest in fields such as materials science, chemistry, bio- and nanotechnology. Recently, the fabrication of tubular microstructures is successfully exploited in optofluidics,<sup>[13,25]</sup> (bio)-sensing,<sup>[44-47]</sup> catalytic microjet engines,<sup>[48-55]</sup> magnetic sensors<sup>[56]</sup> and 3D cell microreactors,<sup>[11,57-59]</sup> to name a few. It has been demonstrated that nanomembranes composed of various materials and material combinations, such as semiconductors,<sup>[1,2]</sup> metals,<sup>[9]</sup> oxides<sup>[9]</sup> and magnetic materials,<sup>[56,60]</sup> can be efficiently rolled-up into tubular structures. Despite the variety of works found in the literature, a systematic study of the parameters defining the diameter of the microtubes is only carried out for semiconductor tubes<sup>[61]</sup> and Si<sub>x</sub>N<sub>y</sub> and Ti tubes on polymers.<sup>[9]</sup>

However, for rolled-up glass microtubes, diameter scalability, hybrid functionalization and long-term biocompatibility have not been investigated in detail yet. By controlling the thicknesses of the deposited layers and therefore exerting precise control over the diameter of the tubes, plenty of applications are demonstrated and envisioned, which rely on an extremely high yield fabrication process. In this chapter the fabrication of transparent SiO/SiO<sub>2</sub> rolled-up microtubes is presented, with a yield close to 100% and with a deterministic control of the tubular diameter by modifying the bi-layer arrangement and thickness. The fabricated microtubes have diameters ranging from 1 to 12  $\mu\text{m}$ . The experimental data are well consistent with a semi-empirical theory and can be fitted for all layer compositions. The SiO and SiO<sub>2</sub> microtubes offer several interesting features such as optical sensor capabilities, biocompatibility and low-cost production.<sup>[11,13]</sup>

Therefore a range of different applications can be foreseen including the integration in microfluidic devices,<sup>[62]</sup> self-propelled microengines and cell biophysics in tubular confinements.

## 4.2 Microtube fabrication

This section discusses the concept of fabricating numerous rolled-up SiO<sub>x</sub> microtubes on a single substrate. The substrate is a glass slide with a size matching in standard sockets of inverse and upright optical microscopes. In general, the substrate can consist of many materials such as silicon, polymers or ceramics.

On this glass substrate the sacrificial layer (photoresist) for rolling-up is spin coated. This resist should provide certain requirements such as a suitable adhesion to the substrate material and a smooth surface with a low as possible roughness. Before measuring the characteristics of the photoresist, it is patterned into squares with side lengths of 50 μm. The photoresist structure shown in the left SEM image of Figure 4.1 depicts a structure of the sacrificial layer after the development typical for positive photoresists when they are in contact to a photomask during UV light exposure.<sup>[32]</sup>

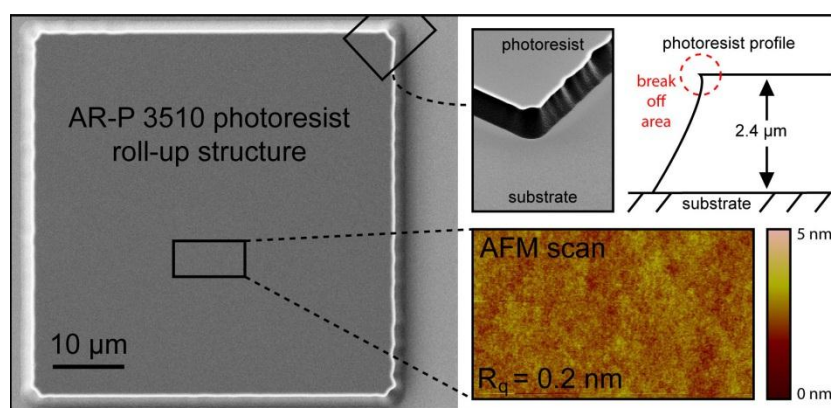


**Figure 4.1:** The roll-up pattern. The SEM image on the left site depicts a characteristic roll-up AR-P 3510 structure before the deposition of SiO and SiO<sub>2</sub>. The inset on the up-right site depicts a zoomed and tilted view on one of the corners of the photoresist. The associated cross-section depicts a typical profile at the corner of the resist. The red dashed circle highlights the so called break off area. The AFM scan in the lower right inset depicts a scanned area 10 by 5 μm on top of the resist, marked by the black square in the left SEM image. The surface roughness of the resist is calculated to  $R_q=0.2$  nm (Taken from Ref. [10]).

The upper right inset of Figure 4.1 depicts a zoomed SEM view to one corner of the pattern including a cross section to highlight the slope of the wall of the resist. The two SEM images of Figure 4.1 are taken by using the secondary electrons. This scanning mode is utilized to scan the surface morphology of a sample, whereby thin structures or edges, such as the small overhang in the break off area (red dashed circle), shine brighter compared to planar surfaces. The bright

frame around the resist structure indicates the presence of this overhang. The mask aligner works in contact mode and therefore, light scattering at the edge of the mask guides light in low doses underneath the mask. Consequently, the overhang is more pronounced at longer exposure times. The shape of the resist in the break off area has a major influence on the rolling-up process and the adhesion of the microtube to the substrate after the roll-up process.

Electron beam evaporation cannot provide a perfectly collimated material beam. This and due to ballistic scattering of the evaporated material the shadow in the break off area is diffuse. With a very short exposure time the overhang does not create a shadow and the deposited membrane is not interrupted. Consequently the membrane is fixed to the substrate at three sides. A strong pronounced overhang (after a long exposure time) leads to a membrane with a loose adhesion to the substrate on all four sides of the square pattern. The membrane will roll-up but the resulting microtube will be washed away by the etchant of the sacrificial layer. Consequently, an optimum exposure time seems to be mandatory for the roll-up process in order to create large arrays of rolled-up microtubes sticking to the substrate. Different exposure times can be utilized to target different requests such as applications where immobile tubes are required (shorter exposure time) or off-chip applications like microjets (longer exposure time).<sup>[10]</sup>

The fabrication of  $\text{SiO}_x$  microtubes relies on the deposition of strained nanomembranes whose deposited thicknesses are in the lower nanometer regime. These nanomembranes require a smooth as possible sacrificial layer in order to minimize the effect of transferring the topology of the surface to the deposited membrane. Small defects of too rough surfaces can destroy the directed stress relaxation leading to an uncontrollable roll-up process, with chances of not rolling at all. Therefore, several polymers are investigated regarding their surface properties and the AR-P 3510 resist is found to be the most suitable one for the roll-up process. The surface roughness of this photoresist is depicted in Figure 4.1 and is  $R_q=0.2$  nm (root mean square roughness) measured by atomic force microscopy (AFM).

Once suitable parameters for the substrate and the sacrificial layer are worked out, the substrate with the patterned surface is loaded at a glancing angle of  $\alpha = 30^\circ$  into the electron beam evaporator. This loading angle and the height of the sacrificial layer of about  $2.4 \mu\text{m}$  lead to an uncoated window at the far end of the photoresist compared to the material source as indicated in Figure 4.2. The angle of  $30^\circ$  is optimized for  $\text{SiO}_x$  microtubes on polymers. Nanomembranes based on other materials can also be deposited at different angles.<sup>[48,53]</sup>

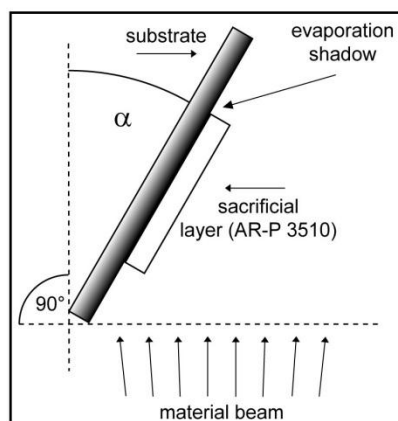


**Figure 4.2:** Schematic view on the sample holder in the electron beam evaporation device. The tilting angle  $\alpha$  can be changed between  $0^\circ$  and  $90^\circ$ , whereby  $90^\circ$  means that the resist on the substrate faces the material beam directly. The evaporation shadow of the sacrificial layer (AR-P 3510) is at the far end compared to the material target.

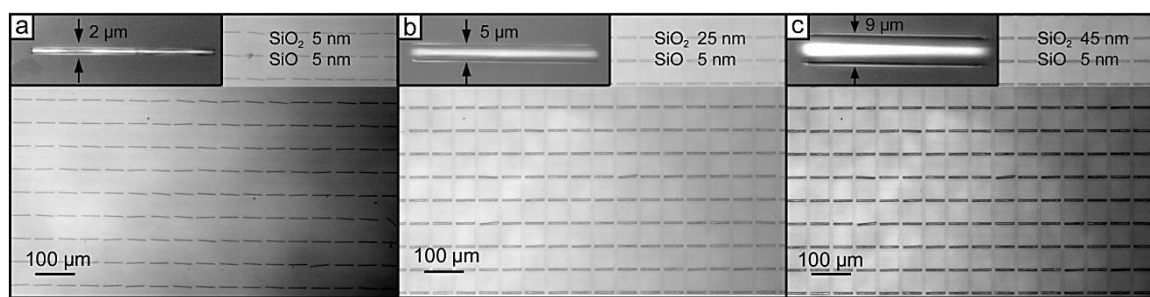


**Figure 4.3:** Arrays of rolled-up microtubes. Optical images of three different arrays containing rolled-up SiO/SiO<sub>2</sub> microtubes with different outer diameters corresponding to the different mono-layer thickness compositions of SiO and SiO<sub>2</sub>: (a) the diameter is 2  $\mu\text{m}$  for 5/5 nm (SiO/SiO<sub>2</sub>); (b) 5  $\mu\text{m}$  for 5/25 nm and (c) 9  $\mu\text{m}$  for 5/45 nm. The insets depict a close view to one of the microtubes on the corresponding sample (Taken from Ref. [10]).

The optical images in Figure 4.3 depict several arrays of rolled-up SiO/SiO<sub>2</sub> microtubes on a glass substrate fabricated by the deterministic rolled-up nanotech. The fabrication parameters are carefully adjusted to gain a rolling-up yield of well aligned microtubes of almost 100 % for all bi-layer compositions of SiO and SiO<sub>2</sub>. The tuning of the diameter is achieved simply by changing the thickness of the SiO<sub>2</sub> layer while maintaining the thickness of the SiO layer at a specific value. The insets depicted in Figure 4.3 show zoomed views on a single microtube from the corresponding array. These three array-examples are characteristic for all investigated bi-layer compositions and contain about 200 microtubes, well aligned (Figure 4.3.a-c) and with diameters of 2, 5 and 9  $\mu\text{m}$ , respectively.

The examples shown in Figure 4.3 illustrate how the diameter tuning is carried out: the SiO layer is the ground layer which provides the strain for rolling-up while the SiO<sub>2</sub> layer acts as the moderator of the diameter. A thicker layer of SiO<sub>2</sub> has a higher resistance against the strain

relaxation of the SiO layer than a thinner SiO<sub>2</sub> layer and therefore, the diameter increase with a thicker SiO<sub>2</sub> nanomembrane. In order to fabricate microtubes with a diameter of 2 μm, a bilayer composition of 5 nm SiO and 5 nm SiO<sub>2</sub> is required. By increasing the thickness of the SiO<sub>2</sub> membrane to 25 nm the outer diameter of the rolled-up tube increases to 5 μm (Figure 4.3.b). If the thickness of the SiO<sub>2</sub> membrane is set to 45 nm, the tubular diameter increases to 9 μm. A detailed look on the rolled-up microtubes, an investigation on a larger set of bi-layer compositions and their capabilities for fluidic investigations will be discussed in the following chapter.

### 4.3 Characterization of rolled-up microtubes

The fabrication process described in the previous section enables the tuning of the diameter of a SiO<sub>x</sub> microtube by modifying the composition of the SiO/SiO<sub>2</sub> bi-layer membrane. An example of a microtube with the smallest achieved diameter is given in the SEM image of Figure 4.4. The entire microtube is depicted in Figure 4.4.a whose outer diameter is about 1.2 μm. The zoomed view to the end of this microtube shows that this rolled-up microtube has a compact rolled wall with just a small mismatch between the single windings. The wall (marked by yellow arrows) is made of SiO<sub>x</sub> and follows the former shape of the sacrificial layer. The position of the microtube after rolling-up shown in Figure 4.4 is typical for many microtubes. For larger tubes (e.g. diameter larger than 10 μm) microtubes can roll over the wall and lay on the substrate.

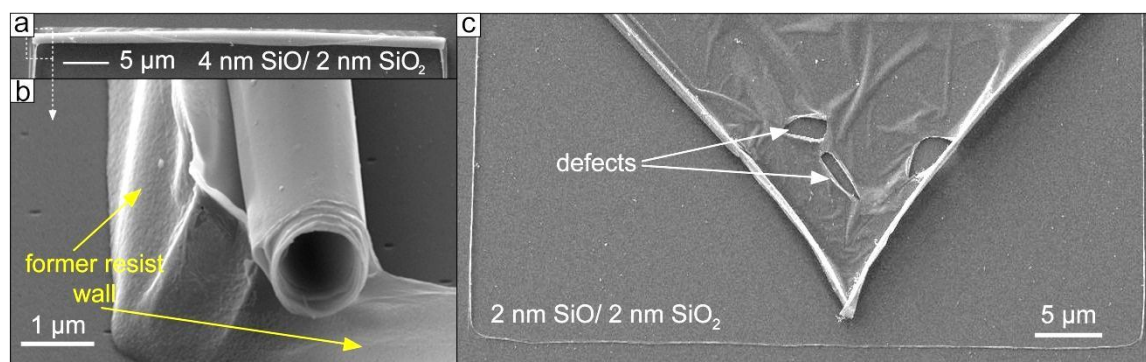


**Figure 4.4:** SEM images of a rolled-up microtube. (a) Overview on a 50 μm long SiO/SiO<sub>2</sub> microtube with a diameter of about 1 μm. The bi-layer composition is 4/2 nm (SiO/SiO<sub>2</sub>). (b) Close view with a cross-section of the end of this rolled-up microtube (Taken from Ref. [10]). The arrows point on the overhang (red) and the former photoresist walls (yellow). (c) SEM image of a very thin bi-layer 2/2 nm (SiO/SiO<sub>2</sub>) after the roll-up procedure.

The minimum diameter is so far limited by the ability to build-in strain by electron beam evaporation. It is observed that for thinner membranes than for the microtube depicted in Figure 4.4.a the rolling-up process loses its directionality and defects in the membrane can destroy the membrane as depicted in Figure 4.4.c for a membrane made of 2 nm SiO and 2 nm SiO<sub>2</sub>. A larger diameter can be achieved by increasing the bi-layer thickness. The maximum diameter is limited by the size of the used pattern which is in particular 50 μm in side length. The maximum diameter

which can be provided by this structure is calculated to 15.9  $\mu\text{m}$  by dividing the side length by  $\pi$  according to the relationship between diameter and circumference of a circular structure. In general, larger diameters are possible with longer distances along the rolling-up direction. These large microtubes are topic of current research of our group at the IIN. An example of an application of utilizing these large microtubes as artificial cavities for single cell studies will be given in the chapter of the applications of SiO<sub>x</sub> microtubes on page 37. The tuning of the diameter is investigated for six different thick SiO membrane thicknesses with a set of different SiO<sub>2</sub> layer thicknesses for each of these SiO membranes. The summary on this investigation including a theoretical fit is plotted in Figure 4.5.

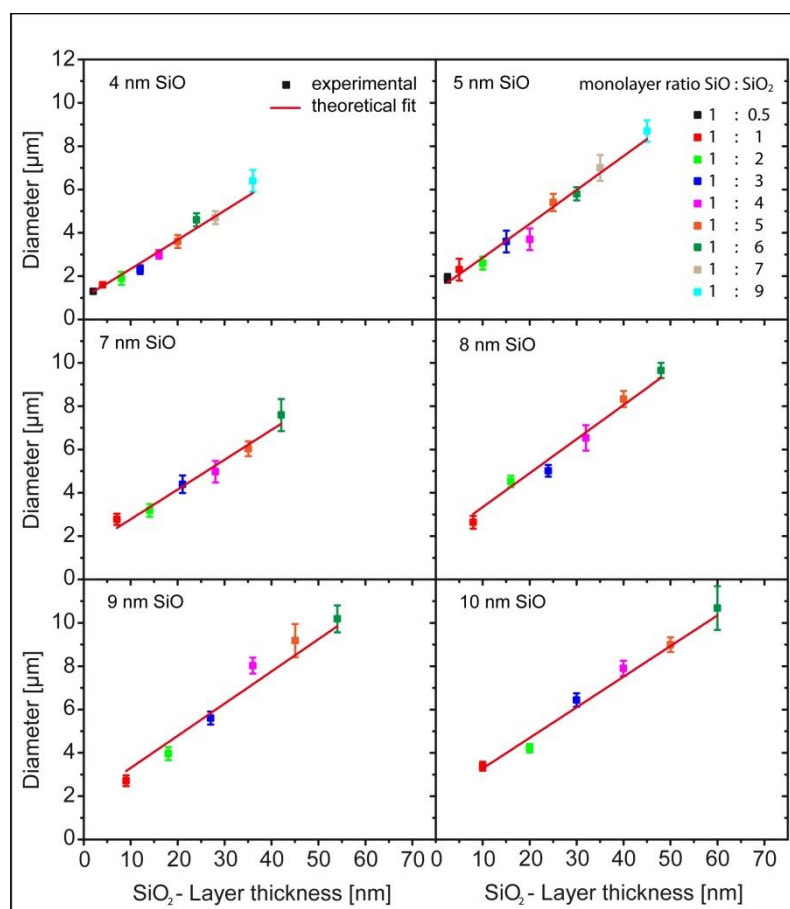


**Figure 4.5:** Diameter of microtubes at different bilayer compositions. Dependence of the diameter of SiO/SiO<sub>2</sub> microtubes on the SiO<sub>2</sub> monolayer thickness for six different thicknesses of SiO. The monolayer thickness of SiO ranges between 4 and 10 nm. The colors of the data-points are correlated to discrete monolayer thickness ratios between the SiO and SiO<sub>2</sub> mono-layer. The ratio ranges from 1:0.5 to 1:9. A theoretical fit (red line) is plotted for each set of monolayers (Taken from Ref. [10]).

Based on a macroscopic continuum mechanical model suitable for a bilayer system where the two layers have almost the same Young modules, the following equation can be used to calculate the diameter of the rolled-up tubes:<sup>[63,64]</sup>

$$D = \frac{d_1^4 + 4jd_2d_1^3 + 6jd_1^2d_2^2 + 4jd_1d_2^3 + d_2^4j^2}{3\epsilon j(1+\nu)d_1d_2(d_1+d_2)} \quad (4.1)$$

where  $D$  is the outer tubular diameter,  $d_1 \equiv \text{SiO}$  and  $d_2 \equiv \text{SiO}_2$  are layer thicknesses,  $\nu$  is the Poisson ratio of  $\text{SiO}_x$  ( $\nu=0.2$ ),<sup>[65]</sup> the Young's modulus ratio is expressed by  $j=Y_1/Y_2$  and  $\epsilon$  is the in plane biaxial strain of the bi-membrane. By assuming that the Young's moduli of SiO and SiO<sub>2</sub> are almost equal, equation (4.1) can be shortened to:

$$D = \frac{1}{3\epsilon(1+\nu)} \frac{(d_1+d_2)^3}{d_1d_2} \quad (4.2)$$

To simplify the mathematical calculation  $d_1$  is set as a constant. Figure 4.5 shows the diameter of the microtube as a function of the SiO<sub>2</sub> layer thickness for different SiO monolayer thicknesses varying from 4 to 10 nm. Each set of data-points with the same color code denotes a fixed SiO : SiO<sub>2</sub> nanomembrane thickness ratio ranging from 1 : 0.5 to 1 : 9. The measured diameters are collected by optical microscopy at 100x magnification and the error bars are estimated by performing a statistical calculation (standard deviation, 95% confidence) for  $n = 50$ . The theoretical fits in Figure 4.5 are obtained by using Equation (4.2) and fitted to the data distribution.

Studies on the rolled-up microtubes with different diameters about their fluidic capabilities can show that SiO<sub>x</sub> microtubes could be employed as capillaries to move fluids on-chip as already demonstrated for other more expensive and toxic material systems.<sup>[66,67]</sup> In order to prove the fluidic capabilities of these SiO/SiO<sub>2</sub> microtubes two different fluids are employed. There is first a simple dye solution containing Rhodamin 6G and second a suspension of fluorescent polymer particles. Each column in Figure 4.6 depicts a selected microtube with diameters of 1.8  $\mu\text{m}$ , 3.6  $\mu\text{m}$  and 6.5  $\mu\text{m}$ , respectively.

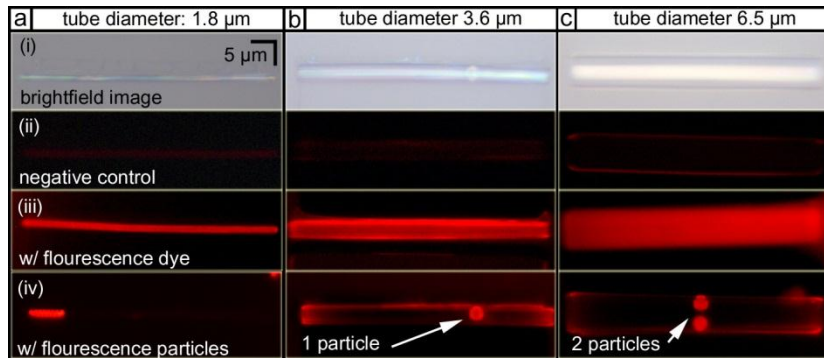


**Figure 4.6:** Investigation on the fluidic capabilities of microtubes. The optical images show bright field (i) and fluorescence (ii–iv) pictures of microtubes with different diameters (a–c). The utilized dye solution contains Rhodamine 6G while the suspension contain fluorescent spherical polymer particles with diameters of 0.5  $\mu\text{m}$  in (a) and 1.9  $\mu\text{m}$  in (b) and (c) as well. Three different fluorescent conditions are displayed: (ii) negative control before liquid filling; (iii) filled with dye solution; and (iv) confinement of fluorescent microparticles (Taken from Ref. [10]).

The images are taken in the bright field and fluorescence setting of the microscope. The fabricated SiO/SiO<sub>2</sub> microtubes show a slight fluorescent signal as it can be seen in row (ii) of Figure 4.6 which might be originated from Si-clusters embedded in the SiO layer.<sup>[68,69]</sup> After dispensing the Rhodamine 6G dye solution with a micropipette onto the samples, all microtubes are easily filled with the fluid by capillary forces.(Figure 4.6, row iii).

The confinement of fluorescent polymeric microparticles with diameters of 1.9  $\mu\text{m}$  for the larger microtubes and 0.5  $\mu\text{m}$  for the small microtubes is also demonstrated in Figure 4.6 (iv). Prior to dispensing the suspension on the microtubes they are washed in isopropyl alcohol several times to remove the residual dye as much as possible. Depending on the tubular diameter, single or multiple particles (Figure 4.6.a-c row iv) are observed within the microtubes. The results demonstrate that the fabricated SiO/SiO<sub>2</sub> microtubes can easily be filled with fluids or even particles.

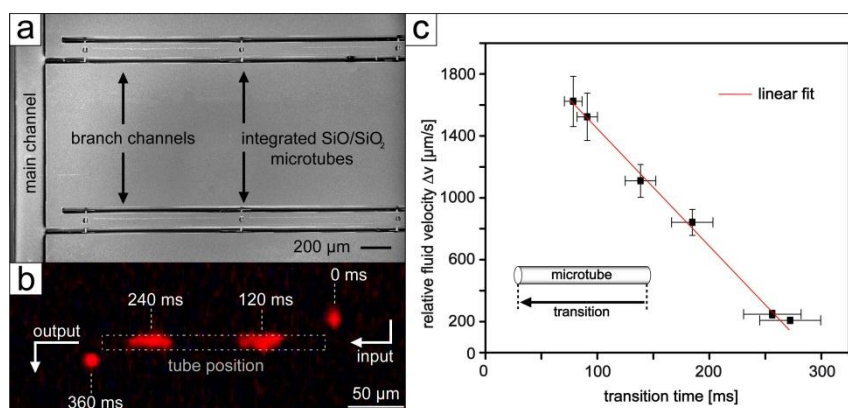


**Figure 4.7:** In-flow studies with integrated microtubes. (a) SEM of a microtube array integrated into a photolithography defined SU-8 10 microfluidic structure. The branch channels connect the microtubes and are supported by the main channel. (b) Merged fluorescence image sequence of a particle transfer between the branch channels through a microtube. (c) Different particle transition times depending on relative difference of the liquid velocity  $\Delta v$  in the connected branched channels (Taken from Ref. [10]).

The integration of the microtubes into a microfluidic structure as shown in Figure 4.7 extends the applicability of these microtubes to a more controllable way of handling fluids. The SEM image in Figure 4.7.a depicts several SiO/SiO<sub>2</sub> microtubes integrated into a microfluidic chip fabricated by photolithographic structuring of the SU-8 polymer. The main channel on the left side connects to the branched channels, which are bridged by the integrated microtubes. Though this channel system fluids can be pumped through. The visualization of the fluid flow is carried out with fluorescent particles. This suspension of spherical polymer particles is pumped through the system by an external syringe pumping system. The fluorescence image depicted in Figure 4.7.b shows a sequence of fluorescence images merged into one frame of one particle with a diameter

of about 1.9  $\mu\text{m}$  which is passing the microtube from the right branched channel to the left one. The microtube position is highlighted by the grey dashed rectangular frame in Figure 4.7.b.

The required pressure gradient between the bridged channels can be achieved by alternating the liquid velocity by pumping at the inlet (overpressure,  $v_{in}$ ) and extracting at the outlet (negative pressure,  $v_{out}$ ). Therefore it is possible to tune the speed of the transfer of the particle through the integrated microtube as shown in Figure 4.7.c. The relative fluid velocity  $\Delta v$  is calculated by the difference of the fluid speed in the branched channels:  $\Delta v = |v_{in} - v_{out}|$ . The transition time of the particle through the tube is calculated by using the image capture time of the camera (80 ms) and the length of the trace of the particle in the microtube on a captured image. Thus, the detection limit is limited by the capture time of the CCD camera, which enables the quantification of speeds from 200 up to 1800  $\text{mm s}^{-1}$ .

This integration foresees that new fabrication techniques towards Lab-on-Chip applications of optically active rolled-up microtubes for label-free sensing are possible. The discussion in the next chapter picks up the results from the diameter tuneability of the microtube, their fluidic capabilities and the integration progress and discusses possible applications of these microtubes for a variety of research fields.

## ***4.4 Field of application of SiO<sub>x</sub> microtubes – a perspective***

### ***4.4.1 Microtubes as artificial cavities for cells***

Collaborations are established to push forward the new approach of combining cell engineering with artificial tubular structures. Cells, especially the utilized HeLa (from **Henrietta Lacks**, cancer patient) cells have diameters above 10  $\mu\text{m}$ . The confinement of individual cells in rolled-up microtubes is achieved by adjusting the diameter of the microtube to the size of the cell. Particles are only driven by external forces such as the Brownian motion or other forces like convection of the medium where the particles are suspended in. Living cells are able to move by themselves. Therefore, by functionalizing the inner surface of the microtubes with specific proteins from the extracellular matrix (ECM) makes the microtubes attractive to for cells<sup>[10]</sup>. Another possibility to get cells into a microtube is either to force them by pumping with a negative pressure as Smith et. al [45] demonstrated or to move them in by using optical tweezers.

The collaboration for the cell investigation is mainly performed with Dr. Wang Xi, who is also co-authoring the publication Harazim et al. [10] of fabrication and applications of SiO<sub>x</sub> microtubes.

## 2D cell confinements

It is well known that submicron-level discrepancy on the substrate can cause abrupt changes in cellular behavior due to the high sensitivity of the cells to their micro-environment.<sup>[70-72]</sup> Cells react sensitively to cues in their local microenvironment including gradients of cytokines and secreted proteins from neighboring cells, the exposure to soluble signals and the texture of the substrates.<sup>[73-80]</sup> To date, most cellular activity studies are performed on conventional planar two-dimensional (2D) substrates,<sup>[81]</sup> even though cellular signaling and responses in tissues *in vivo* occur in a highly complex 3D system, named the extracellular matrix. This 3D environment confines cell shape and regulates cellular behaviors. It is thus expected that cells behave significantly different in 2D and 3D environments.<sup>[81,82]</sup> As a result, a 3D scaffold which can mimic the *in vivo* environment for cell culture is highly sought-after.<sup>[83,84]</sup>

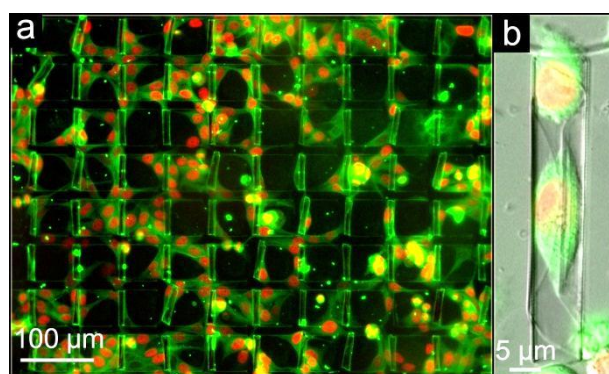


**Figure 4.8:** Biofunctionalized array of rolled-up microtubes. (a) Fluorescent image of HeLa Kyoto cells, stably expressing a fluorescently tagged core histone, H2B-mcherry (red), and mEGFP- $\alpha$ -tubulin (green), cultured on a SiO/SiO<sub>2</sub> microtube array. The microtubes are functionalized with fibronectin and then tagged with a primary mouse antibody against fibronectin, followed by fluorescent anti-mouse IgG-FITC secondary antibody staining. The green fluorescence of the tubes confirms the conjugation of fibronectin to the surface; the cells grow well both on the surface of the microarray and inside the tubes. (b) Merged optical and fluorescent images of two HeLa Kyoto cells inside a microtube (Taken from Ref. [10]).

During this project, the SiO/SiO<sub>2</sub> microtubes are chemically functionalized with fibronectin, an ECM glycoprotein that binds to membrane-spanning receptor proteins named integrins. Since cells usually have a size of above 10  $\mu$ m, a microtube diameter larger than 10  $\mu$ m is required for 3D cell culture studies. The platform's viability for *in vitro* cell culture has been tested using HeLa Kyoto cell lines. Fluorescent imaging of live samples shows that the HeLa cells proliferate on the platform during extended periods of time. The cells showed normal morphology (Figure 4.8.a) and survived and proliferated inside the tubes for similar periods as in 2D culture. Figure 4.8.b depicts a zoomed-in view on a single functionalized microtube confining two cells.

The tubular structure allows only one-dimensional free motion of the cells; thus one can expect important cellular processes such as cell migration or cell division and mitosis to be affected. Different from conventional microfluidic channels, where the walls are usually perpendicular to the substrate, the microtubes with their smooth curved surface inside could mimic the *in vivo* environment of a blood vessel, for instance. Furthermore, the production of large arrays of transparent and biocompatible microtubes allows researchers to speed up the investigation and scrutinize isolated cells one by one in a novel 3D platform for studies such as cell migration and proliferation.

#### 4.4.2 Catalytic microtubes as versatile tools

Just recently several publications demonstrated that with the rolled-up nanotech it is easily possible to create catalytic microtubes which are mainly based on materials such as Ti, Cr, Fe, Co, Ni and Ag.<sup>[9,48-55,85,86]</sup> The catalytic microtubes have in common that they have a catalytic layer on the inner tubular wall to decompose hydrogen peroxide into water and oxygen gas. Platinum is a common catalyst but also biological enzymes such as catalase are employed.<sup>[51]</sup> The development of catalytic microtubes reached a technological level where a remote control in microfluidic channels is already realized. The remote control is rather simple: the microtube has a ferromagnetic layer (Fe) incorporated which can be affected by an external magnetic field.<sup>[50]</sup> Hence, the microtube aligns itself with the magnetic field **B** and since the propulsion is unidirectional and continuous, the catalytic microtube can be guided through a microchannel network as depicted in Figure 4.9.1.(A-C). The entire microfluidic chip design with the microchannel system and the reservoir for the catalytic microtubes (microbots) is schematically depicted in Figure 4.9.1.D.

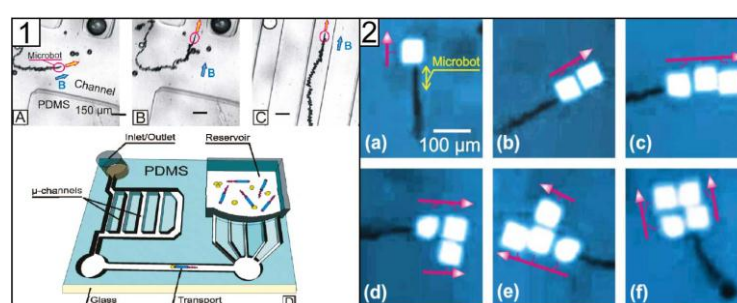


**Figure 4.9:** Catalytic microtubes in a microfluidic system. (1) (A-C). Optical sequence of a microbot “swimming” into the microchannels of a PDMS chip. The blue arrow represents the direction of the magnetic field. (D) Schematic of the fabricated microchip used for the transport of microparticles. (Taken from Ref. [48]) (2) Optical images of a microbot assembling four nanoplates in different configurations (a–f) Fuel solution used: hydrogen peroxide (5 wt %), 0.005% surfactant, and 1 vol % isopropanol. (Taken from Ref. [50])

These microbots are not only suitable to be guided through a complex channel network, but they can also be utilized as cargo-transporters, which has been demonstrated by Solovev et al. [50] recently. The sequence of optical images shown in Figure 4.9.2.(a-f) visualizes that one single microbot can be guided through a bulk solution to collect several microplates and transport them to a desired destination. Transporting nanoplates from one location to another seems not spectacular. However, thinking a step further that these microtubes could transport drugs without harming healthy cells through the blood vessel system directly to cancer cells, this tool gains a lot of attraction.

By shrinking the diameter of the catalytic metallic microtubes down to the sub-micrometer regime which is remarkably smaller than the diameter of a cell, a new functionality arises: a self-propelled nanotool.<sup>[87]</sup> Due to asymmetric rolling-up the tubular openings have a “sharp tip” like structure. This structure has two functionalities: (i) the asymmetric opening forces the nanotube into a corkscrew like motion (Figure 4.10.a) useful for drilling and (ii) the tip of the microtube is sharp enough to break bio-membranes and enter cells (e.g. HeLa cells) as depicted in the optical image of Figure 4.10.b and the SEM image in Figure 4.10.c. This is the consequent improvement of the previously described remotely controllable microbot. These two examples of multifunctional micro and nanotubes with an incorporated catalytic layer demonstrate the high potential of the rolled-up nanotech in biosciences.

Whereas the above described catalytic microtubes consist partially of toxic, expensive materials and sometimes consider extravagant deposition techniques such as molecular beam epitaxy (MBE), the simple addition of a thin (2 nm) layer of gold by e-beam evaporation transforms a SiO<sub>x</sub> microtube into a powerful tool with a high potential to beat the previously presented catalytic engines regarding the easiness of fabrication, their costs and biocompatibility.

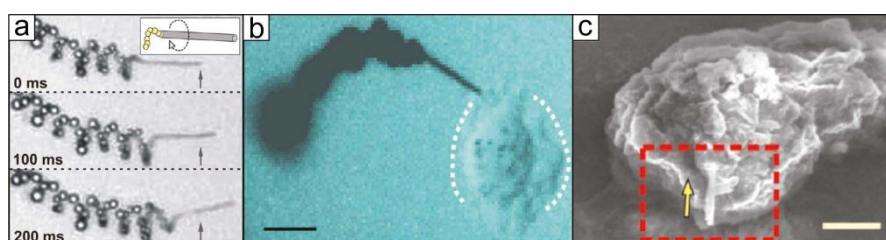


**Figure 4.10:** Self-propelled nanotool. (a) Autonomous corkscrew-like motion of a single InGaAs/GaAs/Cr/Pt (3/3/1/1 nm) rolled-up nanojet. Arrows indicate relative motion of the nanojet between panels, and the schematic inset shows the type of motion. (b) Optical microscopy image of an active nanotool drilling into a cross-linked biomaterial; a paraformaldehyde-fixed HeLa cell. Scale bar = 10  $\mu\text{m}$ . (c) Representative secondary electron SEM images of tubular nanotools which are autonomously embedded into a biomaterial (fixed HeLa cells). (Text and images taken from Ref. [87])

Here, the SiO/SiO<sub>2</sub> microtubes serve as a template for the modification with self-assembled monolayers (SAMs). Before rolling-up, the strained SiO/SiO<sub>2</sub> bi-layer membrane is supplemented with the coating of a 2 nm thin Au layer. Instead of a two layer system a three layer SiO/SiO<sub>2</sub>/Au system rolls-up into a microtube. Similar to the metal based catalytic micro-engines demonstrated by Sanchez et al. [51] catalase enzymes can now be coupled to the inside of the microtube creating a hybrid, semi-transparent and low-cost microjet.<sup>[51]</sup> Figure 4.11.a depicts the general principle of utilizing an organic catalyst to decompose H<sub>2</sub>O<sub>2</sub> into water and O<sub>2</sub> gas.

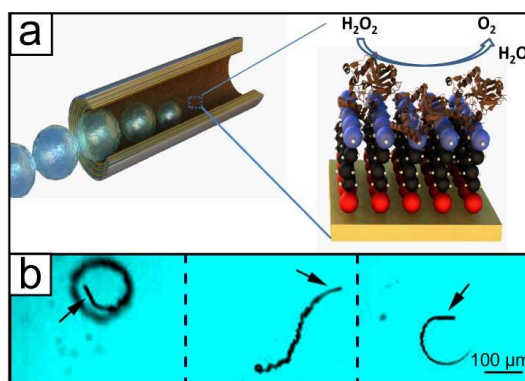


**Figure 4.11:** Microtubes with bio-functionalized surfaces. (a) Schematic example of a hybrid biocatalytic microengine. The inner tubular surface is functionalized with self-assembled monolayers (SAM) and the protein catalase as catalyst to reduce H<sub>2</sub>O<sub>2</sub> into water and O<sub>2</sub> gas. (Taken from Ref. [51]) (b) An optical sequence shows the trajectories of a SiO/SiO<sub>2</sub>/Au-catalase microjet engine in a 2.0% (v/v) H<sub>2</sub>O<sub>2</sub> solution. The arrows point on the 50 μm long microjet (Taken from Ref. [10]).

SiO<sub>x</sub> microtubes modified this way are the first catalytic microjets containing oxide layers which are suitable for investigations ranging from fundamental studies to biosensing applications. The inner and outer walls of the microjets can be selectively biofunctionalized just by adding a gold layer inside or outside. The oxide layer can be modified with different functionalities such as deoxyribonucleic acid (DNA) or antibodies to capture different targets or for sorting of biomolecules in a similar, yet inexpensive manner compared with reported microjets containing Au layers outside. <sup>[54,55]</sup>

The hybrid microjets of about 5 μm in diameter and 50 μm in length acquire speeds of about 150 μm/s when they are immersed in a fuel solution containing 2% H<sub>2</sub>O<sub>2</sub> and 0.05% sodium dodecyl sulfate (SDS) which reduces the surface tension. Figure 4.11.b depicts three different types of motion of catalytic SiO/SiO<sub>2</sub> microjets in a hydrogen peroxide solution. A video corresponding to the sequence shown in Figure 4.11.b is available in the supplementary information of Ref. [10].

With this new design of the microjets the material's toxicity is in principle reduced, the use of biocompatible fuel is imaginable and the utilized materials are cheap and easier to deposit, all this without compromising the form and functionality of the catalytic microtubes. Furthermore, with the ability of tuning the diameter of the rolled-up tubes it is possible to adjust the size of the catalytic microtubes to specific applications, such as drilling tools with thin microtubes or high throughput pumps with larger catalytic microtubes. All this shows that SiO<sub>x</sub> tubes have a high potential to be the leading type of catalytic rolled-up structures especially in research fields where non-harmful materials are required. The transparency of the microtubes enables studies on fundamental hydrodynamics and modeling in narrow cavities.

#### ***4.4.3 On-chip components: pumps, valves and sensors***

The integration of sensors and actuators into a single portable LoC system is crucial for reaching the aim of fabricating an analytic device based on the point-of-care concept.<sup>[88]</sup> In particular, actuators involve pumps and valves to move and control the fluids on-chip whereas sensors cover a large range of different sensing mechanisms. The next paragraphs give an insight on the potential of microtubes working as sensors and actuators in LoC devices.

##### **Driving fluids with microtubes**

Solovev et. al. [67] recently presented a novel approach for on-chip micropumps which is based on the catalytic reaction on the inner tubular wall. The huge advantage of this method is the pumping of liquids and even particles through the microtube without the use of any mechanical components as illustrated in the image sequence in Figure 4.12. Furthermore, the low amount of toxic fuel necessary to move fluids enable applications where biocompatible components are mandatory like the sensing of cells.<sup>[45]</sup> The ability of tuning the diameter of the SiO<sub>x</sub> microtubes to values from 1 to more than 12 μm provide access to pumping applications adjustable to many different sized objects for optimal pumping performance.

Another elegant way to pump liquids through micrometer sized channels is by the electro osmotic effect. Since this effect takes place on non-conductive surfaces (see Figure 2.5) the SiO<sub>x</sub> microtubes are predestinated to act as small cavities for EO effect based pumps.<sup>[10]</sup> Technically, it should be possible to fabricate one, two or even more microtubes in parallel to each other on a substrate between two electrodes in order to force the fluid in the microtubes to move along the electrical field.

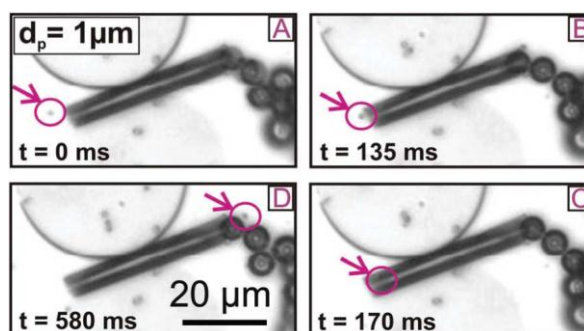


**Figure 4.12:** A catalytic micropump. Sequence of optical images of a tubular micropump which moves microparticles through its hollow body. Arrows show a tracked individual polystyrene microparticle with a diameter of 1  $\mu\text{m}$ . At the time  $t = 0$  ms (A), the particle comes into close proximity of the micropump mouth, at 135 ms approaches entrance (B), at  $t = 170$  ms is sucked inside (C) and after 580 ms is pumped out (D). Large black spheres exiting the micropump are oxygen microbubbles. (Text and image taken from Ref. [67]).

### Microtubes as valves

The schematic diagram of a micro-valve as depicted in Figure 4.13 point out the potential of rolled-up microtubes working as important parts of actuators in LoC devices. The theoretical work from Daghighi et al. [89] on a powerful and new kind of valve employs cylindrical channels as in- and outlets to the valve chamber (Figure 4.13.a).

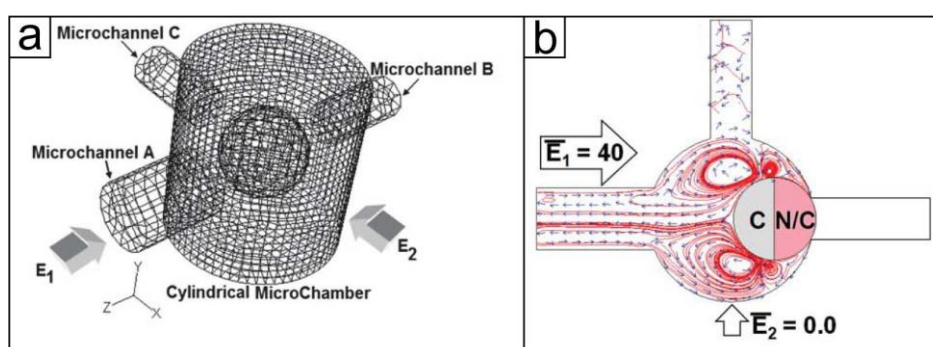


**Figure 4.13:** Principle of a microvalve. (a) Schematic diagram of a micro-valve with three microchannels and one suspended Janus particle in it.  $E_1$  and  $E_2$  represent external electric field directions. (b) Theoretical model and cross section of the valve containing: stream lines (red), arrows indicating the flow direction (small and black) and a Janus particle with conducting “C” and non-conducting “N/C” material. Vectors  $E_1$  and  $E_2$  indicate the direction and the strength of the applied electrical field. (Text and images taken from Ref. [89])

The valve chamber has three inlets (outlets, depending on the flow direction) of cylindrical shape. The valve chamber contains a spherical Janus particle with a conductive and a non-conductive face, whereas the diameter of this particle is at least as large as the diameter of the channels connected to the chamber. The Janus particle can be moved by applied external electric fields to each of the three channels just by tuning the strength and direction of the applied electric field ( $E_1$  and  $E_2$  in Figure 4.13.a-b). Hence, it could be possible to close one of the channels with the Janus

particle as the simulation in Figure 4.13.b indicates.  $E_1$  is strong enough to push the Janus particle to the right side and close the channel. If  $E_2$  instead of  $E_1$  would be present, the upper channel could be closed by the Janus particle.

Opening and closing of channels utilizing a spherical Janus particle requires a cylindrical shape of the channel. Using the rolled-up nanotech is a suitable way to solve the technical realization of fabricating cylindrical channels since it is very difficult to fabricate microchannels with a circular cross-section<sup>[90]</sup> with standard microchip fabrication techniques.

### Microtubes as optical sensors

One of the most important applications of microtubes, on which this thesis focuses on, is the application of optical active microtubes as on-chip sensors to analyze fluids. In recent years some promising approaches in the fabrication of such microtubes have been developed,<sup>[12,13,25]</sup> but the optical quality could not compete with similar optical sensors<sup>[23,26,29]</sup> and the microfluidic integration is not carried out yet.

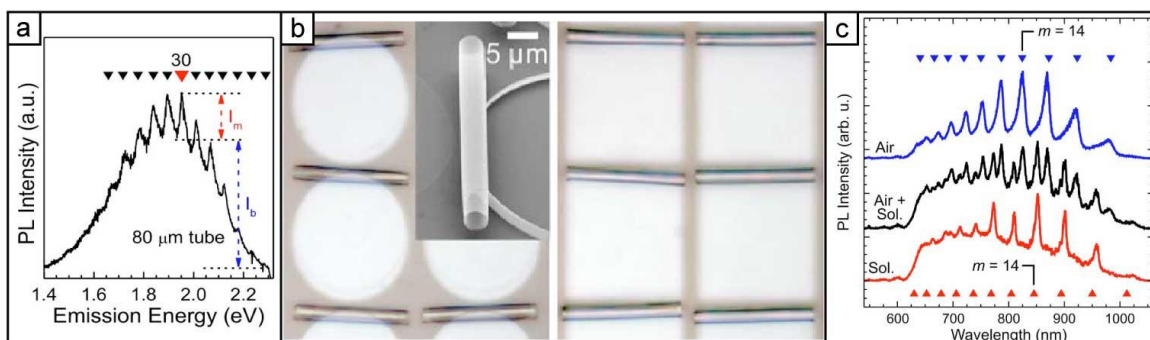


**Figure 4.14:** SiO<sub>x</sub> microtubes as optical sensors. (a) PL spectrum from the middle of a microtube rolled up from a circular nanomembrane. Intensities of the mode ( $M=30$ ) and the broad emission band are defined as  $I_m$  and  $I_b$ , respectively. The triangles indicate the mode positions obtained from a finite-difference time-domain simulation. (b) Optical microscope image of ordered microtube arrays from nanomembranes of different shapes: circles (left panel) and squares (right panel). The inset shows an SEM image of a microtube from a circular nanomembrane. ((a and b) text and image adapted from Ref. [12]). (c) Spectrum shift produced by the presence of an aqueous sugar solution inside the tube. The spectra with the resonant modes in presence of the solution (red) or of a bubble of air trapped in the tube (blue). The black spectrum refers to a region at the interface between liquid and air inside the tube. (Text and image adapted from Ref. [25])

The PL spectra and microtubes in Figure 4.14.a-c show the state of the art rolled-up microtubes suitable for optical detection prior to this thesis. The diameter of a SiO/SiO<sub>2</sub> with optical properties is still quite large (80 μm, Figure 4.14.a) but shows already optical resonant modes. One of the mode numbers is marked with a red triangle ( $m = 30$ ). The optical images (and the SEM inset) in Figure 4.14.b prove that the microtube can roll-up on different patterned sacrificial

layers. A detailed investigation on the tuning of the diameter is missing so far, but performed during this thesis. The PL spectrum in Figure 4.14.c proves that optical active rolled-up microtubes in principle can be utilized as refractometric sensors by monitoring the mode shift. Here for example mode number 14 is observed to be at different wavelength when the content of the microtube has a different refractive index. In this particular case the content could not be exchanged on demand and the quality factor of the microtube is also not good enough to be suitable for high resolution refractometric measurements.

## 4.5 Conclusion

In this chapter it has been demonstrated that conventional lithography combined with electron beam evaporation is a productive and an easy way to fabricate rolled-up SiO/SiO<sub>2</sub> microtubes well aligned and in a large quantity on a substrate. The diameter of the microtubes can be tuned over an order of magnitude from 1 to 12 μm simply by modifying the composition of the bi-layer thickness ratios. It has been confirmed that these microtubes can easily be filled with liquids of different contents such as fluorescence dye or microparticles. It has been demonstrated that this kind of microtubes enable a wide range of applications with key features of which can be accessed by the diameter. SiO<sub>x</sub> microtubes above 10 μm in diameter are suitable for single cell studies in narrow 3D scaffolds mimicking the *in vivo* environment of cells. A small microtube combined with a microfluidic channel system could be suitable as minimal invasive injection needles to deliver drugs into cells similar to the work just recently described by Boukany et al. [91]. Microjet engines based on cheap and biocompatible materials have been proved for their functionality with the result that they provide a high potential to replace the conventional metallic based micro jet engines in research fields where non-harmful materials are required. Microtubes with about 5 μm and smaller in diameter have some possible applications: they could be utilized as fluid micropumps in Lab-on-Chip devices by employing the electro-osmotic flow when also electrodes are incorporated into the structure and they could act as a part of a new innovative valve where the theoretical calculation is just recently presented by Daghighi et al. [89]. Furthermore, the demonstration of their integration into microfluidic channel systems as bridges between microfluidic channels could open up many possibilities for further research on optical label-free sensors in Lab-on-a-Chip devices.<sup>[13]</sup> All these applications confirm the high potential of SiO<sub>x</sub> based rolled-up microtubes in chemical/ biochemical analysis and as components in Lab-on-a-Chip devices.

From all these possible applications one specific has been selected for a deeper investigation. The concern is to push forward the concept of a Lab-in-a-Tube<sup>[45]</sup> to a new level of integration towards Lab-on-Chip devices with several integrated optofluidic sensors. The development and characterization of such a powerful system is presented in the next chapter.



## ***5 SiO<sub>2</sub> microtubes as optofluidic sensors integrated on-chip***

This chapter is based on the publication Harazim et al. [92] in the Journal Lab on a Chip. Expressions and segments taken from this publication are not cited separately.

This part of the thesis introduces a new methodology of fabrication of tubular rolled-up optofluidic ring resonators (RU-OFRRs) based on glass (SiO<sub>2</sub>) material with high optical quality factors. Combining lab-on-a-chip fabrication methods and rolled-up nanotech allows the fabrication of fully integrated tubular optofluidic sensors. The microfluidic integration of several RU-OFRRs on one chip is solved by enclosing the microtubes with a patterned and robust SU-8 polymeric matrix. A viewport on each microtube enables exact excitation and monitoring of whispering gallery modes with a photoluminescence spectroscopy system under constant ambient conditions while exchanging the content of the RU-OFRR with liquids of different refractive indices. The refractometric sensor capabilities are investigated regarding signal stability, sensitivity and reliability. The sensitivity of the integrated RU-OFRR, which is the response of the modes to the change of the refractive index of the liquid, is up to 880 nm/refractive index units (RIU).

### ***5.1 Introduction***

Label-free optofluidic sensor technology is a topic of great interest ranging from analytical science to pharmaceutical industry with a variety of applications implemented as Lab-on-a-Chip (LoC) devices.<sup>[25-27,93-95]</sup> As already mentioned in background chapter 2.2, part of optofluidics merges microfluidics with optical sensing capabilities into a single device. Refractive index based sensors are realized by different approaches such as interferometer,<sup>[96,97]</sup> surface plasmon resonance<sup>[96,98,99]</sup> optical waveguides,<sup>[100-102]</sup> photonic crystals,<sup>[103,104]</sup> optical fibers<sup>[105,106]</sup> and ring resonators. Optical ring resonators come in different shapes such as planar ring resonators,<sup>[107]</sup> spheres<sup>[108]</sup> and disks,<sup>[109]</sup> and if combined with fluidics they are called optofluidic ring resonator (OFRR). Only in tubular geometry they do inherently combine compact and most practical fluidic functionality with optical sensitivity. According to the resonant conditions, circulating light can interfere constructively at certain frequencies called whispering gallery modes (WGM) whose evanescent field decays exponentially outside the tubular wall. The sensing mechanism of tubular OFRRs is the response of the evanescent field to changes in the RI near the surface of the tubular wall. The quality-factor (Q) of such ring resonators, related to the linewidth of WGMs in the detected light spectrum, is an indicator of the quality of the fabricated optical device. High quality factors are preferable in order to work efficiently as label-free bio-sensors for cells,<sup>[45]</sup> bio-analytes<sup>[13,25,46]</sup> and vapours.<sup>[27,110]</sup>

Liquid core optical ring resonators (LCORRs) are part of the OFRR family and often rely on the fabrication of narrow circular channels by glass capillary pulling.<sup>[111,112]</sup> Although this kind of OFRR provides very high quality factors (e.g.  $10^6$ ), it is not suited for parallel microfluidic on-chip integration due to its fabrication technique, big dimension and fragility. Other members of the OFRR family are liquid-core microtube optical ring resonators (LCMORs)<sup>[25]</sup> and rolled-up micro cavity ring resonators (RU- $\mu$ CRRs)<sup>[13]</sup> which are based on rolled-up nanotechnology,<sup>[1,13,25,113]</sup> but which up to now showed relatively low Q values only in the range of several hundreds.<sup>[13,25,45]</sup> However, by this technology, large arrays of tubular fluidic channels with well-defined shape and size can be fabricated on virtually any kind of substrate.<sup>[1,10,11,13,45]</sup> Due to their easy size tuneability<sup>[11]</sup> both in length and diameter they perfectly match to the typical dimensions of microfluidic channels and thus are good candidates to be included in compact LoC systems. First steps towards integration of rolled-up microtubes into microfluidic systems have been reported previously,<sup>[10,66,114]</sup> but their optofluidic functionality after microfluidic integration remains unexplored.

In this part of the thesis the fabrication and characterization of high Q rolled-up optofluidic ring resonators fully integrated into Lab-on-a-Chip devices is presented. The ring resonators are fabricated on a mother substrate and consist of rolled-up glass (SiO<sub>2</sub>) microtubes with diameters close to 10  $\mu$ m. Selected microtubes can be picked up from the mother substrate and transferred to a target microchip for further assembly. Optical characterization by photoluminescence (PL) spectroscopy reveals high Q values of up to 2900. A technology platform is described ranging from the fabrication of RU-OFRRs over the integration process to the final device. The stability of the response signal and the reproducibility are evaluated by flowing different analytes through the devices for defined periods of time. A minimum detection limit of  $3.4 \cdot 10^{-4}$  per refractive index unit (RIU) is obtained and a maximum sensitivity of 880 nm/RIU, which is the highest value measured for any RU-OFRR to date.

## 5.2 *Microchip fabrication*

This chapter presents in detail the fabrication process of the chip device. Specific fabrication parameters can be found in chapter 3.3.2. (*On-Chip integration of SiO<sub>2</sub> microtubes*). The flow chart in Figure 5.1 depict the six main steps of the fabrication process which are in particular: (1) selection of the substrate's material and preparation; (2) the fabrication of microtube with a high optical quality; (3) transfer of the microtubes to the prepared substrate; (4) further preparation of the microtubes for the last two integration steps; (5) the integration of the microtubes into a microfluidic channel system and (6) the final assembly of the microchip device.

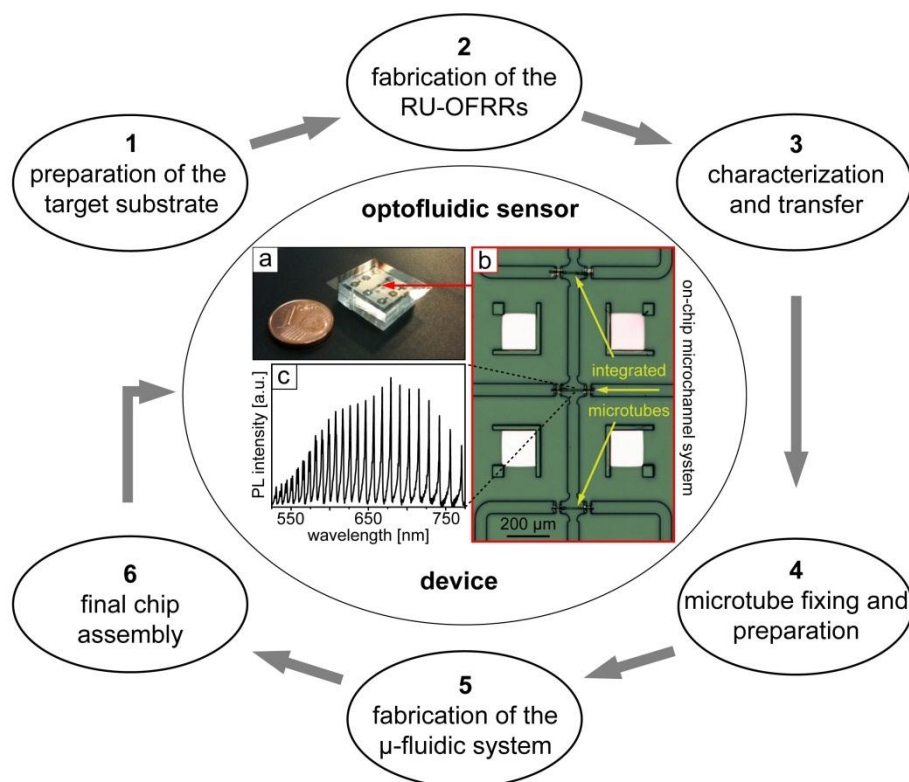


**Figure 5.1:** Fabrication flow chart for the integration of high quality rolled-up optofluidic resonators. (a) Photograph of a fabricated optofluidic sensing chip device. (b) Optical microscope image of three microtubes integrated into a microchannel system. (c) Background subtracted PL spectrum measured on a microtube integrated into the optofluidic chip sensor.

The final chip device pictured in Figure 5.1.a consists of a microfluidic channel system (Figure 5.1.b) where the in- and outlets are bridged by integrated rolled-up microtubes. The optical quality of the RU-OFRs is evaluated by PL spectroscopy in a wavelength range from visible to near infrared (Figure 5.1.c).

The manufacturing of this complex device involves different material deposition methods and clean room processing steps. Each of the fabrication steps will be described in detail below, starting with the selection of the material of the substrate.

### Step 1.1: material of the substrate

The D263T 4 inch glass wafers are cut into pieces to match with the dimension of a stage for standard glass slides in an ordinary invers microscope. The thickness of the glass is 500  $\mu\text{m}$ , this value of the thickness is a compromise between the fragility of the glass (a larger value increases the stability) and maintaining the option of using short distance objectives such as immersion oil lenses requiring thin as possible substrates. Besides the high transparency of more than 90 % of the glass in the wavelength range of 400 to 800 nm, an important property of the glass is its thermal expansion coefficient  $\sigma$ . The utilized materials have different inherent expansion

coefficients and due to the layered stack design of the final device some of the materials will have a large contact area among them. In particular, the interface between the glass substrate and an Al<sub>2</sub>O<sub>3</sub> layer as well as the interface between the Al<sub>2</sub>O<sub>3</sub> layer and the SU-8 channel structure, both are applied during a later fabrication step. Hence, the thermal expansion coefficients should be comparable in their values in order to avoid strong strain gradients caused by thermal treatment of the substrate. In particular, the expansion coefficient of the glass substrate is  $7.2 \cdot 10^{-6} \text{ K}^{-1}$  [115], which is already close to the value of Al<sub>2</sub>O<sub>3</sub> of about  $7 \cdot 10^{-6} \text{ K}^{-1}$  [116]. Furthermore, the  $\sigma$  of both materials should be as close as possible to the expansion coefficient of SU-8 ( $52 \cdot 10^{-6} \text{ K}^{-1}$ ) [117] employed later in the chip fabrication process. Minimizing the difference of the expansion coefficients of Al<sub>2</sub>O<sub>3</sub>, glass substrate and SU-8 reduces the number of possible system failures such as detachment due to interlayer stress. The choice to harmonize the expansion coefficients between D263T glass and the Al<sub>2</sub>O<sub>3</sub> layer is justified by the inherent Young modulus of the utilized materials and their chronological order of application in the system. A lower value indicates a more flexible material. The Young modulus of PDMS (360 to 870 kPa) [118] (also utilized later) is very low and can be neglect compared to the materials SU-8 (2 GPa) [117], D263T (72.9 GPa) [115] and Al<sub>2</sub>O<sub>3</sub> (69 GPa) [119]. The Young modulus of SU-8 is low enough that it can compensate forces at the contact area originating from different thermal expansion coefficients in the temperature range of 20 to 180 °C. This and the fact that Al<sub>2</sub>O<sub>3</sub> is mainly between the D263T glass and the SU-8, it is appropriate to equalize the expansion coefficients between the substrate and the Al<sub>2</sub>O<sub>3</sub> layer. After assembly, the stress in the system occurs mainly between the flexible SU-8 and the Al<sub>2</sub>O<sub>3</sub> layer.

### Step 1.2: alignment structures

The alignment structures simplify the handling and increase dramatically the accuracy of alignment. These four components are depicted in Figure 5.2 and can be also seen as four white squares in the microscope image in Figure 5.1.b. The macroscopic marks 1, 2 and 3 in Figure 5.2 (highlighted in orange) support the manual alignment and mark 4 (highlighted in blue) supports the precise alignment with a mask aligner during the photolithography processes.

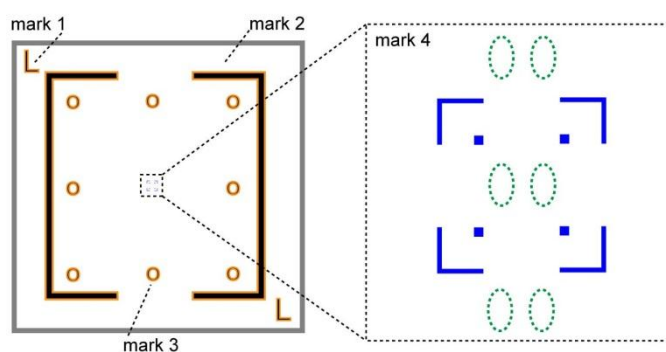


**Figure 5.2:** Sketch of the alignment structures. (a) Total overview on the alignment structure. Markers for manual macroscopic alignment are highlighted in orange; markers for precise alignment are highlighted in blue. (b) Close view to the central part. The green highlighted dashed ovals indicate the position of the sockets introduced in the next fabrication step.

The chiral character of mark 1 assists the positioning of the substrate during orientation sensitive processing steps. Mark 2 and 3 support the alignment of the PDMS lid in a next fabrication step and mark 4 is used during all alignment steps where the mask aligners MA 56 and MA 6 are employed. The next part of the substrate preparation involves the introduction and fabrication of the so-called socket system.

### Step 1.3: fabrication of the socket system

As already discussed in chapter 4 (*Scaling of SiO<sub>x</sub> microtubes and potential applications*), arrays of rolled-up microtubes can be integrated into a microfluidic structure by photolithography processing. Unfortunately, it is very difficult to manufacture another set of microtubes with similar or different functionality on the same substrate without harming the fabricated microtubes. Different kind of microtubes are for example optical microcavities for enhanced liquid sensing,<sup>[13]</sup> flexible split-wall microtube resonators for mouse cell analysis<sup>[45]</sup> and rolled-up magnetic sensors for in-flow detection of magnetic particles<sup>[56]</sup>. The invented socket system eliminates these difficulties and raises the possibility of combining many different microtubes with different functionalities on one substrate. In case of utilizing optical active microtubes, the sockets allow the precise positioning and elevation of selected microtubes on a target substrate for further integration.

The requirements on the sockets are as following: (i) the microtubes can be elevated above the substrate to a fixed and reproducible distance; (ii) the dimension of the sockets is adaptable to the dimension of the microtubes; (iii) microtubes can be placed in any orientation and at any location on the substrate utilizing the sockets; (iv) suitable for mass production and (v) long term stability. With an appropriate design, all these requirements can be fulfilled by the negative photoresist SU-8. This epoxy based photoresist has excellent chemical and temperature resistance, a large range

of layer thicknesses from 1 up to 200  $\mu\text{m}$ , a high aspect ratio and is already widely utilized in micro electromechanical systems (MEMS).<sup>[33-35,120]</sup> The sketches depicted in Figure 5.3 show the design of a socket. One socket (Figure 5.3.a) consists of (1) the clamp, which will fix the microtube into the predefined lateral position and (2) the supporting platform to elevate the microtube above substrate. The width  $b$  as well as the heights  $h_1$  and  $h_2$  can be adapted to the size of the microtube. The heights are tunable by the spin-coating parameters and the viscosity of the utilized resist, because the structuring of the SU-8 resist relies on photolithographic processing. The position and orientation of the socket as well as the width  $b$  can be adjusted to the required parameters simply by another photomask with suitable structures. The planar elevation of one microtube can be achieved by two aligned sockets with a distance  $d$  to each other. A typical arrangement is given in Figure 5.3.b showing a microtube with a free-standing part in the middle. The distance  $d$  between two sockets utilized in this thesis is set to 140  $\mu\text{m}$ , appropriate to the length of 200  $\mu\text{m}$  of the microtubes. As indicated in Figure 5.3.b the height  $h_1$  should be at least as high as the microtube providing a planar surface after spin coating photoresists on the substrate (required later during the chip fabrication).

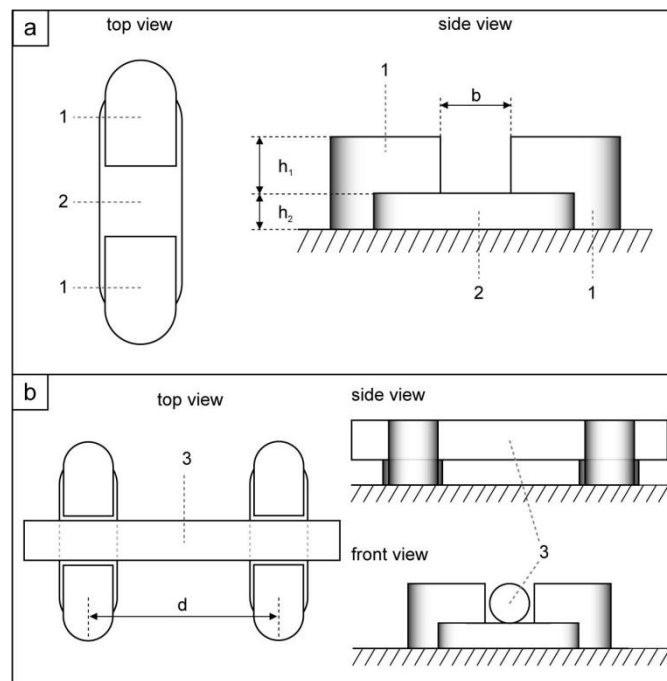


**Figure 5.3** Sketch of a socket structure. (a) One socket structure consist of two components: (1) The clamp to fix the microtube into the requested position and (2) the supporting platform to elevate the microtube from the substrate. The distance  $b$  and the heights  $h_1$  and  $h_2$  are tunable to match the size of the microtube. (b) Example arrangement of two sockets with a distance  $d$  to each other as supporting structures to elevate the microtube permanently to a fixed distance to the substrate.

The designed shape of a socket take in account recommendations for contact-area stress reduction<sup>[36,37]</sup> of the processed photoresist because a socket consists of two layers of SU-8. In

particular, structures with a small surface contact-area and round shapes are designed showing less interlayer stress and a longer lifetime. The process parameters for the baking times and temperatures as well as the final thermal cross-linking step are selected carefully in order to increase the interlayer bonding strength between the two resist layers and the stiffness of the SU-8 photoresist.

With an appropriate design of the photomask a large number of sockets can be fabricated on a single substrate. In this thesis the final device will contain three pairs of sockets, located between the central alignment structures as depicted in Figure 5.2 (socket position is highlighted by green ovals). A close view on one pair of sockets is shown in the optical image in Figure 5.4. The dashed line indicates the trenches in the sockets where the transferred microtube will be placed.

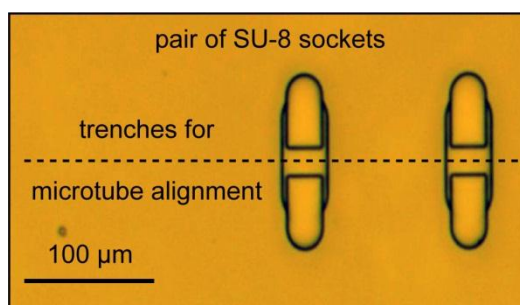


**Figure 5.4:** Optical image of a pair of sockets consisting of the SU-8 photoresist. Both sockets are aligned in parallel to allow the placing of a tubular structure along the trenches indicated by the dashed line.

The number of three pairs of sockets, respectively three microtubes on the chip device, is reasoned by the compromise between an appropriate chip fabrication time and the task of integrating multiple sensors. The principle of elevating and positioning a microtube on a target substrate is part of a submitted patent (January 2012).

## Step 2: microtube fabrication

The integrated glass microtubes act as microfluidic channels and as optofluidic components, constituting the sensor of the chip. Compared to the square shape pattern for rolling-up microtubes as described in chapter 3.2.3, the shape of the roll-up pattern is now more complex in order to establish an optimal light confinement along the tubular axis. One mother substrate contains about 400 optical active microtubes. In order to allow optical PL measurements on each microtube a certain distance of the optical active part of the microtube to the substrate is required to avoid light leakage to the substrate.<sup>[12]</sup> This requirement is fulfilled by a U-shape roll-up pattern producing a free-standing microtube with an elevated center part of the microtube.

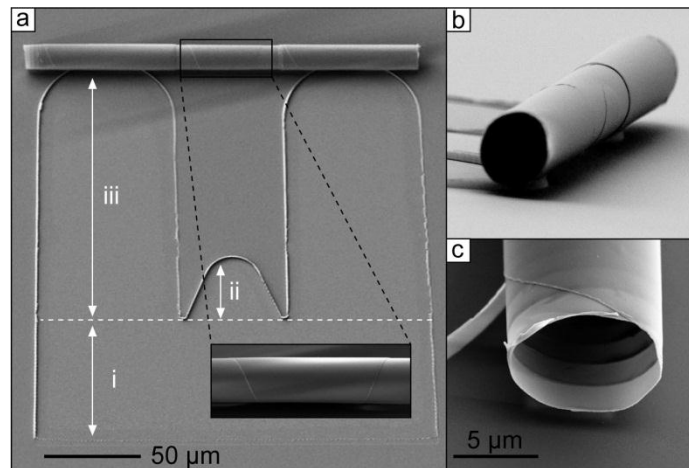


**Figure 5.5:** SEM images and zooms of a free-standing microtube. (a) Scanning electron image (SEM) image shows a U-shape pattern and a RU-OFRR. The pattern is separated into three segments (i to iii) by the white dashed line. The inset shows a magnification of the center of the free-standing part of the microtube with an outer diameter of 13  $\mu\text{m}$ . (b) Side view SEM image of a free-standing elevated rolled-up microtube. (c) Close-up of a microtube end where the compact rolling is clearly seen.

The basic fabrication method for this advanced microtube is similar to the previously described technique for rolling-up microtubes,<sup>[10,11]</sup> but instead of a SiO/SiO<sub>2</sub> bi-layer combination a single-material bi-layer of SiO<sub>2</sub>/SiO<sub>2</sub> is employed to roll-up the microtubes. With this material combination of the bilayer higher quality factors in the PL resonance spectrum could be achieved. The new U-shape pattern for rolling-up is depicted in Figure 5.5.a. The shape is adapted from microtube resonators described by Kipp<sup>[121]</sup> and Strehlow<sup>[122]</sup>. The U-shape pattern is separated in three segments by a white dashed line: (i) the first segment defines the tubular body and has a length of 75  $\mu\text{m}$  and a width of 200  $\mu\text{m}$ , segment number two (ii) is a spatially shaped on the outer wall of the microtube flanked by two segments of type three (iii) with a length of 160  $\mu\text{m}$ . The lobe in segment two induce a better light confinement within the tubular wall by turning it into a so called bottle resonator.<sup>[122]</sup> Segment three contributes to the mechanical integrity at the ends of the microtube due to a higher number of revolutions, and consequently a thicker wall. The rolling starts at the lower end of segment one and finishes in the upper position of the segments three. A rolled-up microtube in the final position and an inset with a zoomed-in view to the center of the microtube can be seen in the SEM images in Figure 5.5.a.

The central part of the microtube remains free-standing as it can be seen in Figure 5.5.b. The distance of the microtube to the substrate has a value of about 2.5  $\mu\text{m}$ . The total distance from the substrate to the microtube is calculated by the thickness of the sacrificial layer and the bilayer thickness contributed to the wall from segment number three. The first three windings and the compact rolling-up of the SiO<sub>2</sub> bilayer can be clearly seen in Figure 5.5.c depicting one end of a microtube.

The mother substrate, on which the microtubes are fabricated, is a square silicon wafer with lateral lengths of 10 mm (Figure 5.6.a). The U-shape roll-up pattern is arranged in a way that about 400 microtubes can fit on the Si substrate. During the deposition of the SiO<sub>2</sub> bi-layer, the sample is always mounted centered and in the same orientation on the substrate holder in order to maintain similar deposition conditions for every sample.

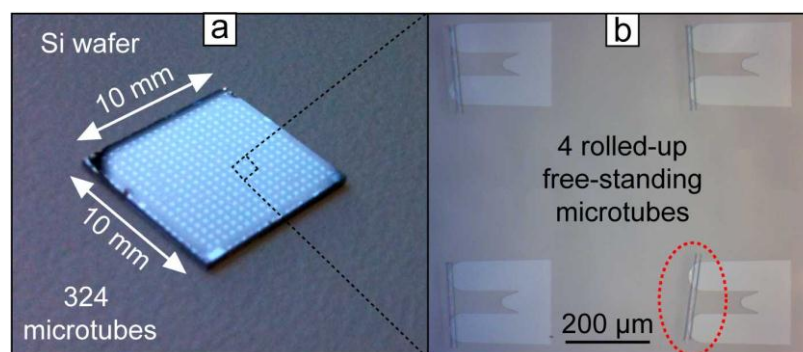


**Figure 5.6:** Fabrication of free-standing microtubes. (a) Photo of a silicon substrate which contains about 400 rolled-up free-standing microtubes. (b) Optical microscope image of four rolled-up free-standing microtubes. One remarkable misaligned microtube is highlighted by a red dashed circle.

A non-uniform coated sacrificial layer as well as differences in the bi-layer properties can lead to a slightly different rolling behavior as depicted in Figure 5.6.b. One of the four microtubes (highlighted by a red dashed circle) appears misaligned. This misalignment might not affect the mechanical properties of the tube regarding their usage as microfluidic channels, but differences in the optical properties can occur. Thus, all microtubes have to be analyzed for their optical properties by photoluminescence spectroscopy.

### Step 3.1: optical characterizations of microtubes

The PL spectrum of each microtube is recorded and the results are summarized in a PL-characteristic map of the substrate as depicted in Figure 5.7. The measurements on the sample were performed by Jens Trommer during his diploma thesis at the IIN. Each position on the map corresponds to a specific microtube, whereas the colors indicate the rolling status of the microtube. In particular: green means that the microtube rolled until the end of the U-pattern (28 %); blue marked fields indicate that the microtube is still free-standing but did not roll until the end of the structure (13 %); orange colored fields indicate that the microtube start to roll, but is not free-standing (48 %); the microtube in the last two cases cannot be used for integration because they are either damaged (black, 7 %) or not rolling at all (red, 3 %).

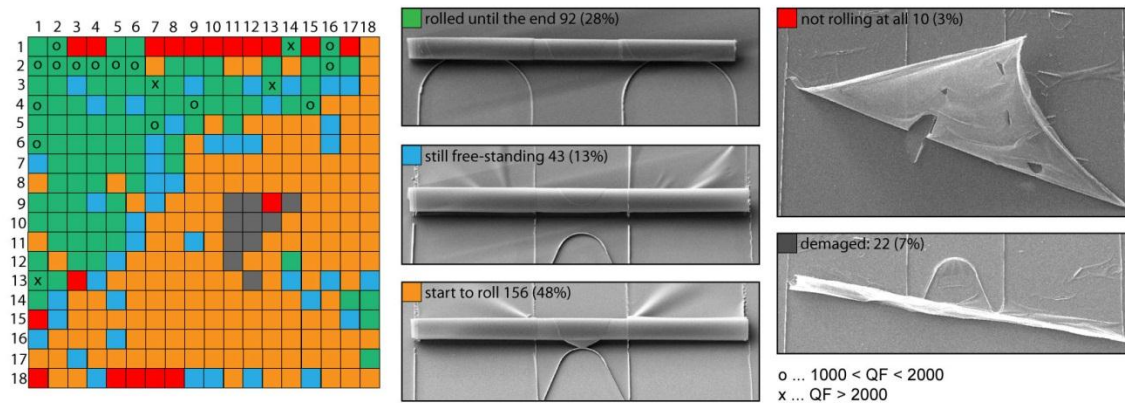


**Figure 5.7:** PL-characteristic map of a Si substrate with free-standing rolled-up microtubes. The map colors consider the rolling status of the microtubes: red: not rolling at all; grey: damaged; orange: start to roll-up; blue: the microtube is free-standing; green: the microtube rolled till the end. Fields marked with an x-symbol contain microtubes with a Q of more than 2000; fields marked with an o-symbol contain microtubes with a Q between 1000 and 2000. The SEM images on the right show an example of different roll-up states.

The quality factors of the resonance frequencies in the PL spectrum are calculated by using the full width at half maximum (FWHM) method. Certain microtubes show Q values between 1000 and 2000 which are marked with an “o” and some microtubes have Q values above 2000 which are marked with an “x” symbol.

Figure 5.8 shows a background subtracted PL data acquired from the center position of a RU-OFRR with Q above 2000. The spectrum reveals eight groups of modes, each of them corresponding to an azimuthal resonant condition.<sup>[122]</sup> The series of closely spaced modes at the short wavelength side of each azimuthal mode are higher order axial modes (see inset of Figure 5.8) and originate from the axial confinement<sup>[122]</sup> in the middle of the microtube.

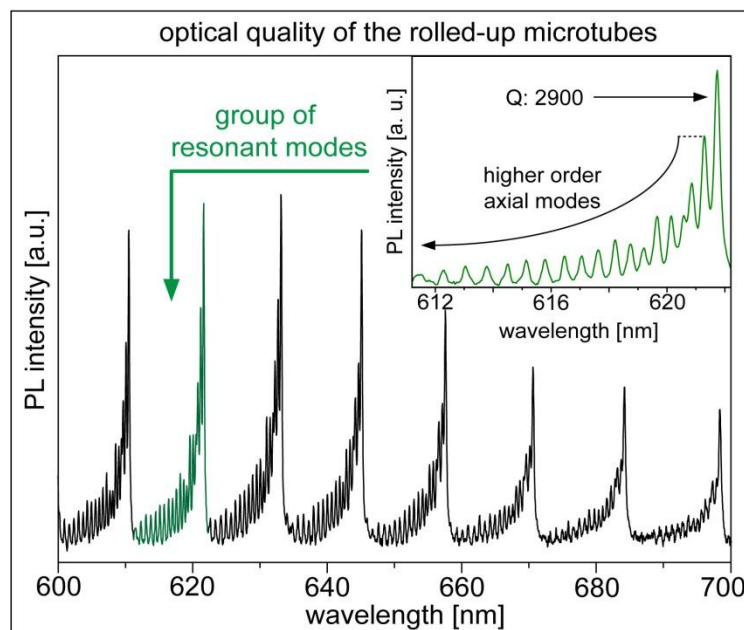


**Figure 5.8:** Optical characterization of a rolled-up microtube by photoluminescence spectroscopy. PL spectrum at the center part of a free-standing microtube. Inset illustrates one resonant azimuthal mode with an associated series of axial modes.

The mode with highest intensity for each group of modes reaches an average Q value of 2900. This value is derived from the peak linewidth after fitting the modes with Lorentzian curves, and represents the highest value reported for RU-OFRRs to date.

### Step 3.2: Transfer of the microtubes

The integration of optically active microtubes working as sensors requires a transfer to a socket structure prepared on the glass substrate in step 1, which can elevate the microtube to a certain height. Briefly, the transfer is carried out with a micro needle mounted on a 3D micro manipulator stage and a conventional microscope. The micro needle is a glass capillary pulled under heat until the tapered part reached a diameter of about 5  $\mu\text{m}$ . The transfer is performed by Vladimir Bolaños (member of the IIN, IFW Dresden). The 3D sketch in Figure 5.9 depicts how microtubes are placed onto the sockets. The trenches in the sockets help to wipe off the microtube from the micro needle and align it easily. With this method three microtubes are transferred to the prepared target glass substrate.

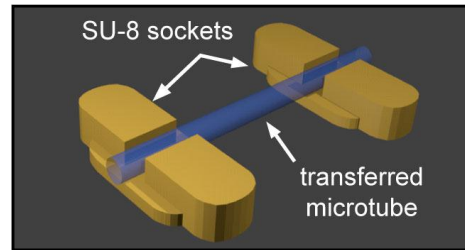


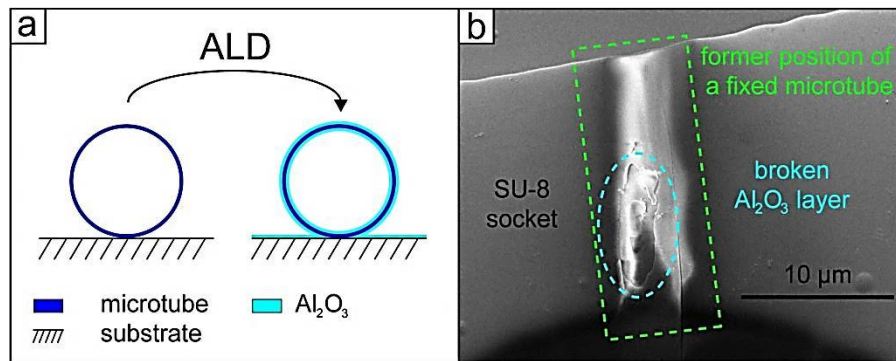
**Figure 5.9:** Sketch of a transferred microtube. The microtube is placed along the trenches of two SU-8 sockets.

As mentioned in the materials and methods section the transfer involves mechanical forces to the microtubes. It is known from Smith et. al. [45] that rolled-up microtubes can contain nano sized gaps between the rolled-up layers. Therefore, it is to consider that mechanical forces applied to the microtubes can change the configuration and size of these gaps by rearranging the bilayer windings if the interlayer friction is overcome by the mechanical forces. This rearrangement could lead to changes in the optical properties of the microtubes. Therefore, a PL measurement is performed on the transferred microtubes to track the evolution of the optical properties during the microchip assembly process. A summarized overview on the Q evolution can be found in chapter 5.4 on page 67.

After transfer, the microtubes simply lay on the sockets and the physical adhesion is too weak to hold the microtubes on the surface. In the next step of the chip fabrication the microtubes will be pinned to the substrate and stabilized mechanically in order to maintain their structural integrity and position on the substrate during the integration.

#### **Step 4.1: mechanical stabilization and fixing of the microtubes**

The structural integrity of SiO<sub>2</sub> microtubes is too fragile to stand against forces arising from surface tension during drying-out of liquids, which leads ultimately to a collapse of the microtube. After the transfer some steps involve the handling with liquids, which are mainly solvents and developer solutions during photolithography processing. Therefore, a stabilization step of coating a 10 nm thick Al<sub>2</sub>O<sub>3</sub> layer by ALD on the inner and outer microtube wall is required. This value is optimized in order to achieve appropriate mechanical stabilization with a thin as possible layer thickness in order to avoid a strong impact on the optical properties. Additionally, the isotropic coating of material helps to pin the microtubes to the sockets on the sample.<sup>[11,123]</sup>



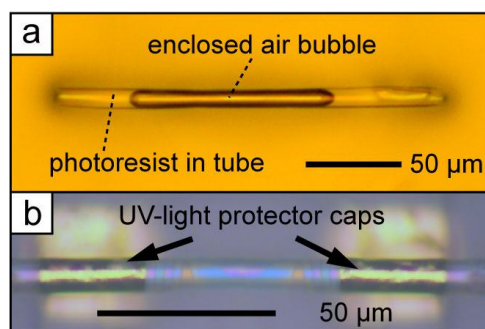
**Figure 5.10:** Principle of fixation and stabilization of microtubes by ALD. (a) An isotropic coating of  $\text{Al}_2\text{O}_3$  (bright blue) will fix the microtube to the substrate and stabilize mechanically. (b) SEM image depicts a broken  $\text{Al}_2\text{O}_3$  layer (marked by a blue dashed oval) deposited by ALD. The green dashed frame highlights the former position of a fixed microtube.

Figure 5.10.a illustrates the mechanism of the fixation and stabilization by isotropic coating. The rolled-up microtube is coated both inside and outside with an  $\text{Al}_2\text{O}_3$  layer (bright blue) fixing it to the substrate. The SEM image in Figure 5.10.b depicts an area on a SU-8 structure after an already fixed microtube (former position highlighted by the green frame) is removed by mechanical forces. The now visible broken  $\text{Al}_2\text{O}_3$  layer (bright blue dashed oval) marks the area where the microtube is in contact and pinned to the SU-8. Besides the mechanical capabilities of the ALD coating it offers another positive effect which could be interesting for other applications: the electrical isolation. This can be useful if electrodes in combination with the microtubes are designed to work as actuators such as electroosmotic pumps or valves (see chapter 4.4.3) where only the electrical potential is required.

#### Step 4.2: deposition of UV-light protectors

Thurmer et. al. [66] demonstrated that the integration of rolled-up microtubes into a polymer matrix patterned by UV-light lithography is feasible without UV-light protectors for non-transparent microtubes. However, the microtubes in this work are constructed from  $\text{SiO}_2$  and transparent to the UV-light.

During the chip fabrication process different kind of photoresists are utilized. Figure 5.11.a depicts that after the spin-coating of photoresist, it can enter the microtube and fills the tube at some extend. However, during the next fabrication step, a negative resist is utilized in order to stay permanently and forming the microchannel structure. Negative resists polymerize and loose solubility by exposure to UV-light. Hence, UV-light protectors are required during the integration process to shield the content of the microtubes from UV-light exposure and avoiding polymerization of SU-8 photoresist inside the microtubes. Otherwise this would lead ultimately to a closed channel by the remaining resist.



**Figure 5.11:** Photolithography on microtubes. (a) Microscope image of a microtube after spin-coating. The tube is partially filled with photoresist. The resist encloses an air bubble in the center of the microtube. (b) Optical image of a microtube with two deposited UV-light protector caps on top.

The UV-light protectors are based on an Au layer sandwiched between Cr deposited onto the microtube (Figure 5.11.b). Chromium improves the adhesion of the Au layer to metal oxides such as Al<sub>2</sub>O<sub>3</sub> and SiO<sub>2</sub>. An additional thin SiO<sub>2</sub> layer on top of the UV-light protectors is required as adhesion agent to the SU-8 polymer layer applied in step 5.<sup>[36]</sup>

### Step 5.1: fabrication of the microfluidic channel system

The fabrication of the microfluidic system employs the photoresist SU-8 10, which is well employed in MEMS and other micro fabricated devices<sup>[33-37]</sup> offering a promising approach to integrate the rolled-up microtubes into microfluidic structures. Several parameters are considered when designing the chip structure, such as the controllable exchange of the microtube's content and constant ambient conditions with a low refractive index medium around the microtube as mentioned in chapter 2.2.

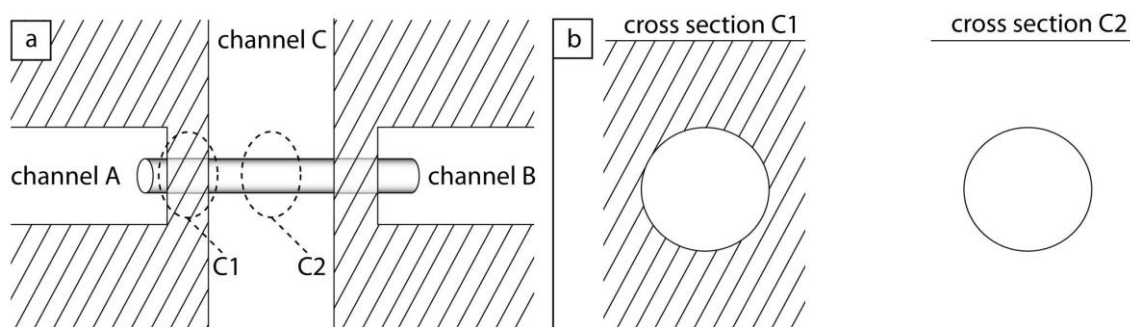


**Figure 5.12:** Sketch of the principle of the microfluidic integration of a microtube. (a) The microtube bridges the channels A and B. Channel C crosses the microtube perpendicular. The channels are defined by a solid material (shaded area). The two dashed circles indicate the position of the cross section C1 and C2 depicted in (b): C1 illustrates that the microtube (circular area) is totally enclosed by the material of the channel wall and the cross section C2 shows that the central part of the microtube is completely enclosed by the material of channel C, which is usually air.

The sketch in Figure 5.12.a illustrates the general design: the microtube bridges two microfluidic channels named A and B. These channels are the in- and outlets for the microtube. Channel C is supposed to contain always air which refractive index is about  $n_{\text{air}} \approx 1$  RIU in order to support the light confinement in the tubular wall by total internal reflection.

The final design of the target substrate is depicted in Figure 5.13 and the photograph in Figure 5.13.a is showing an overview on the microchip structure. The glass substrate contains a microchannel system with three integrated microtubes on top. Each microtube has its own in- and outlet connections for independent filling and sensor characterization studies. There are three pairs of coupling links (CL) highlighted with the colors blue, green and red. The CLs are located where the pinholes of the PDMS lid are. Each CL pair is directly connected to one integrated microtube in the center of the microchip structure. A zoomed-in view to the central part is depicted in the microscope image in Figure 5.13.b. For clarification, the colors of the microchannels correspond to the same color of the CLs in Figure 5.13.a indicating that each of the three integrated microtubes (#1, #2 and #3) can be connected and operated independently. The red dashed circle in Figure 5.13.b highlights one of the four alignment structures visible in this image that remain after the fabrication process and having no further function once the microchip is finally assembled.

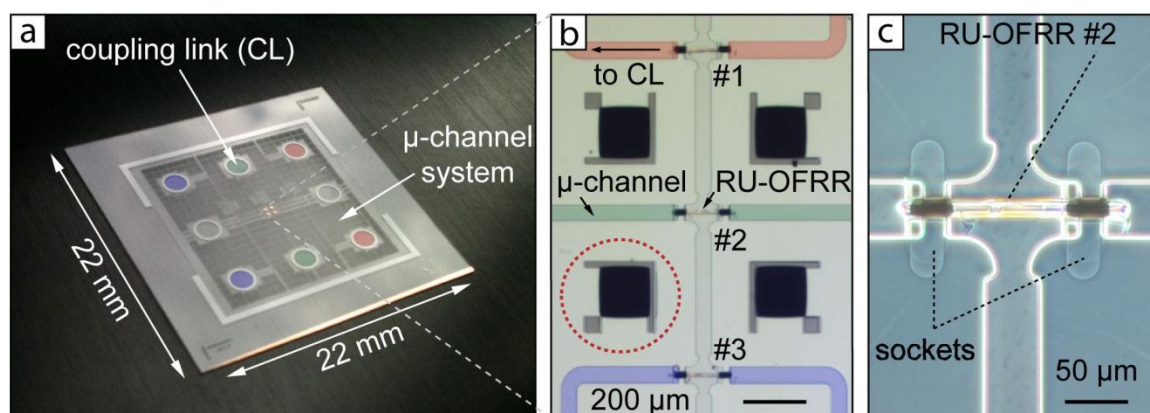


**Figure 5.13:** Overview on the microfluidic structure of the chip. (a) Photograph of the glass substrate with a lateral length of 22 mm. The substrate contains three pairs of coupling links (CL) highlighted with colored circles and a microchannel system connecting these CLs. (b) This optical image is a zoomed view to the center of the microchip structure. The colors of the microchannels correspond to the colors of the CLs in (a). The channel color indicates that the rolled-up OFRRs No. 1, 2 and 3 can be accessed separately. The four large structures (lower left one is highlighted with a red dashed circle) are residues of the alignment structures. (c) dark field image of the central RU-OFRR to highlight the position of the sockets elevating the microtube.

By means of dark field imaging (Figure 5.13.c) a better visualization of the position of each fabricated component such as the microtube, the UV-light protectors and the sockets is possible. The horizontal microchannels bridged by the microtube correspond to the channels A and B from Figure 5.12.a. The vertical microchannel is related to channel C in Figure 5.12.a.

### **Step 5.2: final assembly preparations**

The chip prepared in the previous steps contains all components of the final device. The final layer is a PDMS lid bonded on top of the previously prepared chip structure. The permanent bonding is realized by surface activation utilizing an oxygen plasma as known from fabrication techniques of microfluidic systems.<sup>[17,18]</sup> During O<sub>2</sub> plasma treatment OH groups are formed on the surface of the PDMS whereas a plasma treatment on a SiO<sub>2</sub> surface can break the molecular bonds. When both surfaces get into contact after activation interlayer molecular bonds are formed creating a permanent and strong adhesion between the two materials. However, the bonding strength between PDMS and SU-8 is very low after plasma treatment. Hence, an additional layer of 5 nm of SiO<sub>2</sub> is added to the SU-8 as adhesion agent to enable the permanent bonding between the substrate and the PDMS. The value of the thickness is optimized in order to use the thinnest working SiO<sub>2</sub> layer while maintaining the impact of this additional SiO<sub>2</sub> layer on the optical properties of the microtube minimal. The SiO<sub>2</sub> is deposited by electron beam evaporation.

### **Step 6: final chip**

The prepared substrate from Step 5.2 and the PDMS lid (fabrication see chapter 3.3.2) with drilled pin holes at the correct position are loaded at the same time into an oxygen plasma chamber to activate the surface as McDonald et. al.<sup>[17,18]</sup> explained for the fabrication of MEMS devices utilizing PDMS material. The activation process relies on breaking the atomic bonds on the glass surface and oxidation of the methyl groups on the PDMS surface. After the surface activation both surfaces are brought into contact, the molecules on each surface can recombine with each other to establish a permanent bond. Prior pushing both surfaces gently on each other, the pin holes in the PDMS have to be aligned perfectly to the coupling links on the chip, otherwise the chip is lost since there is no second chance to drill pinholes into the PDMS without harming the substrate.

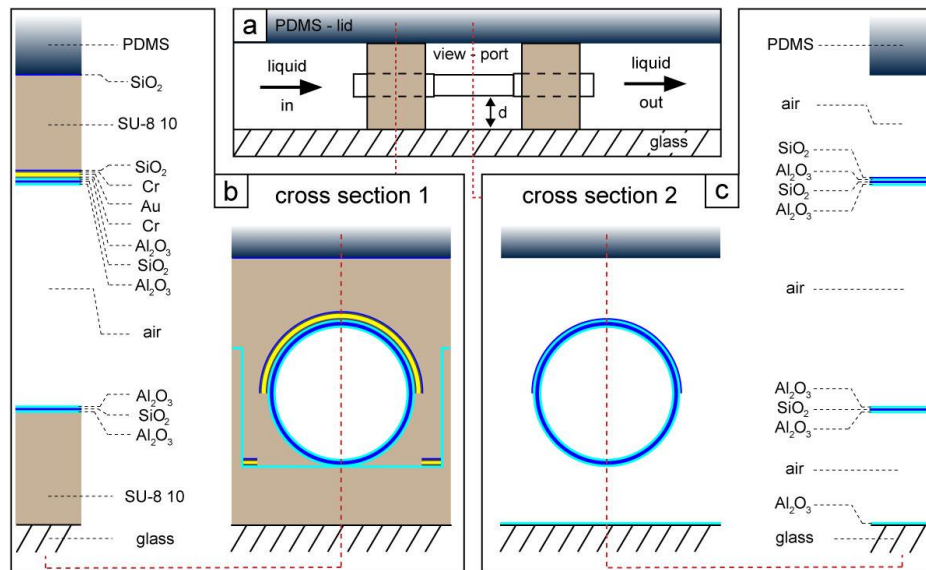


**Figure 5.14:** Overview on the final device structure. (a) Cross section along the microtube connecting the attached fluidic channels. The left channel is the input/liquid-in channel while the right one is set to the output/liquid-out channel. The central part of the microtube is free-standing and has a distance of  $d$  to the substrate. The viewport around the central part of the microtube is separated from the in- and outlet channels by a SU-8 wall. This microchannel layer is enclosed by the glass substrate and the system closing PDMS lid. (b) Detailed cross section of the part of the device where the microtube is enclosed by the SU-8 layer. The left legend shows all utilized materials during the device fabrication with their final location in the device. (c) Detailed cross section of the part of the device where the microtube is free-standing and totally enclosed with environmental air. The right legend shows all material to be found in this part of the device.

A full overview on the final sensor structure is given in the sketches of Figure 5.14. The volume surrounding the centered part of the integrated microtube is called view-port and is confined by the bottom glass and the top PDMS lid as depicted in Figure 5.14.a. The in- and outlets of the microtube are marked with labeled arrows. Cross section 1 and 2 (Figure 5.14.b and Figure 5.14.c) show a detailed view to all the utilized materials during the device fabrication and their location within the device structure.

Cross section 1 depicts an insight into the layered structure of the microfluidic device. The SU-8 layer (brown color) encloses the microtube (SiO<sub>2</sub> ≡ blue and Al<sub>2</sub>O<sub>3</sub> ≡ bright blue ring) and seals it completely. The UV-light protector cap consists of Au (yellow), whereas the Cr and SiO<sub>2</sub> materials are the interlayer adhesion agents between the material of the microtube and the SU-8 from the microchannel structure. In this sketch one can see a thin SiO<sub>2</sub> layer on top of the microtube. This layer originates from the electron beam evaporation of SiO<sub>2</sub> during the final assembly preparation step (5.2). The second cross-section represents the center of the viewport (area with optical sensing properties) showing the free-standing character of the integrated RU-OFRRs. As mentioned above, the Q values of the microtubes are monitored after each integration

step to compare the Q value evolution. The impact of the SiO<sub>2</sub> on top of the microtube and from all previous preparation steps on the Q factor will be shown in chapter 5.4.

### 5.3 Controlling liquids within the microchip

The ability of a precise fluid control at the microscale is a key issue for the development of a microfluidic chip. For this device a pressure based method is developed consisting of two syringes connected to the microchip via flexible and inert polytetrafluoroethylene (PTFE) tubing to drive and control the motion of liquids (Figure 5.15.a). Between working medium, the first analyte segment and all following analyte segments a spacer volume of air is incorporated to avoid mixing of the liquids. In Figure 5.15.b a microscope image depicts a close view to the integrated microtube. The utilized syringes filled with the liquid working medium, in combination with the air gap in the tubing, provide the advantages of pneumatic and hydraulic control and allow a very precise manual control of the fluid in the lower-femto liter range. The air gap between two liquids works as a translator of the applied pressure to lower pressure values. In fact, a larger air gap results in a higher translation due to the compressibility of gas if the same volume is pumped by the syringe.

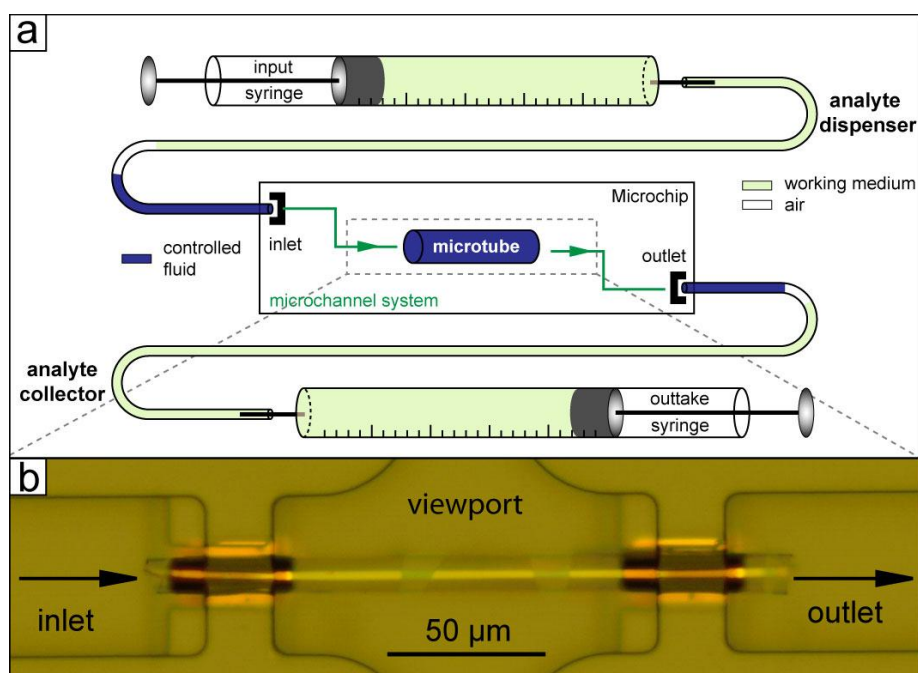


**Figure 5.15:** Integrated microtube. (a) Schematic drawing of the fluidic setup to control liquids in the microchip. An input syringe (analyte dispenser) pushes the fluid (blue) through a microchannels system (green) which guides the fluid to the integrated microtube. At the outlet the fluid will be collected in a tube connected to an outtake syringe (analyte collector). The fluid and the working medium in the syringes are separated by an air gap. (b) Optical image of an integrated microtube. The in- and outlets are indicated by arrows. The viewport surrounds the central part of the microtube.

The image sequence depicted in Figure 5.16 shows the filling (Figure 5.16.a) and emptying (Figure 5.16.b) of a microtube with a liquid. The liquid (DI water, highlighted in blue) is pumped slowly to the microtube and once the liquid contacted the microtube, the microtube is immediately filled. The contact angle between wall and the fluid at the end of the microtube forces the liquid to stop instantly (right end of the microtube in Figure 5.16.a (ii)) since the end is completely suspended in air and no wetting of the outer side of the tube is possible. If an additional pressure is applied to the channels (left side: positive pressure or right side: negative pressure) the right microchannel can be filled. Emptying the microtube required an applied negative pressure of about 100 mBar below ambient conditions.

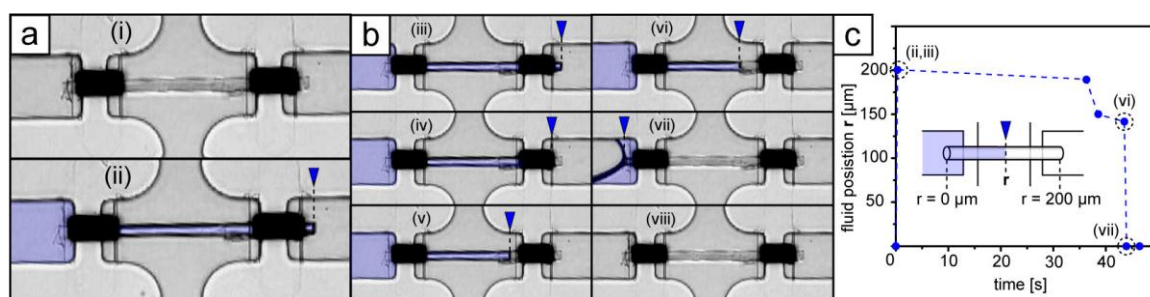


**Figure 5.16:** Sequence of optical images showing filling and emptying of a microtube. The fluid (DI water) is highlighted in blue. (a) Filling of the microtube by capillary forces. The microtube is empty in image (i) and filled in image (ii). (b) Emptying of a microtube by applying negative pressure (iii to viii). (c) Time evolution of the filling level of the microtube. The values of the data points are extracted from the video and correspond to the images in (a) and (b). The schematic inset depicts the time depending filling level  $r$  (interface between air and fluid).

Once the pressure is achieved the fluid/air interface slowly moved backwards through the microtube (Figure 5.16.b (iii) to (vi)). The plot in Figure 5.16.c depicts the entire cycle of the movement of the interface over time from the beginning of the filling until the microtube is emptied. The data is extracted from the recorded video and important points of the filling status of the microtube are highlighted by a dashed circle. The data points correspond to the images depicted in Figure 5.16.a-b and show the position  $r$  of the interface related to the zero point which is the left end of the microtube. The jump from (i) to (ii) indicated the rapid filling by capillary forces. After a certain threshold during emptying the flow resistance in the channel is too weak and so the microtube is emptied almost immediately (jump from vi to vii).

The liquid control can be performed manually or with an automatic control by PC whereas each method has its specific advantages. A remarkable advantage of controlling the liquid manual via a microscope is the available feedback system, only limited by the response time of the controlling person. The controlling person can almost instantly apply positive or negative pressures to the liquid and modify the flow direction in order to pass the sensor part of the microtube several times with the same segment of analyte or object suspended in the liquid. Such an object could be any

kind of particles or even living cells. Figure 5.17 shows an image from a video sequence of controlling the movement of two yeast cells in the microtube by precise manual control. The arrows at the in- and outlets indicate the back and forth movement of the medium. The yeast cells are suspended in a yeast medium in order to maintain them living during the experiment. A video of the accurate control of the yeast medium containing two yeast cells is provided for another publication and can be looked up in the supplementary information of the Lab Chip review on lab-in-a-tube components from Smith et al.[124]. There is no short term influence observed during the work with the cell medium. The successive emptying and filling worked out well.

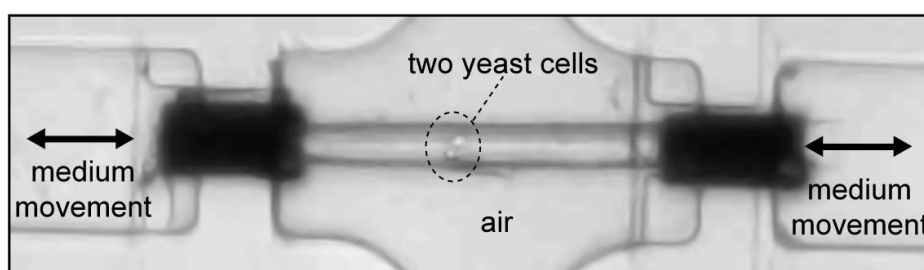


**Figure 5.17:** Moving cells in a microtube. The arrows indicate the back and forth movement of the yeast cell medium containing two yeast.

The automatic control of the fluid is achieved with a syringe pump system connected to a PC with installed controller software. The tracking of the liquid is carried out by utilizing spherical fluorescent polymer particles with a diameter of 1.9  $\mu\text{m}$ . By setting constant flow rates (of up to 2  $\mu\text{L}/\text{min}$ ), liquids can be pumped easily through the microtube over a longer time with the same velocity. The initial particle concentration is about  $1 \cdot 10^5$  particles per  $\mu\text{L}$ . With a flow velocity of 2  $\mu\text{L}/\text{min}$   $2 \cdot 10^5$  particles per minute can pass the microtube. A visualization of the flow in a meander like structure is depicted in Figure 5.18.a (green arrows indicate the direction).

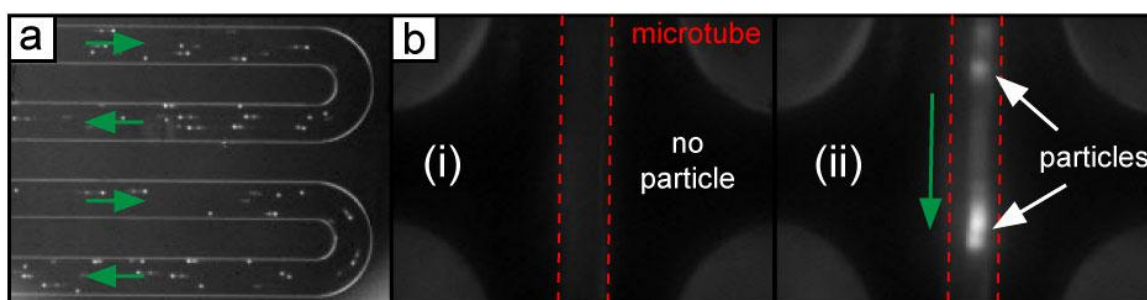


**Figure 5.18:** PC controlled particle movement. (a) Fluorescence image of a section of the microchannel system with a flowing suspension of particles (white dots) whose direction is indicated by the green arrows. (b) Two zoomed-in fluorescence images of the middle part of the microtube (red dashed line indicates the position of microtube). In (i) there is no particle in the microtube and in (ii) there are at least two particles moving through the microtube. The flow direction is indicated by the green arrow.

The two fluorescence images in Figure 5.18.b depict a zoomed-in view on the microtube with no particle (i) and multiple particles (ii) passing the microtube. The red dashed lines in each image highlight the position of the microtube, whereas the green arrow indicates the flow direction.

In conclusion, the microfluidic performance of the developed device has a high potential to work as a screening device for individual objects. The next step is to evaluate the optical properties of the microtubes for sensing applications.

## **5.4 Sensor Characterization**

### **5.4.1 Quality factor ( $Q$ ) evolution**

With finishing the device assembly the collected data of the  $Q$  evolution can now be summarized. The plot in Figure 5.19 shows the  $Q$  value evolution of three integrated microtubes. The microtubes are on the same chip and consequently they went through exactly the same process conditions. The axis of abscissas show only fabrication steps where microtubes are involved starting with the value 2 (numbers related to the fabrication steps in chapter 5.2), in particular after the microtube fabrication. The initial  $Q$  value of each microtube ranges from 450 to 2900. The transfer (step 3.2) mainly involves mechanical forces which lead to stretch, compression and torque forces on the microtube. These forces probably slightly rearrange the rolled-up layers leading to changes in the optical properties. During the microtube fixation (step 4.1) an additional  $\text{Al}_2\text{O}_3$  layer is deposited inside and outside on the tubular wall changing the optical properties. Furthermore, temperatures of up to  $150^\circ\text{C}$  are applied to the microtube during this step. When the UV-light protectors are applied (step 4.2), different organic solvents, the utilized photoresist, developers and temperatures of up to  $110^\circ\text{C}$  could influence the optical properties. After finishing this step, some residues of the resist might remain on the optical active part of the microtube having a size in the nanometer regime. Concerning the utilized materials and applied temperatures, the microchannel fabrication step 5.1 is similar to the one before and leads to minor changes of the  $Q$  value for all three microtubes. The additional  $\text{SiO}_2$  layer on top of the microtubes (step 5.2) creates also small changes of the  $Q$  value. The oxygen plasma treatment during the final assembly step 6 probably removed some polymer residues from the microtube, since this method also can be used for cleaning surfaces. Finally, each microtube has a different  $Q$  value compared to the initial value after the fabrication. The relative numbers given on the right side in Figure 5.19 show the change of  $Q$  of each microtube compared to the first value. Remarkably, the  $Q$  values can also be significantly improved by the integration process as the trend of microtube two (red data points) shows. The  $Q$  of this particular microtube enhanced up to 325 % after final assembly.

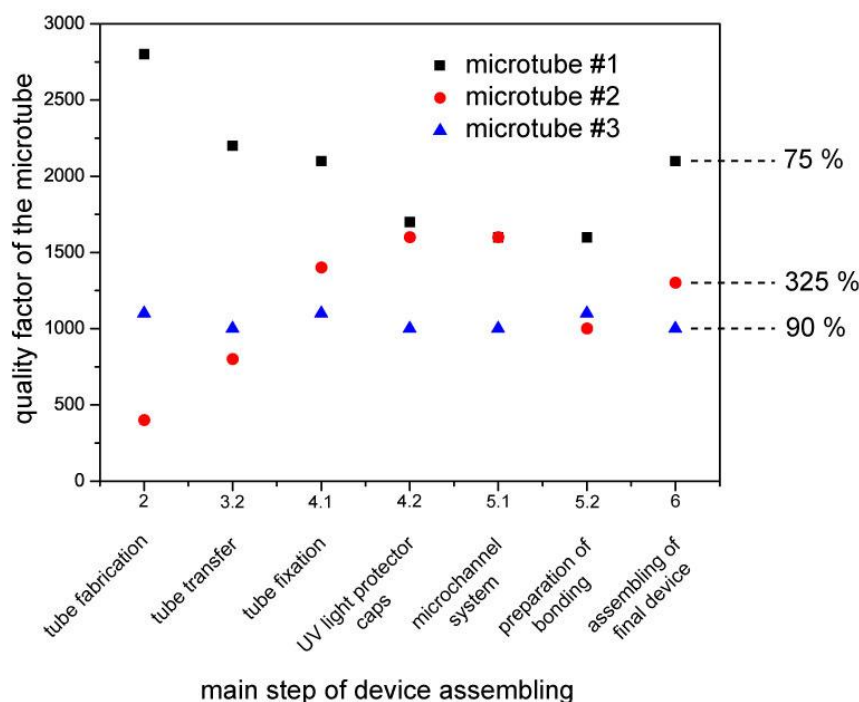


**Figure 5.19:** Quality factor evolution of three integrated rolled-up tubular ring-resonators. The scale depicts main- and sub-steps of the process in which an impact on the optical properties of the microtube is expected. The relative numbers on the right side shows the comparative change of the quality factor related to the first value after the fabrication of the microtube step 2.

The change of the Q value of the microtubes during the integration process is probably referred to nano-gaps in the rolled-up membrane mentioned above. The dispersion in the tubular wall, their size and their behavior during the fabrication process is not controllable and lead to random changes in the optical quality. Even the equal deposition of material, such as the Al<sub>2</sub>O<sub>3</sub>, on all microtubes has different impact on the optical quality. The conclusion on this result is that the integration process maintains the good optical properties of the microtubes. Hence, with this procedure the integration of microtubes for refractometric sensing applications is possible.

#### 5.4.2 Response of the PL spectrum - from air to water

The fluidic connection to the microchip is solved by utilizing a micro pump system with two mounted syringes as the schematic drawing in Figure 5.20 shows. A small volume at the end of the tubing contains the analytes. Prior plugging the tubing to the in- and outlets of the microchip (pin holes in the PDMS) the inlet tubing is filled with segments of different analytes in reverse sensing order. These segments have a volume of 2  $\mu$ L and are separated by an air gap of 2  $\mu$ L whereas the filling is realized by a sequential sucking in of analyte and air. The sketch of Figure 5.20 depicts an example of a sensing sequence, which contains DI water, PBS and PBS with different concentrations of glucose. By pushing the working medium with the input syringe, the sequence of analytes and air gaps is guided to the microtube by the on-chip microchannel system.

After the analyte passed the microtube it is guided to the outlets of the system and can be stored by the collector for further treatment. The device for sensing and read-out of the signal is a PL system with a CW laser (442 nm wavelength) focused on a microtubular rolled-up optofluidic ring resonator as indicated in Figure 5.20.

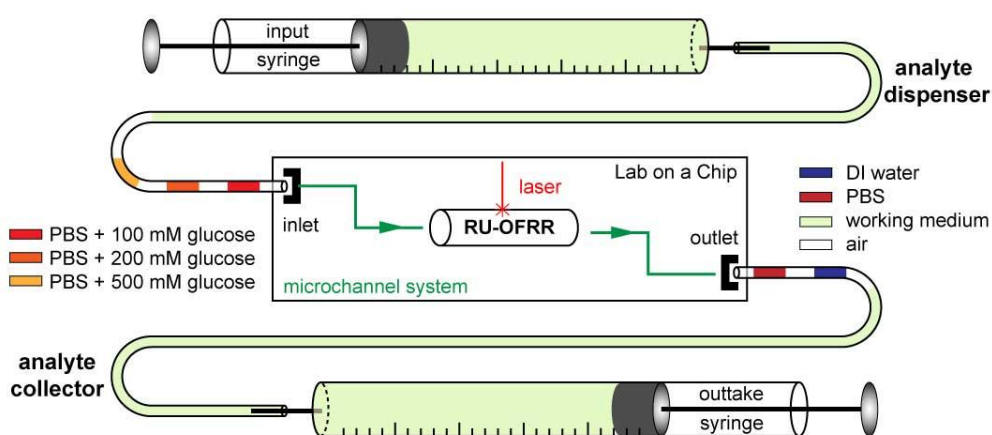


**Figure 5.20:** Schematic drawing of the microfluidic setup. An analyte dispenser and a collector are connected to the chip device. The dispenser pushes the analyte (different colored segments in the tubing) into the device. A microchannel system on the chip guides the analyte to the RU-OFRR which can be excited optically and read out by a PL system. The collector takes the analyzed medium out and can store it.

The sensing mechanism of the RU-OFRR is the response of the resonant modes to the change of the RI inside the microtube. The circulating light within the tubular wall forms an evanescent field which can interact with the volume at the distance of a few hundred nanometers inside and outside the microtube.<sup>[125]</sup> When fluids with different RIs are introduced into the RU-OFRR, the peak positions of the resonant modes change in order to maintain the resonant conditions. The change of the RI is more pronounced if a gaseous phase (e.g. air with  $RI = 1.0$ ) is replaced by a liquid ( $RI \approx 1.333$  for water). The difference in the optical behavior is so remarkable that in consequence it is easy to determine the presence of a liquid inside the RU-OFRR by analyzing the shape of the PL spectrum. Details on the shift and the changes in the PL spectrum are depicted in Figure 5.21 viewing the response of the resonant modes depending on the medium inside the RU-OFRR.

The wavelength ranges to observe the response of the resonant mode is set from 630 to 660 nm in order to detect an appropriate number of resonant modes during a short measurement time (3 seconds). In this range the RU-OFRR create in air three neighboring resonant modes with associated sub-resonances with mode numbers  $m = 63, 62$  and  $61$ . The shape of the spectrum is similar to the presented PL spectrum of a free-standing rolled-up microtube in Figure 5.8.

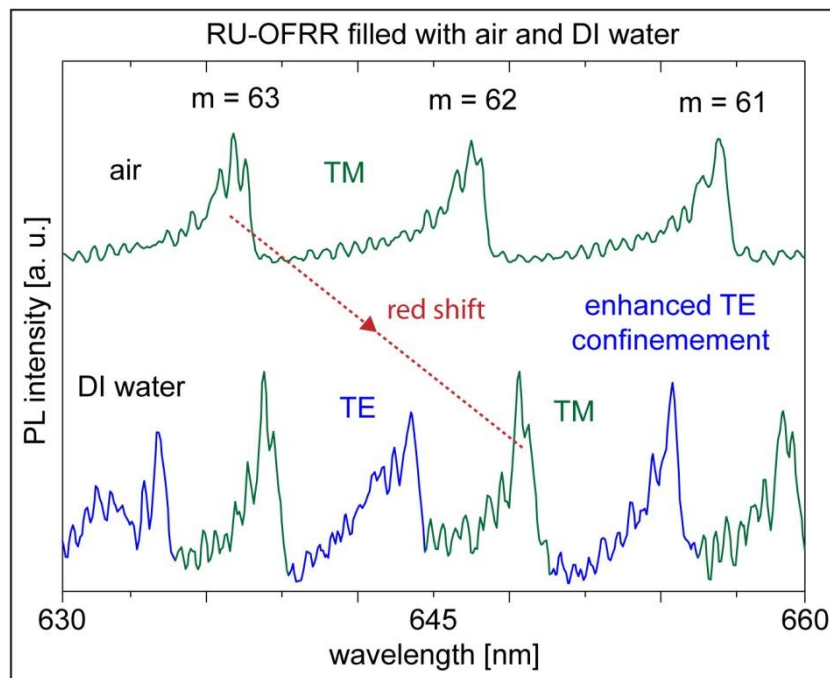


**Figure 5.21:** Resonant mode response to changes of the refractive index. PL spectra of the RU-OFRR with air (top) and DI water (bottom) inside the microtube. The liquid forces the resonant modes to shift to longer wavelengths and to split into TE and TM.

The PL spectra in Figure 5.21 show that without liquid, only transverse-magnetic (TM) polarized modes are confined inside the tube wall, whereas a new group of modes, identified as transverse-electric (TE) polarized modes, appear when a fluid enters the RU-OFRR.<sup>[125,126]</sup> The identification of the TM and TE modes is performed by polarization measurements. The definition of TE and TM modes for microtubes follows the established classification from Hosoda et al. [127]. Briefly, light is electromagnetic radiation and both wall and medium are dielectric. There is no magnetic momentum present in the wall or the medium which could influence the magnetic part of the light. Consequently, only the electric part of the light can interact with wall and medium. In case of TM modes the electrical part oscillates within the wall and is confined by total internal reflection. TE modes instead are perpendicular to TM modes and therefore most part of the electrical field is outside the wall of the microtube if a sub-wavelength wall thickness is present. In case of air inside and outside the wall, no TE modes can be confined because the wall of the microtube is too thin. If a liquid is introduced, the RI inside the tube increases leading to a weaker confinement of light by total internal reflection at the wall-liquid interface. This brings the light to be confined closer to the liquid-wall interface allowing the tube to confine also TE modes because of an effective thicker tubular wall. This difference in the spectra of having a gas or a liquid inside the resonator can be used for a qualitative determination of the state of the matter inside the microtube. Gases (here air) result in single peak resonant modes (only TM), liquids inside result in double peaks (TE and TM) in the same resonant mode.

A red shift of 11 nm after changing the microtube's content from air to DI water clearly detects the difference of the refractive indices between air ( $n \approx 1$ ) and DI water ( $n \approx 1.3330$ ). After a calibration the shift of the mode position can be used to detect the RI of the liquid inside the microtube.

### 5.4.3 Response of the PL spectrum - while drying out

Another upcoming question is what happens to the spectrum if the liquid is removed from the RU-OFRR as described in chapter 5.3 after emptying the microtube? The observed effect is part of the research work of Dr. Libo Ma at the IIN and during the characterization of the integrated microtubes the results of Dr. Ma are confirmed. Closer details on the effect are shown in Figure 5.22.

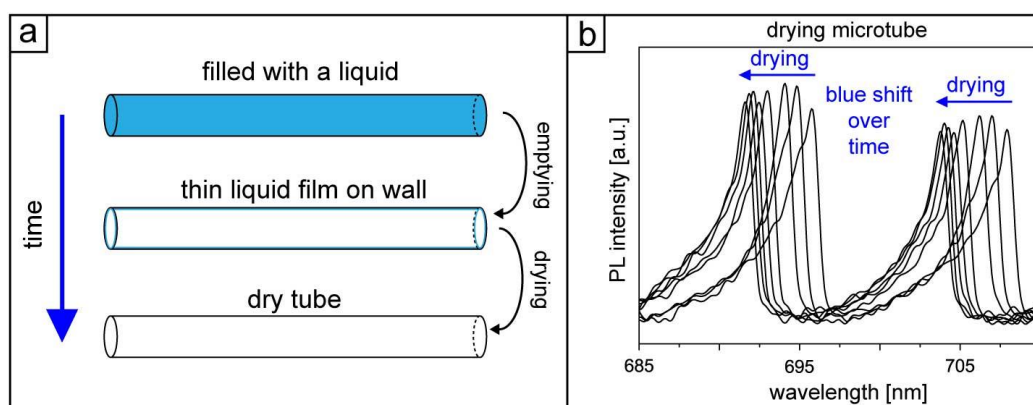


**Figure 5.22:** Drying of a microtube. (a) Sketch of a microtube at different states. (b) PL spectrum shift of a drying ring resonator. The drying of the microtube generates over time a blue shift to shorter wavelengths of the mode peak position.

Concisely, when the status of the microtube turns from filled to emptied (Figure 5.22.a), the inner wall is not dry immediately, the wall is still coated with a thin film of the liquid. This film will dry slowly over time which can be observed by a shift of the PL spectrum to shorter wavelengths as depicted in Figure 5.22.b. The shape of the PL spectrum already looks like if there is only air inside the resonator, but the position of the mode peak is still shifting to lower wavelength (blue shift) and will slowly approach the “dry-air” peak position. The blue shift of the PL spectrum in Figure 5.22.b is observed during 10 minutes measuring every 60 seconds. The air like shape of the spectrum in this case is probably caused by the very low thickness of the liquid film. The film is thick enough to change the effective refractive index to remarkable larger values, but too thin to force TE mode confinement.

#### 5.4.4 Stop-flow signal stability

According to the resonant conditions, the shift of the spectrum is not only sensitive to the RI of material in- and outside of the microtube but it also depends on the tubular diameter.<sup>[23]</sup> A couple of different conditions could change the tubular diameter such as temperature and pressure. In order to probe changes of the tubular diameter over time, the stability of the signal is studied by using a static solution of DI water inside the integrated RU-OFRR and recording the peak position of the most intense peak for each group of TM modes (azimuthal mode numbers 62, 63 and 64) by PL spectroscopy over more than 2 hours, as shown in Figure 5.23.

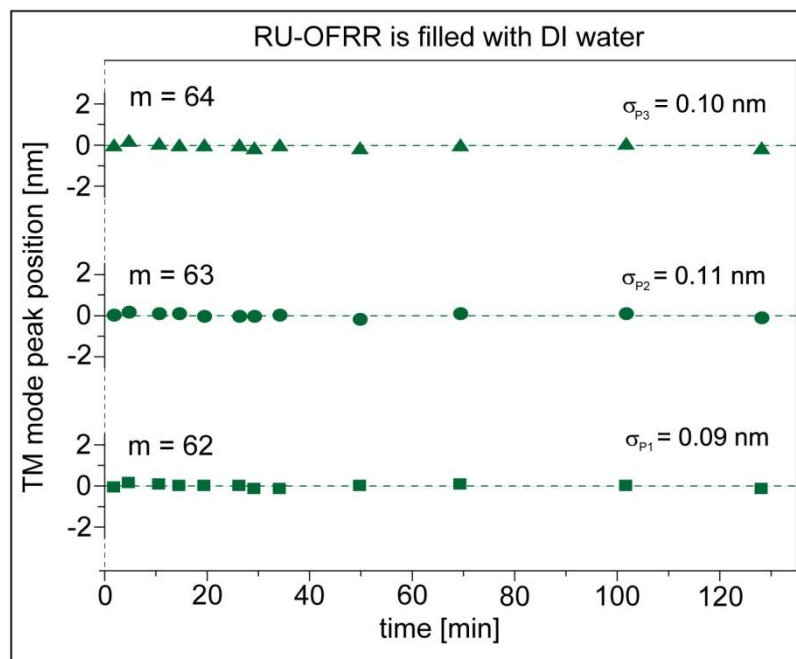


**Figure 5.23:** Determination of the signal stability. Carried out stability by tracking the relative peak position of three side by side positioned TM modes over more than 2 hours; starting with the first position as reference.

The first measurement (time = 0 min) is set as reference peak position for each TM group of modes (position = 0 nm). The peak positions are very stable over time and their variation in wavelength corresponds to a standard deviation  $\sigma_d$  between 0.09 and 0.11 nm, only.

#### 5.4.5 In-flow signal stability

The in-flow investigation on an integrated microtube is carried out by studying the stability and reproducibility of the sensor's response (peak position) when a sequence of two different liquids (DI water and PBS) flows through the RU-OFRR. For this experiment the most intense peak of a single TM group of modes is monitored. The filling of the analyte dispenser is carried out similarly to the example described in Figure 5.20. The tubing is first filled with four segments of 2  $\mu$ l PBS and then two segments of 2  $\mu$ l DI water, each separated by 2  $\mu$ l of air. The two DI water segments are first pumped at a rate of 1  $\mu$ l/min resulting in an average peak position of 688.35 nm

wavelength, as shown in Figure 5.24. According to the higher refractive index of PBS, with a difference RI of  $\Delta n = n_{\text{PBS}} - n_{\text{DI}} = 15 \cdot 10^{-4}$  RIU in respect to DI water, a red shift of the peak position is expected.<sup>[13]</sup>

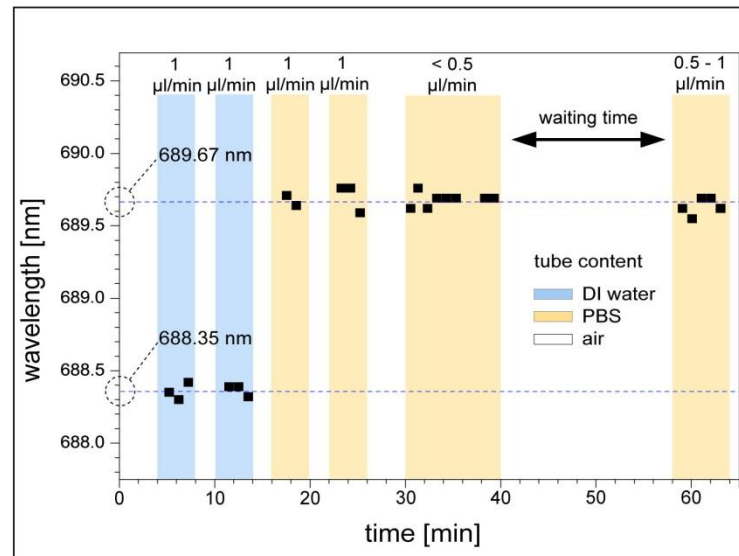


**Figure 5.24:** In-flow studies on a RU-OFRR. Time evolution of the absolute fluctuation of the peak position of one TM mode peak position over more than one hour. The microtube is filled successively with two segments DI water and four segments of PBS at different velocities. The volume of each segment is 2  $\mu\text{l}$ . Each segment is separated by an air gap with a volume of 2  $\mu\text{l}$ . The speed of the liquid varies between < 0.5  $\mu\text{l}/\text{min}$  and 1  $\mu\text{l}/\text{min}$ . The average peak position of the TM mode for DI water is 688.35 nm and for PBS the average position is 689.67 nm.

Once the RU-OFRR is filled with the flowing PBS (rate of 1  $\mu\text{l}/\text{min}$ ) the peak position shifts to an average value of 689.67 nm. Noticeably, the peak position is independent of the flow velocity or the delay time between each segment, proving that the optofluidic response of the RU-OFRR is stable against changes in the flow speed and the in-tube pressure<sup>[112]</sup> respectively.

The sensitivity  $S$  of this RU-OFRR (Figure 5.24) in the RI range between DI water and PBS is calculated by the ratio between the change of the mode peak position  $\Delta\lambda$  and the different refractive index  $\Delta n$  of the liquids using equation 2.8 (values taken from Figure 5.24). The sensitivity  $S$  of about 880 nm/RIU is significantly higher than previously reported values for rolled-up ring resonators.<sup>[13,25]</sup> The relative thinness of the RU-OFRR wall (about 210 nm) with respect to the resonant wavelengths causes this high sensitivity value because it allows the evanescent field of WGM to spread outside the microtube wall.<sup>[24]</sup> Sensitivities are obtained for different integrated RU-OFRR ranging from 472 to 880 nm/RIU. In addition to the high optical quality of the integrated RU-OFRRs, the sensitivity is higher than previous non-integrated rolled-up ring resonators.<sup>[13,45]</sup> The corresponding detection limit (DL) for this RU-OFRR (Figure 5.24) is calculated by the standard deviation of the signal stability and the sensitivity  $S$  using

equation 2.10 to  $DL = 3.4 \cdot 10^{-4} RIU$ . The values of the detection limit range from  $3.4 \cdot 10^{-4}$  to  $6.4 \cdot 10^{-4} RIU$  for several integrated RU-OFRR.

#### 5.4.6 Sensing fluids with different refractive index

In another experiment a number of different liquids are pumped into the integrated sensors using the sensing sequence shown in Figure 5.25 in which DI water and PBS already passed the RU-OFRR sensor unit of the microchip. This sequence is the first part of the tubing filling sequence depicted in Figure 5.20. The arrow of the sensing sequence in Figure 5.25 represent the timeline of the measurement: starting with air, then DI water, air, PBS and air until all analyte segments passed the RU-OFRR and the optical response is recorded by PL spectroscopy.

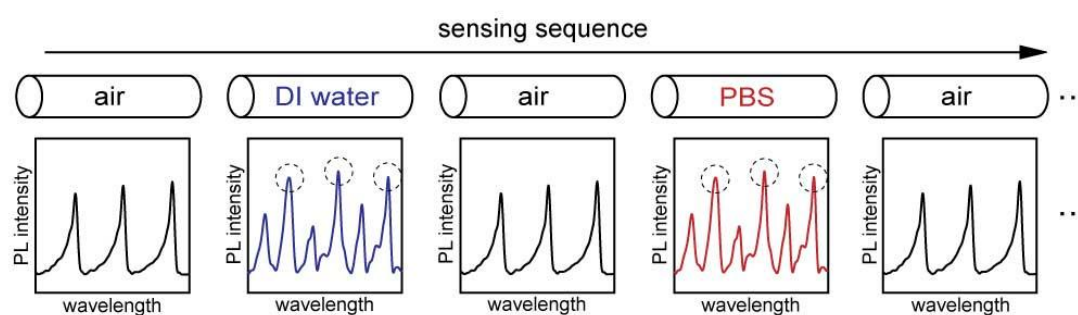


**Figure 5.25:** Example of a sensing sequence detected by PL spectroscopy. The quantitative determination of the liquid is done by monitoring the peak positions (wavelength) of the TM modes (dashed circles).

The microtube-content corresponding PL spectra shown in Figure 5.25 are smoothed to emphasize the shape of the recorded spectrum. The dashed circles in the spectra of DI water and PBS indicate the TM peak positions which have been monitored to compare the spectra of different analytes. The peak positions of three neighboring groups of TM modes (azimuthal mode numbers  $m$  50, 51 and 52) are monitored with respect to the RI of the fluid (data plotted in Figure 5.26). In total five different analytes are utilized to record the optical response of the RU-OFRR. The analytes are in particular DI water, PBS and different concentrations of glucose in PBS (100, 200, 500 mM). The corresponding refractive indices are listed in Table 3.1 at page 22. The blank initial medium is DI water and is pumped through the resonator. The peak position of the first liquid (DI water) is set as a reference point for all measurements. The dashed lines for each mode in Figure 5.26 represent the peak position of the water in the spectrum.

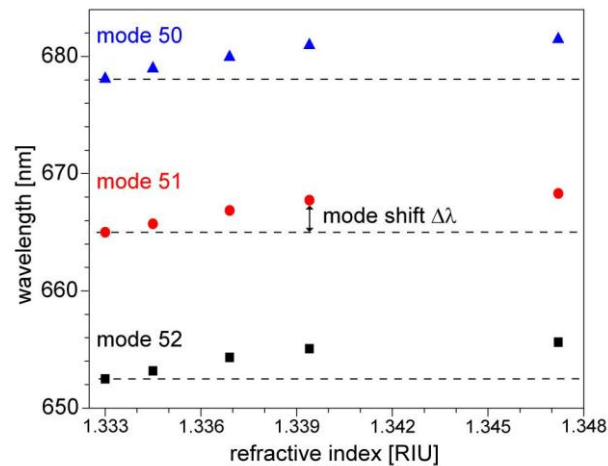


**Figure 5.26:** Sensing the change of refractive index of analytes. Change of the absolute position of three neighboring modes in the PL spectrum depending on the refractive index of the introduced liquid. The mode shift is defined as the distance of the current mode position to the first position at  $n=1.333$  RIU.

The shift to longer wavelengths for all three resonant modes is visible. The evaluation of the linear behavior for this optofluidic sensor is performed by plotting the total shift  $\Delta\lambda$  (relative to DI water) of TM mode  $m=51$  vs. the RI of the liquid (Figure 5.27). There are two different shapes of the plotted curve identified: (i) a linear range (green line) and (ii) a saturation behavior (red dashed line). The linear range involves the analytes DI water, PBS and PBS with 50 mM glucose. The data points for PBS with 100 mM and 200 mM glucose are remarkably displaced from the linear behavior.

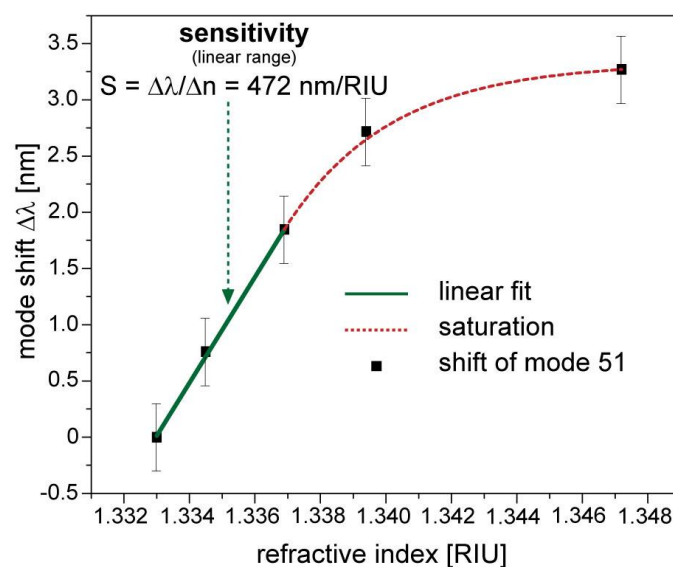


**Figure 5.27:** Mode shift of the peak position of mode 51. In the linear range of the ring resonator the response to the alternating content of the ring resonator is first linear (green line) and then turns over into a saturation (red dashed line) at higher refractive indices. The sensitivity in the linear range has a value of 472 nm/RIU.

It is speculated that beyond a concentration of 100 mM the effect of glucose accumulation on the inner tubular wall deteriorates the sensing capabilities of the RU-OFRR. The interpretation is that the glucose layer is too thick to be penetrated by the evanescent field, which is necessary for sensing. A flowing liquid can reduce the effect of material accumulation but not eliminate it.

Obviously the optical properties of the microtube are modified by the accumulated glucose which can be seen in Figure 5.28. After the strong loss of sensitivity it is decided to empty and dry out the microtube overnight under ambient conditions in order to investigate the impact of the accumulated glucose on the optical properties. Once the microtube is dried it is barely possible to see accumulated material with an optical microtube as depicted in Figure 5.28.a. Only darker shades (arrows point on them) indicate that there could be accumulated glucose.

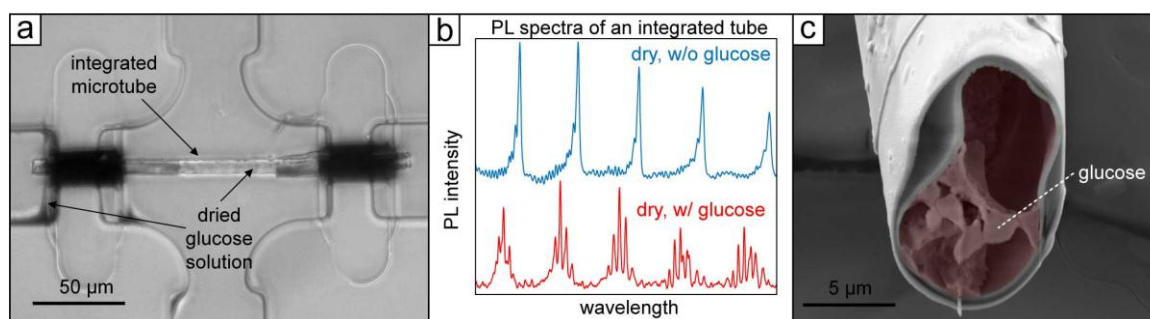


**Figure 5.28:** Different views on a dried out microtube containing glucose. (a) Optical image of the entire microtube. The glucose accumulation can barely be seen and is indicated by arrows. (b) PL spectra of the same microtube shows evident differences before (blue) and after (red) treatment with a glucose solution. (c) SEM FIB-cut image of a dried out microtube resonator. The glucose (highlighted in red) is distributed randomly inside the microtube.

The PL spectrum of the microtube indeed shows remarkable changes of the optical properties. Instead of a single main peak with associated sub-resonances for each mode as known for microtube ring resonators in air (blue spectrum), the resonant modes after drying out (red spectrum) show several peaks (Figure 5.28.b) and also a shift of the strongest pronounced peak to a different wavelength. An expected uniform accumulation of the glucose on the inner tubular wall is not proved as the FIB-cut in Figure 5.28.c shows. Instead the glucose accumulates in random shape within the entire volume. If the oval deformation of the cross section of the microtube is caused by drying glucose or if it is already present after the roll-up process cannot be clarified. However, the modification of the optical properties is evident, even if this modification is simply caused by a random distributed glucose coating on the inner tubular wall.

## 5.5 Conclusions

The integration of rolled-up optofluidic ring resonators with quality factors of up to 2900 into microfluidic devices has been demonstrated. The introduced socket system allows the precise positioning of a large number of microtubes at virtually any location and in any planar orientation on the sample. The control of movement of liquids is very accurate at the femto liter scale and the design of the microfluidic system allows constant flow rates of about 2  $\mu\text{l}$  per minute pushing up to 200 000 particles per minute through the integrated microtubes. With the developed fabrication technique it is possible to integrate optically active microtubes while maintaining their optical properties at a high quality level where refractometric sensing applications are possible. The integrated RU-OFRRs can detect changes in the RI of liquids flowing through the channels with sensitivities of up to 880 nm/RIU which is the highest value observed for tubular optical microcavities to date. Furthermore, the high sensitivity allows a minimum detection limit of  $3.4 \cdot 10^{-4}$  per refractive index unit (RIU) which is comparable to commercial available Abbe-Refractometer. The optical capabilities of a single glass microtube, and the integration approaches including the transfer of microtubes to specific locations into a microchip device, open many new applications such as label-free sensors, integrated dye lasers, on-chip catalytic micropumps and on-chip flow cytometer as stand-alone devices or additional components in already existing<sup>[128]</sup> Lab-on-a-Chip devices. As an example, the socket system would allow the placement, integration and combination of microtubes with different functionalities such as rolled-up giant magneto resistant sensors<sup>[56]</sup> or rolled-up temperature controllers<sup>[129]</sup> in order to create complex and efficient measurement devices for analytes.

An evaluation of the performance of RU-OFRRs from this work in comparison to similar devices developed by other research groups is shown below in Table 5.1. Aside from the detection limit, all values are measured data. The DL given by other groups shows the potential of the presented device and not the effective performance as given for the demonstrator devices in this work.

**Table 5.1.** Performance of different OFRRs.

	<b>RU-OFRR (this work)</b>	<b>LCORR Ref. [111]</b>	<b>LCOMRR Ref. [25]</b>	<b><math>\mu\text{C-ruRR}</math> Ref. [13]</b>	<b>LRROS Ref. [130]</b>	<b><math>\mu\text{OFRR}</math> Ref. [95]</b>	<b>capillaries Ref. [112]</b>
DL <sub>cal</sub> [RIU]	$2.2 \cdot 10^{-6}$	$1 \cdot 10^{-6}$	0.05	$1.4 \cdot 10^{-4}$	n/a	n/a	$1 \cdot 10^{-4}$
S [nm/RIU]	880	20	62	425	800	n/a	390
LoC integration	yes	difficult	no	no	no	planned	difficult
Q	$2.9 \cdot 10^3$	$1.2 \cdot 10^6$	n/a (low)	$6 \cdot 10^2$	n/a	$1.2 \cdot 10^4$	$5 \cdot 10^2$
diameter [ $\mu\text{m}$ ]	8 – 12	100	2	7 – 9	100	50 – 200	8-10
wall thickness	$\approx 200$ nm	2.3 $\mu\text{m}$	90 nm	$\approx 200$ nm	0 $\mu\text{m}$	2 $\mu\text{m}$	0.75-0.9 $\mu\text{m}$

The method for calculating  $DL_{cal}$  is described using data of the presented RU-OFRRs with the highest sensitivity. The signal fluctuation of  $\sigma_d = 0.1$  nm of the sensor signal in this work is already close to the spectral resolution of the employed PL system of  $R_{spec} = 0.02$  nm. In case of a more stable system with a remarkable higher spectral resolution a theoretical detection limit  $DL_{cal}$  of the RU-OFRRs can be calculated. A better DL is expectable if the sensor resolution  $R_{sens}$  (the minimal resolvable spectral shift of the resonance mode) of a microtube is used instead of  $3\sigma_d$ . Thus, assuming  $R_{sens} = 0.5$  nm / 50 = 0.002 nm where  $R_{sens}$  is usually chosen to be 1/50 to 1/100 of the resonant mode linewidth<sup>[13,25,95,111,112,130]</sup> (about 0.5 nm in this work), a detection limit  $DL_{cal} = R_{sens}/S = 2.2 \cdot 10^{-6}$  RIU can be calculated using the sensitivity of  $S = 880$  nm/RIU. The calculated detection limit is already close to the values of LCORRs due to the high sensitivity of the RU-OFRRs.

Sensitivity, LoC integration status and the characteristics of the tubular structure in dimension turn out to be very competitive compared to other similar state-of-the-art devices.

## ***6 Conclusion and Outlook***

This doctoral thesis attempts to give an insight into potential applications of microtubes made of the composite  $\text{SiO}_x$  materials, fabricated using rolled-up nanotech on polymers. These applications cover a variety of scientific fields such as bio-physics, analytical chemistry, optics and fluidics. The main concern is to investigate the suitability of rolled-up microtubes for Lab-on-a-Chip devices which can ultimately lead to applications in mobile devices designed for the point-of-care concept.

The first part of this thesis focused on the reproducible mass fabrication of well-aligned  $\text{SiO}_x$  microtubes on-chip in order to build up a basic framework for further investigation. A variety of potential applications are presented such as artificial scaffolds for cells in order to investigate the behavior of living objects in narrow cavities, catalytic microtubes as cargo transporters and micro/nano tools for in-vivo machining. Further applications such as rolled-up micro injection needles, micropumps and a new and powerful type of valve for LoC devices are also motivated. The scope of applications finished with a potential application of  $\text{SiO}_x$  microtubes as optical sensors in Lab-on-a-Chip devices, which is the main concern of the second part of the thesis.

In this second part, a novel approach to integrate optically active  $\text{SiO}_2$  microtubes into a LoC device is carried out. The introduced socket system enables the exact positioning of an arbitrary number of microtubes at any location and any orientation on a substrate made of any given material. Several microtubes are integrated into a microfluidic channel system achieving a microfluidic system with three independent working optical active microtubes. These fluidic capabilities showed that the control of different liquids and suspensions containing particles or cells can be carried out accurately both manually and per software. The investigation on the sensing capabilities of the integrated microtubes is performed with liquids of different refractive indices. We found, that the signal stability of static medium as well as of liquids in-flow is high, and already close to the detection limit of the employed PL system. The achieved sensitivity as well the detection limit of the integrated microtubes reached and even exceeded the values of other optofluidic sensors working with the same sensing mechanism.

Other foreseen applications of microtubes employing the developed integration technique are, for instance, a cell cytometer for counting cells and to distinguish different cells, a micro-valve as a small completely integrated on-chip actuator and a dye laser integrated into a Lab-on-a-Chip device. All of these possible applications can push the point-of-care concept forward.



## ***Bibliography***

---

- [1] O. G. SCHMIDT, K. EBERL. *Thin solid films roll up into nanotubes*. Nature, **410**, 168 (2001).
- [2] V. YA. PRINZ, V. A. SELEZNEV, A. K. GUTAKOVSKY, A. V. CHEHOVSKIY, V. V. PREOBRAZHENSKII, M. A. PUTYATO, T. A. GAVRILOVA. *Free-standing and overgrown InGaAs/GaAs nanotubes, nanohelices and their arrays*. Physica E, **6**, 828-831 (2000).
- [3] P. CENDULA, S. KIRAVITTAYA, Y. F. MEI, C. DENEKE, O. G. SCHMIDT. *Bending and wrinkling as competing relaxation pathways for strained free-hanging films*. Phys. Rev. B, **79**, 085429 (2009).
- [4] S. M. HARAZIM, P. FENG, S. SANCHEZ, C. DENEKE, Y. F. MEI, O. G. SCHMIDT. *Integrated sensitive on-chip ion field effect transistors based on wrinkled InGaAs nanomembranes*. Nanoscale Res. Lett., **6**, 215 (2011).
- [5] Y. F. MEI, D. J. THURMER, F. CAVALLO, S. KIRAVITTAYA, O. G. SCHMIDT. *Semiconductor Sub-Micro-/Nanochannel Networks by Deterministic Layer Wrinkling*. Adv. Mat., **19**, 2124-2128 (2007).
- [6] Y. F. MEI, S. KIRAVITTAYA, S. HARAZIM, O. G. SCHMIDT. *Principles and applications of micro and nanoscale wrinkles*. Materials Science and Engineering R, **70**, 209-224 (2010).
- [7] S. PRUSS, M. FRAISER, D. J. BOTTJER. *Proliferation of Early Triassic wrinkle structures: Implications for environmental stress following the end-Permian mass extinction*. Geology, **32**, 461-464 (2004).
- [8] W. BAO, F. MIAO, Z. CHEN, H. ZHANG, W. JANG, C. DAMES, C. N. LAU. *Controlled ripple texturing of suspended graphene and ultrathin graphite membranes*. Nat. Nano. **4**, 562-566 (2009).
- [9] Y. F. MEI, G. HUANG, A. A. SOLOVEV, E. BERMUDEZ, URENA, I. MÖNCH, F. DING, T. REINDL, R. K. Y. FU, P. K. CHU, O. G. SCHMIDT. *Versatile Approach for Integrative and Functionalized Tubes by Strain Engineering of Nanomembranes on Polymers*. Adv. Mat., **20**, 4085-4090 (2008).
- [10] S. M. HARAZIM, W. XI, C. K. SCHMIDT, S. SANCHEZ, O. G. SCHMIDT. *Fabrication and applications of large arrays of multifunctional rolled-up SiO/SiO<sub>2</sub> microtubes.*, J. Mat. Chem., **22**, 2793-3256 (2012).

- 
- [11] G. HUANG, Y. MEI, D. J. THURMER, E. CORIC, O. G. SCHMIDT. *Rolled-up transparent microtubes as two-dimensionally confined culture scaffolds of individual yeast cells.*, Lab Chip, **9**, 263-268 (2008).
- [12] G. HUANG, S. KIRAVITTAYA, V. A. BOLAÑOS QUIÑONES, F. DING, M. BENYOUCEF, A. RASTELLI, Y. F. MEI, O. G. SCHMIDT. *Optical properties of rolled-up tubular microcavities from shaped nanomembranes.* Appl. Phys. Lett., **94**, 141901 (2009).
- [13] G. HUANG, V. A. BOLAÑOS QUIÑONES, F. DING, S. KIRAVITTAYA, Y. MEI, O. G. SCHMIDT. *Rolled-Up Optical Microcavities with Subwavelength Wall Thicknesses for Enhanced Liquid Sensing Applications.* ACS Nano, **4**, 3123-3130 (2010).
- [14] W. DEMTRÖDER. *Experimantalphysik 1: Mechanik und Wärme.* Heidelberg: Springer, 3rd ed., p. 248 (2005).
- [15] C.-H. CHEN, J. G. SANTIAGO. *A Planar Electroosmotic Micropump.* J. Micromechan. Microeng., **11**, 672-683 (2002).
- [16] R. B. SCHOCH, J. HAN, P. RENAUD. *Transport phenomena in nanofluidics.* Rev. Mod. Phys., **80**, 839-883 (2008).
- [17] J. C. MCDONALD, G. M. WHITESIDES. *Poly(dimethylsiloxane) as a Material for Fabricating Microfluidic Devices.* Accounts of Chemical Research, **35**, 491-499 (2002).
- [18] J. C. MCDONALD, D. C. DUFFY, J. R. ANDERSON, D. T. CHIU, H. WU, O. J. A. SCHUELLER, G. M. WHITESIDES. *Fabrication of Microfluidic Systems in Poly(dimethylsiloxane).* Electrophoresis, **21**, 27-40 (2000).
- [19] E. SOLLIER, C. MURRAY, P. MAODDI, D. D. CARLO. *Rapid prototyping polymers for microfluidic devices and high pressure injections.* Lab Chip, **11**, 3752-3765 (2011).
- [20] H. CHEN, Y. ZHAO, J. LI, M. GUO, J. WAN, D. A. WEITZ, H. A. STONE. *Reactions in double emulsions by flow-controlled coalescence of encapsulated drops.* Lab Chip, **11**, 2313-2315 (2011).
- [21] G. BOAS et al.. *Optofluidics and the Real World Technologies Evolve to Meet 21st Century Challenges.* www.photonics.com, article ID 47300, (2011).
- [22] C. YANG, D. PSALTIS. *Optofluidics can create small, cheap biophotonic devices.* <http://www.laserfocusworld.com>, article 07/01/(2006).

- 
- [23] X. FAN, I. M. WHITE, S. I. SHOPOVA, H. ZHU, J. D. SUTER, Y. SUN. *Sensitive optical biosensors for unlabeled targets: A review*. Anal. Chim. Acta, **620**, 8-26 (2008).
- [24] I. M. WHITE, H. OVEYS, X. FAN. *Liquid-core optical ring resonator*. Opt. Lett., **31**, 1319-1321 (2006.)
- [25] A. BERNARDI, S. KIRAVITTAYA, A. RASTELLI, R. SONGMUANG, D. J. THURMER, M. BENYOUCEF, O. G. SCHMIDT. *On-chip Si/SiO<sub>x</sub> microtube refractometer*. Appl. Phys. Lett., **93**, 094106 (2008).
- [26] F. VOLLMER, S. ARNOLD. *Whispering-gallery-mode biosensing: label-free detection down to single molecules*. Nature Methods, **5**, 591-596 (2008).
- [27] Y. SUN, X. FAN. *Optical ring resonators for biochemical and chemical sensing*. Anal. Bioanal. Chem., **399**, 205-211 (2011).
- [28] R.K. CHANG, A.J. CAMPILLO. *Optical Processes in Microcavities.*, Singapore, World Scientific Publishing Co Pte Ltd (1996).
- [29] H. LI, X. FAN. *Characterization of sensing capability of optofluidic ring resonator biosensors*. Appl. Phys. Lett. **97**, 011105 (2010).
- [30] I. M. WHITE, X. FAN. *On the performance quantification of resonant refractive index sensors*. Opt. Expr., **16**, 1020-1028 (2008).
- [31] S.E. LYSHEVSKI. MEMS and NEMS: Systems, Devices, and Structures. CRC Press, Boca Raton (2002).
- [32] ROLAND ZENGERLE. *Mikrosystemtechnik 1*, Onlinescript (2011).
- [33] S. TUOMIKOSKI, S. FRANSSILA. *Wafer-Level Bonding of MEMS Structures with SU-8 Epoxy Photoresist*. Physica Scripta, **T114**, 223-226 (2004).
- [34] S. TUOMIKOSKI, S. FRANSSILA. *Free-standing SU-8 microfluidic chips by adhesive bonding and release etching*. Sensors and Actuators A, **120**, 408-415 (2005).
- [35] C. K. CHUNG, Y. Z. HONG. *Surface modification of SU-8 photoresist for shrinkage improvement in a monolithic MEMS microstructure*. J. Micromech. Microeng., **17**, 207-212 (2007).

- 
- [36] H.-K. CHANG, Y.-K. KIM. *UV-LIGA process for high aspect ratio structure using stress barrier and C-shaped etch hole*. *Sensors and Actuators*, **84**, 342-350 (2000).
- [37] K. WOUTERS, R. PUERS. *Diffusing and swelling in SU-8: insight in material properties and processing*. *J. Micromech. Microeng.*, **20**, 095013 (2010).
- [38] J. PIVOT. *Mechanical Properties of SiO<sub>x</sub> Thin Films*. *Thin Solid Films*, **89**, 175-190 (1982).
- [39] R. L. PUURUNEN. *Surface chemistry of atomic layer deposition: A case study for the trimethylaluminum/water process*. *J. Apl. Phys.*, **97**, 121301 (2005).
- [40] Cambridge NanoTech Inc. *Savannah 100 & 200 Atomic Layer Deposition System*. User Manual (2007).
- [41] S. J. B. REED. *Electron probe microanalysis*. In P. J. Poots, J. F. W. Bowles, S. J. B. Reed and M. R. Cave, Editors, *Microprobe Techniques in Earth Sciences*. P. 49. Chapman & Hall London, Glasgow, New York, Tokyo, Melbourne and Madras (1995).
- [42] D. C. JOY. *Scanning Reflection Electron Microscopy*. In S. Amelinckx, D. van Dyck, J. van Landhuyt and G. van Tendeloo, Editors, *Handbook of Microscopy*. Vol. II P. 539. VCH Verlagsgesellschaft Weinheim (1997).
- [43] L. KARSTEN. *Photolumineszenzspektroskopie an Halbleiterquantenpunkten*. Cuvillier, E; 1st ed., (2004).
- [44] H. ZHU, I. M. WHITE, J. D. SUTER, X. FAN. *Phage-based label-free biomolecule detection in an opto-fluidic ring resonator*. *Biosensors and Bioelectronics*. **24**, 461-466 (2008).
- [45] E. J. SMITH, S. SCHULZE, S. KIRAVITTAYA, Y. MEI, S. SANCHEZ, O. G. SCHMIDT. *Lab-in-a-Tube: Detection of Individual Mouse Cells for Analysis in Flexible Split-Wall Microtube Resonator Sensors*. *Nano Lett.*, **11**, 4037-4042 (2011).
- [46] G. YANG, I. M. WHITE, X. FAN. *An opto-fluidic ring resonator biosensor for the detection of organophosphorus pesticides*. *Sens. Actuators B*, **133**, 105-112 (2008).
- [47] I. M. WHITE, H. OVEYS, X. FAN. *Integrated multiplexed biosensors based on liquid core optical ring resonators and antiresonant reflecting optical waveguides*. *Appl. Phys. Lett.*, **89**, 191106 (2006).
- [48] S. SANCHEZ, A. A. SOLOVEV, S. M. HARAIZIM, O. G. SCHMIDT. *Microbots Swimming in the Flowing Streams of Microfluidic Channels*. *J. Am. Chem. Soc.*, **133**, 701-703 (2011).

- 
- [49] S. SANCHEZ, A. A. SOLOVEV, S. SCHULZE, O. G. SCHMIDT. *Controlled manipulation of multiple cells using catalytic microbots*. Chem. Commun., **47**, 689-700 (2011).
- [50] A. A. SOLOVEV, S. SANCHEZ, M. PUMERA, Y. F. MEI, O. G. SCHMIDT. *Magnetic Control of Tubular Catalytic Microbots for the Transport, Assembly, and Delivery of Micro-objects*. Adv. Funct. Mat., **20**, 2430-2435 (2010).
- [51] S. SANCHEZ, A.A. SOLOVEV, Y. F. MEI, O. G. SCHMIDT. *Dynamics of Biocatalytic Microengines Mediated by Variable Friction Control*. J. Am. Chem. Soc., **132**, 13144-13145 (2010).
- [52] Y. F. MEI, A. A. SOLOVEV, S. SANCHEZ, O. G. SCHMIDT. *Rolled-up nanotech on polymers: from basic perception to self-propelled catalytic microengines*. Chem. Soc. Rev., **40**, 2109-2119 (2011).
- [53] S. SANCHEZ, A. N. ANANTH, V. M. FOMIN, M. VIEHRIG, O. G. SCHMIDT. *Superfast Motion of Catalytic Microjet Engines at Physiological Temperature*. **133**, 14860-14863 (2011).
- [54] S. BALASUBRAMANIAN, D. KAGAN, C.-M. J. HU, S. CAMPUZANO, A. J. LOBO-CASTANON, N. LIM, D. Y. KANG, M. ZIMMERMANN, L. ZHANG, J. WANG. *Micromachine-Enabled Capture and Isolation of Cancer Cells in Complex Media*. Ange. Chem. Int. Ed., **50**, 4161-4164 (2011).
- [55] D. KAGAN, S. CAMPUZANO, S. BALASUBRAMANIAN, F. KURALAY, G.-U. FLECHSIG, J. WANG. *Functionalized Micromachines for Selective and Rapid Isolation of Nucleic Acid Targets from Complex Samples*. Nano Lett., **11**, 2083-2087 (2011).
- [56] I. MÖNCH, D. MAKAROV, R. KOSEVA, L. BARABAN, D. KARNAUSHENKO, C. KAISER, K.-F. ARNDT, O. G. SCHMIDT. *Rolled-Up Magnetic Sensor: Nanomembrane Architecture for In-Flow Detection of Magnetic Objects*. ACS Nano, **5**, 7436-7442 (2011).
- [57] S. SCHULZE, G. HUANG, M. KRAUSE, D. AUBYN, V. A. BOLANOS QUINONES, C. K. SCHMIDT, Y. F. MEI, O. G. SCHMIDT. *Morphological Differentiation of Neurons on Microtopographic Substrates fabricated by Rolled-Up Nanotechnology*. Adv. Eng. Mater., **12**, B558-B564 (2010).
- [58] S. ZAKHARCHENKO, E. SPERLING, L. IONOV. *Fully Biodegradable Self-Rolled Polymer Tubes A Candidate for Tissue Engineering Scaffolds*. Biomacromolecules, **12**, 2211-2215 (2011).

- 
- [59] M. YU, Y. HUANG, J. BALLWEG, H. SHIN, M. HUANG, D. E. SAVAGE, M. G. LAGALLY, E. W. DENT, R. H. BLICK, J. C. WILLIAMS. *Semiconductor Nanomembrane Tubes Three-Dimensional Confinement for Controlled Neurite Outgrowth*. ACS Nano, **5**, 2447-2457 (2011).
- [60] A. A. SOLOVEV, Y. F. MEI, E. BERMUDEZ URENA, G. HUANG, O. G. SCHMIDT. *Catalytic Microtubular Jet Engines Self-Propelled by Accumulated Gas Bubbles*. Small, **5**, 1688-1692 (2009).
- [61] C. DENEKE, C. MÜLLER, N. Y. JIN-PHILLIPP, O. G. SCHMIDT. *Diameter scalability of rolled-up In(Ga)AsGaAs nanotubes*. Semicond. Sci. Technol., **17**, 1278-1281 (2002).
- [62] M. PUMERA. *Nanomaterials meet microfluidics*. Chem. Commun., **47**, 5671-5680 (2011).
- [63] M. GRUNDMANN. *Nanoscroll formation from strained layer heterostructures*. Appl. Phys. Lett., **83**, 2444-2446 (2003).
- [64] C.-H. HSUEH. *Modeling of elastic deformation of multilayers due to residual stresses and external bending*. J. Appl. Phys., **91**, 9652-9656 (2002).
- [65] G. CARLOTTI, L. DOUCET, M. DUPEUX. *Elastic properties of silicon dioxide films deposited by chemical vapour deposition from tetraethylorthosilicate*. Thin Solid Films, **296**, 102-105 (1997).
- [66] D. J. THURMER, C. DENEKE, Y. F. MEI, O. G. SCHMIDT. *Process integration of microtubes for fluidic applications*. Appl. Phys. Lett., **89**, 223057 (2006).
- [67] A. A. SOLOVEV, S. SANCHEZ, Y. MEI, O. G. SCHMIDT. *Tunable catalytic tubular micro-pumps operating at low concentrations of hydrogen peroxide*. Phys. Chem. Chem. Phys., **13**, 10131-10135 (2011).
- [68] R. SONGMUANG, A. RASTELLI, S. MENDACH, O. G. SCHMIDT. *SiO<sub>x</sub> Si radial superlattices and microtube optical ring resonators*. Appl. Phys. Lett., **90**, 091905 (2007).
- [69] L. X. YI, J. HEITMANN, R. SHOLZ, M. ZACHARIAS. *Si rings, Si clusters, and Si nanocrystals—different states of ultrathin SiO<sub>x</sub> layers*. Appl. Phys. Lett., **81**, 4248-4250 (2002).
- [70] B. GEIGER, J. P. SPATZ, A. D. BERSHADSKY. *Environmental sensing through focal adhesions*. Nature Rev. Mol. Cell Biol., **10**, 21-33 (2009).

- 
- [71] S. BRITLAND, C. PERRIDGE, M. DENYER, H. MORGAN, A. CURTIS, C. WILKINSON. *Morphogenetic guidance cues can interact synergistically and hierarchically in steering nerve cell growth*. *Exp. Biol. Online*, **1**, 2 (1996).
- [72] C. S. CHEN, M. MRKSICH, S. HUANG, G. M. WHITESIDES, D. E. INGBER. *Geometric Control of Cell Life and Death*. *Science*, **276**, 1425-1428 (1997).
- [73] M. M. STEVENS, J. H. GEORGE. *Exploring and Engineering the Cell Surface Interface*. *Science*, **310**, 1135-1138 (2005).
- [74] S. M. SCHWARTZ, R. L. HEIMARK, M. W. MAJESKY. *Developmental Mechanisms Underlying Pathology of Arteries*. *Physiol. Rev.*, **70**, 1177-1209 (1990).
- [75] P. L. HORDIJK, E. ANTHONY, F. P. J. MUL, R. RIENSTMA, L. C. J. M. OOMEN, D. ROOS. *Vascular-endothelial-cadherin modulates endothelial monolayer permeability*. *J. Cell. Sci.*, **112**, 1915-1923 (1999).
- [76] M. J. WHELOCK, K. R. JOHNSON. *Cadherin-mediated cellular signaling*. *Curr. Opin. Cell Biol.*, **15**, 509-514 (2003).
- [77] G. FENTEANY, P. A. JANMEY, T. P. STOSSEL. *Signaling pathways and cell mechanics involved in wound closure by epithelial cell sheets*. *Curr. Biol.*, **10**, 831-838 (2000).
- [78] D. E. INGBER. *Mechanical Signaling and the Cellular Response to Extracellular Matrix in Angiogenesis and Cardiovascular Physiology*. *Circ. Res.*, **91**, 877-887 (2002).
- [79] J. L. TAN, J. TIEN, D. M. PIRONE, D. S. GRAY, K. BHADRIRAJU, C. S. CHEN. *Cells lying on a bed of microneedles: An approach to isolate mechanical force*. *Proc. Natl. Acad. Sci.*, **100**, 1484-1489 (2003).
- [80] M. GHIBAUDO, J.-M. DI MEGLIO, P. HERSEN, B. LADOUX. *Mechanics of cell spreading within 3D-micropatterned environments*. *Lab Chip*, **11**, 805-812 (2011).
- [81] D. A. BRUZEWICZ, A. P. MCGUIGAN, G. M. WHITESIDES. *Fabrication of a modular tissue construct in a microfluidic chip*. *Lab Chip*, **8**, 663-671 (2008).
- [82] A. CURTIS, C. WILKINSON. *Topographical control of cells*. *Biomaterials*. **18**, 1573-1583 (1997).
- [83] C. M. NELSON. *Tissue Geometry Determines Sites of Mammary Branching Morphogenesis in Organotypic Cultures*. *Science*, **314**, 298-300 (2006).

- 
- [84] A. KHADEMOSSEINI, R. LANGER, J. BORENSTEIN, J. P. VACANTI. *Microscale technologies for tissue engineering and biology*. Proc. Natl. Acad. Sci., **103**, 2480-2487 (2006).
- [85] A. A. SOLOVEV, Y. F. MEI, E. BERMUDEZ URENA, G. HUANG, O. G. SCHMIDT. *Catalytic Microtubular Jet Engines Self-Propelled by Accumulated Gas Bubbles*. Small, **5**, 1688-1692 (2009).
- [86] A. A. SOLOVEV, E. J. SMITH, C. C. BOF BUFON, S. SANCHEZ, O. G. SCHMIDT. *Light-Controlled Propulsion of Catalytic Microengines*. Angew. Chem. Int. Ed., **50**, 10875-10878 (2011).
- [87] A. A. SOLOVEV, X. WANG, D. H. GRACIAS, S. M. HARAZIM, C. DENEKE, S. SANCHEZ, O. G. SCHMIDT. *Self-Propelled Nanotools*. ACS Nano, **22**, 1751-1756 (2012).
- [88] G. M. WHITESIDES. *The origins and the future of microfluidics*. Nature, **442**, 368-373 (2006).
- [89] Y. DAGHIGHI, D. LI. *Micro-valve using induced-charge electrokinetic motion of Janus particle*. Lab Chip, **11**, 2929-2940 (2011).
- [90] D. LAI, J. P. FRAMPTON, H. SRIRAM, A. TAKAYAMA. *Rounded multi-level microchannels with orifices made in one exposure enable aqueous two-phase system droplet microfluidics*. Lab Chip, **11**, 3551-3554 (2011).
- [91] P. E. BOUKANY, A. MORSS, W.-C. LIAO, B. HENSLEE, H. C. JUNG, X. ZHANG, B. YU, X. WANG, Y. WU, L. LI, K. GAO, X. HU, X. ZHAO, O. HEMMINGER, W. LU, G. P. LAFYATIS, L. J. LEE. *Nanochannel electroporation delivers precise amounts of biomolecules into living cells*. Nature nanotech., **6**, 747-754 (2011).
- [92] S. M. HARAZIM, V. A. BOLANOS QUINONES, S. KIRAVITTAYA, S. SANCHEZ, O. G. SCHMIDT. *Lab-in-a-Tube: on-chip integration of glass optofluidic ring resonators for label-free sensing applications*. Lab Chip, doi: 10.1039/C2LC40275K (2012).
- [93] I. M. WHITE, H. ZHU, J. D. SUTER, N. M. HANUMEGOWDA, H. OVEYS, M. ZOUROB, X. FAN. *Refractometric Sensors for Lab-on-a-Chip Based on Optical Ring Resonators*. IEEE Sensors Journal, **7**, 28-35 (2007).
- [94] J. HONG, J. B. EDEL, A. J. DEMELLO. *Micro- and nanofluidic systems for high-throughput biological screening*. Drug Discovery Today, **14**, 134-146 (2008).
- [95] K. SCHOLTEN, X. FAN, E. T. ZELLERS. *Microfabricated optofluidic ring resonator structures*. Appl. Phys. Lett., **99**, 141108 (2011).

- 
- [96] Y. GAO, Q. GAN, Z. XIN, X. CHENG, F. J. BARTOLI. *Plasmonic Mach Zehnder Interferometer for Ultrasensitive On-Chip Biosensing*. ACS Nano, **12**, 9836-9844 (2011).
- [97] R.G. HEIDEMAN, P.V. LAMBECK. *Remote opto-chemical sensing with extreme sensitivity: design, fabrication and performance of a pigtailed integrated optical phase-modulated Mach-Zehnder interferometer system*. Sens. Actuators B, **61**, 100-127 (1999).
- [98] F. C. CHIEN, C. Y. LIN, J. N. YIH, K. L. LEE, C. W. CHANG, P. K. WEI, C. C. SUN, S.J., CHEN. *Coupled waveguide-surface plasmon resonance biosensor with subwavelength grating*. Biosens. Bioelectron., **22**, 2737-2742 (2007).
- [99] D. MONZON-HERNANDEZ, J. VILLATORO. *High-resolution refractive index sensing by means of a multiple-peak surface plasmon resonance optical fiber sensor*. Sens. Actuators B, **115** 227-231 (2006).
- [100] R. HORVATH, H.C. PEDERSEN, N. SKIVESEN, D. SELMECZI, N.B. LARSEN. *Optical waveguide sensor for on-line monitoring of bacteria*. Opt. Lett., **28**, 1233-1235 (2003).
- [101] Y. WANG, H. LI, Z. CAO, T. YU, Q. SHEN, Y. HE. *Oscillating wave sensor based on the Goos-Hänchen effect*. Appl. Phys. Lett., **92**, 061117 (2008).
- [102] C. F. CARLBORG, K. B. GYLFASON, A. KAZMIERCZAK, F. DORTU, M. J. BANULS POLO, A. MAQUIEIRA CATALA, G. M. KRESBACH, H. SOHLSTRÖM, T. MOH, L. VIVIEN, J. POPPLEWELL, G. RONAN, C. A. BARRIOS, G. STEMME, W. VAN DER WIJNGAART. *A packaged optical slot-waveguide ring resonator sensor array for multiplex label-free assays in labs-on-chips*. Lab Chip, **10**, 281-290 (2010).
- [103] B. CUNNINGHAM, P. LI, B. LIN, J. PEPPER. *Colorimetric resonant reflection as a direct biochemical assay technique*. Sens. Actuators B., **81**, 316-328 (2002).
- [104] P.Y. LI, B. LIN, J. GERSTENMAIER, B.T. CUNNINGHAM. *A new method for label-free imaging of biomolecular interactions*. Sens. Actuators B, **99**, 6-13 (2004).
- [105] T.L. LOWDER, J.D. GORDON, S.M. SCHULTZ, R.H. SELFRIDGE. *Volatile organic compound sensing using a surfacerelief D-shaped fiber Bragg grating and a polydimethylsiloxane layer*. Opt. Lett., **32**, 2523-2525 (2007).
- [106] F. XU, P. HORAK, G. BRAMBILLA. *Optical microfiber coil resonator refractometric sensor: erratum*. Opt. Express, **15**, 9385-9385 (2007).

- 
- [107] S. LACEY, I. M. WHITE, Y. SUN, S. I. SHOPOVA, J. M. CUPPS, P. ZHANG, X. FAN. *Versatile opto-fluidic ring resonator lasers with ultra-low threshold*. Opt. Express, **15**, 15523-15530 (2007).
- [108] A. M. ARMANI, K. J. VAHALA. *Heavy water detection using ultra-high-Q microcavities*. Opt. Lett., **31**, 1896-1898 (2006).
- [109] A. RAMACHANDRAN, S. WANG, J. CLARKE, S. J. JA, D. GOAD, L. WALD, E. M. FLOOD, E. KNOBBE, J. V. HRYNIEWICZ, S.T. CHU, D. GILL, W. CHEN, O. KING, B. E. LITTLE. *A universal biosensing platform based on optical micro-ring resonators*. Biosens. Bioelectron., **23**, 939-944 (2008).
- [110] Y. SUN, J. LIU, D. J. HOWARD, G. FRYE-MASON, A. K. THOMPSON, S.-J. JA, X. FAN. *Rapid tandem-column micro-gas chromatography based on optofluidic ring resonators with multi-point on-column detection*. Analyst, **135**, 165-171 (2010).
- [111] H. ZHU, I. M. WHITE, J. D. SUTER, M. ZOUROB, X. FAN. *Integrated Refractive Index Optical Ring Resonator Detector for Capillary Electrophoresis*. Anal. Chem., **79**, 930-937 (2007).
- [112] V. ZAMORA, A. DIEZ, M. V. ANDRES, A. GIMENO. *Refractometric sensor based on whisperinggallery*. Opt. Expr., **15**, 12011-12016 (2007).
- [113] O. G. Schmidt, N. Y. Jin-Phillipp. *Free-standing SiGe-based nanopipelines on Si (001) substrates*. Appl. Phys. Lett., **78**, 3310-3312 (2001).
- [114] C. DENEKE, O. G. SCHMIDT. *Real-time formation, accurate positioning, and fluid filling of single rolled-up nanotubes*. Appl. Phys. Lett., **85**, 2914-2916 (2004).
- [115] SCHOTT AG. *Eigenschaften von D 263 T*. <http://www.schott.com> (2012).
- [116] W. MARTIENSSEN, HANS WARLIMONT. *Springer handbook of condensed matter and materials data*. Heidelberg: Springer, 1st ed. p. 438-439 (2005).
- [117] ANIKA KOHLSTEDT. *SU-8 als Konstruktionswerkstoff*. TU Darmstadt, Institut für Elektromechanische Konstruktionen (2011).
- [118] D. ARMANI, C. LIU, N. ALURU. *Re-configurable fluid circuits by PDMS elastomer micromachining*. Micro Electro Mechanical Systems, **MEMS99**, 222-227 (1999).
- [119] THE ENGINEERING TOOL BOX. *Elastic Properties and Young Modulus for some Materials*. <http://www.engineeringtoolbox.com> (2012).

- 
- [120] MICRO CHEMICALS. *NANO<sup>TM</sup> SU-8 Negative Tone Photoresist Formulations 2-25*.  
www.microchem.com, **Rev. 2** (2002).
- [121] T. KIPP, H. WELSCH, CH. STRELOW, CH. HEYN, D. HEITMANN. *Optical Modes in Semiconductor Microtube Ring Resonators*. Phys. Rev. Lett. **96**, 077403 (2006).
- [122] C. STRELOW, H. REHBERG, C. M. SCHULTZ, H. WELCH, C. HEYN, D. HEITMANN, T. KIPP. *Optical microcavities formed by semiconductor microtubes using a bottle-like geometry*. Phys. Rev. Lett., **101**, 127403 (2008).
- [123] J. W. ELAM, D. ROUTKEVITCH, P. P. MARDILOVICH, S. M. GEORGE. *Conformal Coating on Ultrahigh-Aspect-Ratio Nanopores of Anodic Alumina by Atomic Layer Deposition*. Chem. Matter., **15**, 3507-3517 (2003).
- [124] E. J. SMITH, W. XI, D. MAKAROV, I. MÖNCH, S. M. HARAZIM, V. A. BOLAÑOS QUIÑONES, C. K. SCHMIDT, Y. MEI, S. SANCHEZ, O. G. SCHMIDT. *Lab-in-a-Tube: Ultracompact components for on-chip capture and detection of individual bioorganisms*. Lab Chip, doi: 10.1039/c2lc21175k (2012).
- [125] I. M. WHITE, J. GORING, Y. SUN, G. YANG, S. LACEY AND X. FAN. *Versatile waveguide-coupled optofluidic devices based on liquid core optical ring resonators*. Appl. Phys. Lett., **91**, 241104 (2007).
- [126] V. A. BOLAÑOS QUIÑONES, G. HUANG, J. D. PLUMHOF, S. KIRAVITTAYA, A. RASTELLI, Y. F. MEI, O. G. SCHMIDT. *Optical resonance tuning and polarization of thin-walled tubular microcavities*. Opt. Lett. **34**, 2345-2347 (2009).
- [127] M. HOSODA, T. SHIGAKI. *Degeneracy breaking of optical resonance modes in rolled-up spiral microtubes*. Appl. Phys. Lett., **90**, 181107 (2007).
- [128] S. SCHUMACHER, J. NESTLER, TH. OTTO, M. WEGENER, E. EHRENTREICH-FÖRSTER, D. MICHEL, K. WUNDERLICH, S. PALZER, K. SOHN, A. WEBER, M. BURGARD, A. GRZESIAK, A. TEICHERT, A. BRANDENBURG, B. KOGER, J. ALBERS, E. NEBLING, F. F. BIER. *Highly-integrated lab-on-chip system for point-of-care multiparameter analysis*. Lab Chip, **12**, 464-473 (2011).
- [129] I. MÖNCH, J. SCHUMANN, M. STOCKMANN, K.-F. ARNDT, O. G. SCHMIDT. *Multifunctional nanomembranes self-assembled into compact rolled sensor-actuator devices*. Smart Mater. Struct., **20**, 085016 (2011).

- [130] M. SUMETSKY, R. S. WINDELER, Y. DULASHKO, X. FAN. *Optical liquid ring resonator sensor*.  
Opt. Expr., **15**, 14376-14381 (2007).

## List of Figures and Tables

Figure 2.1: General method to create a nanotube. ....	5
Figure 2.2: Schematics of bending behavior. ....	6
Figure 2.3: SEM images of wrinkled nanomembranes. ....	6
Figure 2.4: Rolled-up nanotech on polymers. ....	7
Figure 2.5: Schematic of the structure of the electric double layer. ....	10
Figure 2.6: Example a complex on-chip microfluidic structure. ....	11
Figure 2.7: General schematic of the detection principle of label-free refractive index based sensors. ....	12
Figure 2.8: Schematic drawing of the working principle of an OFRR. ....	13
Figure 3.1: Overview over the BOC Edwards FL400 electron beam evaporation device. ....	18
Figure 3.2: ALD deposition cycle. ....	19
Figure 4.1: The roll-up pattern. ....	30
Figure 4.2: Schematic view on the sample holder in the electron beam evaporation device. ....	32
Figure 4.3: Arrays of rolled-up microtubes. ....	32
Figure 4.4: SEM images of a rolled-up microtube. ....	33
Figure 4.5: Diameter of microtubes at different bilayer compositions. ....	34
Figure 4.6: Investigation on the fluidic capabilities of microtubes. ....	35
Figure 4.7: In-flow studies with integrated microtubes. ....	36
Figure 4.8: Biofunctionalized array of rolled-up microtubes. ....	38
Figure 4.9: Catalytic microtubes in a microfluidic system. ....	39
Figure 4.10: Self-propelled nanotool. ....	40
Figure 4.11: Microtubes with bio-functionalized surfaces. ....	41
Figure 4.12: A catalytic micropump. ....	43
Figure 4.13: Principle of a microvalve. ....	43
Figure 4.14: SiO <sub>x</sub> microtubes as optical sensors. ....	44
Figure 5.1: Fabrication flow chart for the integration of high quality rolled-up optofluidic resonators. ....	49
Figure 5.2: Sketch of the alignment structures. ....	51
Figure 5.3 Sketch of a socket structure. ....	52
Figure 5.4: Optical image of a pair of sockets consisting of the SU-8 photoresist. ....	53
Figure 5.5: SEM images and zooms of a free-standing microtube. ....	54
Figure 5.6: Fabrication of free-standing microtubes. ....	55
Figure 5.7: PL-characteristic map of a Si substrate with free-standing rolled-up microtubes. ....	56
Figure 5.8: Optical characterization of a rolled-up microtube by photoluminescence spectroscopy. ....	57
Figure 5.9: Sketch of a transferred microtube. ....	58
Figure 5.10: Principle of fixation and stabilization of microtubes by ALD. ....	59
Figure 5.11: Photolithography on microtubes. ....	60
Figure 5.12: Sketch of the principle of the microfluidic integration of a microtube. ....	60
Figure 5.13: Overview on the microfluidic structure of the chip. ....	61

---

<i>Figure 5.14: Overview on the final device structure.</i> .....	63
<i>Figure 5.15: Integrated microtube.</i> .....	64
<i>Figure 5.16: Sequence of optical images showing filling and emptying of a microtube.</i> .....	65
<i>Figure 5.17: Moving cells in a microtube.</i> .....	66
<i>Figure 5.18: PC controlled particle movement.</i> .....	66
<i>Figure 5.19: Quality factor evolution of three integrated rolled-up tubular ring-resonators.</i> .....	68
<i>Figure 5.20: Schematic drawing of the microfluidic setup.</i> .....	69
<i>Figure 5.21: Resonant mode response to changes of the refractive index.</i> .....	70
<i>Figure 5.22: Drying of a microtube</i> .....	71
<i>Figure 5.23: Determination of the signal stability.</i> .....	72
<i>Figure 5.24: In-flow studies on a RU-OFRR.</i> .....	73
<i>Figure 5.25: Example of a sensing sequence detected by PL spectroscopy.</i> .....	74
<i>Figure 5.26: Sensing the change of refractive index of analytes.</i> .....	75
<i>Figure 5.27: Mode shift of the peak position of mode 51.</i> .....	75
<i>Figure 5.28: Different views on a dried out microtube containing glucose.</i> .....	76
<i>Table 3.1: Utilized analytes sorted by their refractive indices</i> .....	22
<i>Table 5.1: Performance of different OFRRs</i> .....	77

## ***Versicherung***

Hiermit versichere ich, dass ich die vorliegende Arbeit ohne unzulässige Hilfe Dritter und ohne Benutzung anderer als der angegebenen Hilfsmittel angefertigt habe; die aus fremden Quellen direkt oder indirekt übernommenen Gedanken sind als solche kenntlich gemacht.

Bei der Auswahl und Auswertung des Materials sowie bei der Herstellung des Manuskripts habe ich Unterstützungsleistungen von folgenden Personen erhalten:

Prof. Dr. Oliver G. Schmidt

Dr. Samuel Sanchez

Dr. Dominic Thurmer

Vladimir Bolanos

Britta Koch

Marlitt Viehrig

Weitere Personen waren an der Abfassung der vorliegenden Arbeit nicht beteiligt. Die Hilfe eines Promotionsberaters habe ich nicht in Anspruch genommen. Weitere Personen haben von mir keine geldwerten Leistungen für Arbeiten erhalten, die im Zusammenhang mit dem Inhalt der vorgelegten Dissertation stehen.

Die Arbeit wurde bisher weder im Inland noch im Ausland in gleicher oder ähnlicher Form einer anderen Prüfungsbehörde vorgelegt.

.....

Ort, Datum

.....

Unterschrift



## *Theses*

1. Rolled-up nanotech on polymers facilitates the simple and deterministic fabrication of a large number of well-aligned microtubes on a single chip.
2. Rolled-up microtubes have the potential to work as sensors and actuators in Lab-on-a-Chip devices such as optically active microtubes working as optical ring resonators.
3. The design of a microtube can enhance its sensing properties.
4. If optically active microtubes are utilized as optical ring resonators, it is expected that a higher optical Q value goes along with a higher sensitivity.
5. If optically active microtubes are utilized as optical ring resonators a low refractive index medium around the microtube enhances the sensitivity.
6. If microtubes are utilized as optical sensors it is recommended to avoid continuous material accumulation on the wall to maintain the sensing capabilities.
7. If microtubes are utilized as optical sensors it is expected that a suitable low detection limit can enable them to detect single molecules on the tubular wall.
8. Microtubes fabricated by rolled-up nanotech can be integrated into a complex on-chip microfluidic structure.
9. If transferring optically active microtubes from a mother substrate to a target substrate, the on-chip integration requires a socket system.
10. The on-demand and reproducible exchange of the content of a rolled-up microtube requires on-chip integration into a microfluidic channel system.
11. Rolled-up nanotech on polymers in combination with bio-functionalization can be utilized to fabricate low-cost and biocompatible catalytic microtubes.
12. Microtubes, transparent in the visible spectrum, can be utilized as artificial on-chip scaffolds and reaction containers for cells.



## *Acknowledgements*

Here I would like to take the time to acknowledge all the people who have helped and supported me during the long way to complete this thesis.

First of all I would like to thank Professor Dr. Oliver G. Schmidt for giving me the chance to work in in his exciting Institute and supervising my Ph.D. thesis.

I greatly appreciate Professor Dr. Thomas Geßner to be a referee for my doctoral thesis and for taking time in his busy calendar.

Next, I would like to thank Dr. Samuel Sanchez for his ongoing support in scientific questions and excellent advice for teaching me the meaning of nicely written publications. I also would like to thank Yongfeng Mei for introducing me to the scientific research in this institute and mentoring during the first half of my Ph.D. thesis.

Thanks also to the rest of the NBC group I belong to. Thanks to Britta Koch, Marlitt Viehrig, Dr. Vanessa Plans, Veronika Magdanz, Adithya (Adi) Nagarakodige Ananth, Darijan Kantor and Dr. Wang Xi (Simon) for making my PhD time very pleasant, helping a lot during experiments and doing fruitful discussions with me.

Thanks to all the many other people at the IIN for their help, technical support and nice discussions during my PhD time including Ronny Engelhard without whom many machines at the IIN would not be working. Thanks also to Vladimir Bolanos, I enjoyed very much the time in the PL lab and appreciate the big help from him on the fabrication and characterization of the sensors. Thanks to Dr. Dominic Thurmer for helping me with the grammar things. Thanks to Dr. Daniel Grimm for his hard work on keeping the clean room running. Thanks to Emica Coric for introducing me into SEM imaging which saved a lot of time. Thanks to Dr. Stefan Baunack for doing some important FIB cuts for me. Thanks to Barbara Eichler for AFM measurements and for cutting all my wafers as well as Dr. Ingolf Mönch for nice and helpful discussions. Cornelia Krien for taking care on the consumables in the labs and Dr. Christoph Deneke for introducing me into working in chemistry labs and showing me how exhausting it can be to etch with HF in summer. I would also like to thank the IT people René Pokorny and André Eichler for always fast support if there was any trouble with computers.

Thanks go out to all the friends I've had the pleasure of spending time with and discussing ideas: Elliot Smith, Alex Solovev, Sabine Schulze, Michael Melzer, Wenping Si, Junwen Deng, Anika Hofmann, Stefan Böttner, Martin Bauer, Daniil Karnaushenko, Kumar Santosh, Bianca Höfer, Peixuan Chen, Irma Sujanski, Dr. Hengxing Ji, Dr. Xinghua Kong, Dr. Peter Cendula, Dr. Thomas Dienel, Dr. Denys Makarov, Dr. Larysa Baraban, Dr. Lichun Jang, Dr. Cesar Bof Bufon, Dr. Ping Feng, all of which were there at some point during my PhD and for being there when it was necessary to simply go out and have fun.

Thanks to all of my friends out there and to anyone else who has helped me on my way that I may have forgotten, but hopefully did not.



## Publications (Peer-Review)

1. S. M. Harazim, V. A. Bolaños Quiñones, S. Kiravittaya, S. Sanchez, O. G. Schmidt.  
*Lab-in-a-Tube: on-chip integration of glass optofluidic ring resonators for label-free sensing applications.*  
Lab Chip, **2012**, doi: 10.1039/C2LC40275K.
2. E. J. Smith, W. Xi, D. Makarov, I. Mönch, S. M. Harazim, V. A. Bolaños-Quiñones, C. K. Schmidt, Y. Mei, S. Sanchez, O. G. Schmidt.  
*Lab-in-a-Tube: Ultracompact components for on-chip capture and detection of individual bioorganisms.*  
Lab Chip, **2012**, doi: 10.1039/c2lc21175k.
3. A. A. Solovev, X. Wang, D. H. Gracias, S. M. Harazim, C. Deneke, S. Sanchez, O. G. Schmidt.  
*Self-Propelled nanotools.*  
ACS Nano, **2012**, 6, 1751-1756.
4. S. M. Harazim, W. Xi, C. K. Schmidt, S. Sanchez, O. G. Schmidt.  
*Fabrication and applications of large arrays of multifunctional rolled-up SiO/SiO<sub>2</sub> microtubes.*  
Journal of Materials Chemistry, **2012**, 22, 2878-2884.
5. S. Sanchez, A. A. Solovev, S. M. Harazim, C. Deneke, Y. F. Mei, O. G. Schmidt.  
*The smallest Man-Made Jet Engine.*  
The Chemical Record, **2011**, 11, 367-370.
6. S. M. Harazim, P. Feng, S. Sanchez, C. Deneke, Y. F. Mei, O. G. Schmidt.  
*Integrated sensitive on-chip ion field effect transistors based on wrinkled InGaAs nanomembranes.*  
Nanoscale Research Letters, **2011**, 6:215.
7. S. Sanchez, A. A. Solovev, S. M. Harazim, O. G. Schmidt.  
*Microbots swimming in the flowing streams of microfluidic channels.*  
Journal of American Chemical Society, **2011**, 133, 701-703.
8. Y. F. Mei, S. Kiravittaya, S. M. Harazim, O. G. Schmidt.  
*Principles and applications of micro and nanoscale wrinkles.*  
Materials Science and Engineering R, **2010**, 70, 209-224.
9. P. Feng, I. Mönch, G. S. Huang, S. M. Harazim, E. J. Smith, Y. F. Mei, O. G. Schmidt.  
*Local-illuminated ultrathin silicon nanomembranes with photovoltaic effect and negative transconductance.*  
Advanced Materials, **2010**, 22, 3667.
10. P. Feng, I. Mönch, S. M. Harazim, G. S. Huang, Y. F. Mei, O. G. Schmidt.  
*Giant persistent photoconductivity in rough silicon nanomembranes.*  
Nano Letters, **2009**, 9, 3453-3459.

## Conferences and scientific presentations

1. S. M. Harazim, S. Sanchez, O. G. Schmidt.  
*Integration of free-standing rolled-up microtubes into a microfluidic system for sensor applications.*  
NanoBioTec Montreux **2010**, 15.-17. November - poster
2. S. M. Harazim, Y. F. Mei, P. Feng, C. Deneke, O. G. Schmidt.  
*Ion sensitive field effect transistor based on wrinkled nanochannels integrated on a chip.*  
MRS Spring Meeting San Francisco **2010**, 6. April - oral
3. S. M. Harazim, Y. F. Mei, O. G. Schmidt.  
*Electrically forced ion transport through nanofluidic channels based on wrinkled InGaAs-layers.*  
IFW Dresden winter school: Nanomembranes, Oberwiesenthal **2009**, January 12-14 - oral
4. S. M. Harazim, P. Schwille.  
*Controlled dynamic droplet fusion in PDMS based microelectromechanical systems (MEMS) for GFP in-vitro expression.*  
Saxon Biotechnology Symposium Dresden **2007**, 28. November - poster

## Cover pages in journals

1. Lab Chip, **2012**, received invitation, draft submitted for consideration (17.05.2012)
2. J. Mater. Chem., **2012**, 22, 2878

## Patents

1. "Verfahren zur Herstellung von Mikrofluidsystemen" – patent pending
2. "Verfahren für die Positionierung von Mikrostrukturelementen" – patent pending

## Grants and contributions to research groups

1. DAAD, travel grant 2010, City University Hong Kong.
2. Contribution to the DFG research group 1713 "Sensoric Micro- and Nanosystems"
3. Participation on projects I/84 072 und 86362 of the Volkswagen foundation

